
THE UNIVERSITY *of* EDINBURGH

# Nonlinear Waves In Nematic Liquid Crystals

*Enrique Calisto Leiva*

Doctor of Philosophy
University of Edinburgh
August 2024

# Declaration

I declare that this thesis was composed by myself and that the work contained therein is my own, except where explicitly stated otherwise in the text.

(*Enrique Calisto Leiva*)

# Lay Summary

Optics is the branch of physics that studies the behaviour and properties of light and its interaction with matter. Commonly, visible light refers to electromagnetic radiation that the human eye can perceive, but in Physics, the term *light* refers to electromagnetic radiation of any wavelength, whether visible or not. The experimental development of laser beams (light sources that produce a very narrow beam of a single wavelength or colour) in 1960, instigated the interest in new materials and their interaction with powerful optical beams. One of these fascinating materials is liquid crystals, chemical compounds whose properties are between fluid and solid crystallines, they are characterized for interacting strongly with electromagnetic fields (in particular, laser beams).

Liquid crystals offer a wide range of technological and scientific applications, currently being used in devices such as smart screens, mobile phones and televisions. Moreover, their versatility can play a role in future optical communications, signal processing and computational progress. This thesis studies the interaction between laser beams and a particular type of liquid crystal material, examining the path followed by the light as it travels along the material and the potential design of an optical isolator, a device that distinguishes light signals travelling in one direction from those travelling in the opposite one.

# Abstract

In the last few decades, nonlinear, nonlocal optical media have emerged as an ideal setting for experimentally observing and studying nonlinear optical phenomena such as modulation instability, random lasing, spatial solitons and shock waves. In particular, liquid crystals in the nematic mesophase (NLC) support self-confined optical spatial solitons, named in this context as *nematicons*, i.e. stable and robust self-confined beams which can propagate without diffraction within the self-induced channel waveguide. They have become the focus of several studies following their demonstration in planar nematic liquid crystal cells and hold special interest due to their potential use in the design of all-optical devices such as diodes, isolators and optical switches. From a theoretical perspective, nematicon propagation is described by a system of nonlinear dispersive-wave equations constituted by a nonlinear Schrödinger-like equation for the optical beam and an elliptic Poisson equation for the response of the liquid crystal. This system of equations has no exact solutions, therefore most effort is devoted to improving numerical methods, although modulation theories can also give insight into the mechanisms behind the optical beam evolution.

In this thesis, we investigate self-induced waveguides which, by launching nematicons from the opposite ends of a sample cell, establish signal pipelines with distinguishable paths, resulting in a diode-like transmission. We specifically examine the generation and path of extraordinary-wave nematicons in planar cells of nematic liquid crystals (NLC) when launching identical beams from the opposite ends of samples with linearly modulated angle distributions of the optic axis, i.e. a varying molecular background orientation across the transverse and propagation coordinates.

# Acknowledgements

First and foremost I want to thank my former supervisor, Prof. Noel Smyth, he and his family Julie and Callum welcomed me into his home as one more member of his family when I arrived in Edinburgh in the middle of the COVID-19 pandemic. He showed me kindness, patience, generosity and support until the end, and I will always be grateful for his encouragement and all the knowledge he shared with me.
I would also like to thank Prof. Gaetano Assanto for his guidance, knowledge, fruitful collaboration, and patience with me and my constant delays. Thanks too, to my supervisor Prof. Tom Mackay for his kindness, positive disposition and willingness to support me. Special thanks to Prof. Moritz Linkmann and Prof.Marcel Clerc.
Next, I would like to thank all the people I have met in Edinburgh. To Rodrigo, who I've known for more than 10 years but who became my close friend in Edinburgh, thank you for all the time and conversations shared. To Patricio, for the friendship, food and conversations shared. To Andres and Koraima, for always making me feel welcome to their flat and for going through the PhD journey together. To my flatmates, Druk, Kyohei, Utkarshinee, Will and especially to Dayun and Jungmin for their friendship and encouragement. To Angela, thank you for your love, support and patience, and for pushing me to finish the thesis in time. To all the people I have met in the EUTTC: Fred, Isaac, Faye, Daniel, Charmaine, Richard, Soma, Jerry, Petrina and many more. Special thanks to Joel and Georges, for their friendship and support for my thesis progress.
Finally, I would like to thank all the friends from Chile who have kept in contact and have motivated me: Nico, Ricardo, Camilo, Sebastian (Mario), Beatriz, Paul, Valeska, Mireya and many others. Special thanks to Pedro, Rayen and Francisco (Fransafu) for all the memes, and discord conversations and for caring about me. To Karina and Maria Jose for their friendship, encouragement and caring about me and my thesis progress. To my mother, aunt and brother David for their constant support and encouragement at a distance. Thanks for making this PhD thesis possible.

# Contents

# List of Abbreviations

| | |
|---|---|
| **LCs** | Liquid Crystals |
| **NLC** | Nematic Liquid Crystal |
| **IST** | Inverse Scattering Transform |
| **KdV** | Korteweg-de Vries Equation |
| **NLS** | Nonlinear Schrödinger Equation |
| **NNLSE** | Nonlocal Nonlinear Schrödiger Equation |
| **FP** | Forward propagating beam or signal |
| **BP** | Back-launched beam or signal |
| **SOS** | Spatial Optical Soliton |
| **ODE** | Ordinary Differential Equation |
| **PDE** | Partial Differential Equation |
| **ITO** | Indium-tin oxide |
| **PVA** | Polyvinyl Alcohol |
| **NIR** | Near-infrared |
| **UV** | Ultraviolet |
| **SVEA** | Slowly Varying Envelope Paraxial Approximation |
| **FFT** | Fast Fourier Transform |
| **RK4** | Fourth-order Runge-Kutta |
| **CP** | Counterpropagating beams |

# List of Frequent Symbols

| | |
|---|---|
| $\nabla_\perp^2$ | Transverse part of the Laplacian $\nabla_\perp^2 = \frac{\partial^2}{\partial x^2} + \frac{\partial^2}{\partial y^2}$ |
| $n_o$ | Ordinary refractive index |
| $n_e$ | Extraordinary refractive index |
| $\vec{n}$ | Nematic director |
| $\bar{\bar{\epsilon}}$ | Dielectric tensor |
| $\Delta\epsilon$ | Optical anisotropy |
| $\alpha$ | Scattering loss constant |
| $K$ | Nematic elastic constant |
| $\delta$ | Birefringent walk-off angle |
| $\Delta$ | $\tan\delta = \Delta$ |
| $\theta_b$ | Nematic director background modulation |
| $\psi$ | All-optical reorientation |
| $u$ | Beam electric field envelope |
| $\nu$ | Nonlocality parameter |
| $P_b$ | Dimensional Beam Power |
| $W_b$ | Dimensional Beam Width |
| $(h, d, L)$ | Planar cell dimensions (thickness, width, length) |

# Chapter 1

# Introduction

## 1.1 Solitary waves and solitons

One of the main objects of study in this work corresponds to solitary waves arising in nonlinear, nonlocal optical media. There is no universally accepted definition of a solitary wave. They were first described and observed by John Scott Russell at Edinburgh's Union Canal in 1834 [1] as a wave that propagates over a long distance without losing its shape.

In 1895, Korteweg and de Vries derived an equation describing Russell's experimental observation [2]

$$\frac{\partial u}{\partial t} + 6u\frac{\partial u}{\partial x} + \frac{\partial^3 u}{\partial x^3} = 0. \tag{1.1}$$

Using results from the study of elliptic functions, Korteweg and de Vries found a set of solutions that could travel without dissipating [3]

$$u(x,t) = \frac{1}{2}c\,\mathrm{sech}^2\left(\frac{1}{2}\sqrt{c}(x - ct - x_0)\right). \tag{1.2}$$

The term *soliton* for the same solitary wave described by Russell was introduced by Kruskal and Zabusky [4], for the solitary wave solutions of the Korteweg and de Vries (KdV) equation after showing they have a particle-like interaction, meaning that they could retain their shape after interacting with other solitary waves, leaving only with a phase shift as a consequence of their interaction. The initial value problem for the KdV equation was solved shortly after by Gardner, Greene, Kruskal and Miura [5] using the inverse scattering transform (IST). This established the first general method for solving integrable nonlinear partial differential equations (PDEs), including the nonlinear Schrödinger equation, sine-Gordon equation and the Kadomtsev–Petviashvili equation [6]. However, most of the nonlinear PDEs in applications are not integrable and there are many examples of solitons in nonintegrable systems, that are not necessarily steady, such as breathers or gap solitons, or that display radiating interactions [7, 8].

In optics and related literature, a soliton is a solution of a nonlinear partial

differential equation (PDE) which:

1. Is localized, retaining its basic form over a long time or large distance.
2. Emerge from collisions (elastic or inelastic) with other solitons with a similar size and shape.

Due to soliton's inherent stability, they are ideal information transporters in long-distance transmission. Following the first working fibre-optic data transmission system demonstration in 1965, numerous experiments and theoretical interest have been focused on their practical and potential applications [9, 10]. Hasegawa and Tappert's prediction that optical fibres could support the propagation of stable temporal solitons in 1973 [11], attracted both researchers and members of the communication industry, resulting in the discovery of temporal and spatial solitons in a variety of different materials.

Temporal solitons are formed in fibre waveguides and other dispersive media via a balance between nonlinear self-phase modulation and the linear group velocity dispersion effect [12]. When an optical pulse propagates inside an optical fibre, linear dispersion leads to the frequency components of the beam moving at different speeds, resulting in a temporal broadening of the beam. However, due to the nonlinear self-phase modulation, the carrier frequency changes, with the degree and sign of the change dependent on the pulse form. For a bright pulse, the leading edge moves more slowly than the trailing edge, resulting in an overall pulse compression. Depending on the pulse amplitude and waveform, the compression effect can balance the dispersion, and the pulse propagates without deformation, forming a bright temporal optical soliton. On the other hand, spatial optical solitons result from the balance between nonlinear self-focusing and linear diffractive spreading in nonlinear media. Natural diffraction can be countered by an increase in the refractive index of the medium in the vicinity of an optical beam, which focuses the beam. Due to the diversity of materials and the fact that spatial diffraction is not restricted to one dimension, there are many types of spatial optical solitons. Depending on the physical mechanism, they can be classified into Kerr-solitons [13], photorefractive solitons [14], quadratic solitons [15], nematicons [16], etc.

## 1.2 Nematicons

One of the most interesting materials supporting spatial solitons corresponds to nematic liquid crystals (NLC), capable of local and nonlocal interactions which allow a light beam to experience self-focusing; solitons observed in NLC are then termed *nematicons* [16]. The equations modelling light-beam propagation in an NLC are strongly related to the nonlinear Schrödinger equation (NLSE), which is the fundamental equation governing soliton evolution in a self-focusing nonlinear optical medium [20] and can be written as

$$i\frac{\partial u}{\partial z} + \frac{1}{2}\nabla^2 u + |u|^2 u = 0, \tag{1.3}$$

where $u$ represents the envelope of the electric field of the beam, $z$ is the propagation variable and the Laplacian operator $\nabla^2$ is taken with respect to the transverse spatial variables, denoted by $\nabla_\perp^2 = \partial_{xx} + \partial_{yy}$ in the (2+1)-D (2-transverse + 1-propagation) evolution problem.

Before deriving Eq. (1.3), we must introduce the concept of *Kerr effect*. The Kerr effect is a change in the refractive index of a material in response to an applied electric field. When the electric field is due to the presence of the light itself, without needing an external electric field, it is called *optical Kerr effect* (or AC Kerr effect) [17]. The effect causes a variation in the index of refraction proportional to the local light intensity, which is significant for very intense light beams, such as those produced by laser [17, 18]. This refractive index variation leads to the nonlinear optical effects of self-focusing, self-modulation and modulation instability [18]. The refractive index can then be phenomenologically represented as

$$n(x, y, z, t) = n_0(x, y, z) + \Delta n(x, y, z, t), \tag{1.4}$$

where $n_0$ is the linear refractive index of the medium and $\Delta n$ is the variation of the nonlinear refractive index caused by the optical field (sometimes called $n_{NL}$ in the literature [20]). In general, the nonlinear refractive index $\Delta n$ is a function of spatial and temporal coordinates and can exhibit spatial and temporal nonlocality. If we do not consider the spatial and temporal nonlocality, it can be shown that

$$\Delta n = n_2 I. \tag{1.5}$$

Where $n_2$ is the nonlinear refractive index coefficient or Kerr coefficient and the relationship between the intensity and the electric field is given by

$$I = \frac{|E|^2}{2\eta}, \tag{1.6}$$

where $\eta = \eta_0/n_0$ with $\eta_0$ the impedance of free space.

We now consider a transversely linearly polarized electric field $\vec{E}(x, y, z)$ propagating in the $z$ direction with phase constant $k_0 n_0$ and $\vec{k} = k_0 \hat{z}$. The field can be expressed in complex representations as

$$\vec{E}(x, y, z) = E_0(x, y, z)\hat{\mathbf{z}} = u(x, y, z)e^{i(k_0 n_0 z - wt)}\hat{\mathbf{z}}, \tag{1.7}$$

where $u(x, y, z)$ is the envelope function of the electric field, $k_0 = \omega n_0/c$ is the wave number and $c$ is the speed of light in vacuum. The propagation of the optical electric field $\vec{E}$ is governed by the electromagnetic wave equation

$$\frac{\partial^2 \vec{E}}{\partial t^2} = c^2 \nabla^2 \vec{E}. \tag{1.8}$$

Substituting (1.7) into (1.8), one gets the Helmholtz equation [19]

$$\nabla_\perp^2 E_0 + k_0^2 n^2 E_0 = 0, \tag{1.9}$$

where $n$ is the refractive index of the medium given by Eq. (1.4).

Assuming that the envelope $u(x, y, z)$ varies slowly along $z$ (*Paraxial approximation*), i.e.

$$\left|\frac{\partial^2 u}{\partial z^2}\right| \ll \left|k_0 \frac{\partial u}{\partial z}\right|, \tag{1.10}$$

and substituting (1.7) into (1.9), we get

$$\nabla_\perp^2 u + 2ik_0 n_0 \frac{\partial u}{\partial z} + k_0^2\{[n(I)]^2 - n_0^2\}u = 0. \tag{1.11}$$

Now, considering that nonlinear effects are much smaller than linear ones, and expressing the intensity in terms of the electric field

$$[n(I)]^2 - n_0^2 \approx n_0^2 n_2 \frac{|u|^2(x, y, z)}{\eta_0}. \tag{1.12}$$

Then (1.11) becomes

$$2ik_0 n_0 \frac{\partial u}{\partial z} + \nabla_\perp^2 u + \frac{k_0 n_0^2 n_2}{\eta_0}|u|^2 u = 0. \tag{1.13}$$

This can be turned directly into the (NLSE) Eq. (1.3) after scaling the coefficients in dimensionless form.

The (1+1)-D (1-transverse + 1-propagation) NLS equation is integrable and possesses exact solutions. It has a stable soliton solution which can be found via the (IST) mentioned earlier, and is given exactly by

$$u(x, z) = a\,\mathrm{sech}(ax)e^{ia^2 z/2}, \tag{1.14}$$

where $a$ is the amplitude of the soliton. It can be directly verified that $u(x, z)$ is not periodic, but localized and monotonically decaying in the transverse variable $x$. This solution can be interpreted as the result of a balance between dispersive effects (proportional to the term $\nabla_\perp^2 u$) and self-focussing effects arising from the nonlinear Kerr response of the medium which depends on the intensity $|u|^2$.

Stable soliton solutions cannot be found for the (2+1)-D NLS equation because solutions blow-up in finite $z$ above an amplitude threshold, in what is usually called *catastrophic collapse* [14]. Stable evolution in (2+1) dimensions can be achieved in materials whose response deviates from the pure Kerr effect, corresponding demonstrations were shown in several systems, using stabilizing mechanisms, such as self-steepening [14], saturation [21], multiphoton absorption [22] and higher-order phenomena [23]. In the case of NLCs, their response is both saturable and nonlocal, as the optical and elastic response of the fluid is wider than the width of the optical beam, which contributes to stabilising optical solitons.

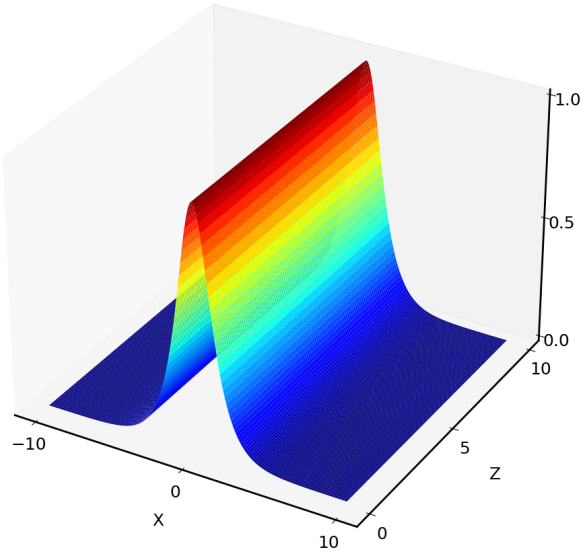


Figure 1.1: Fundamental soliton solution of the (1+1)-D NLS equation.

The robustness of nonlocal solitons has been attributed to the nonlocality regularization effect, which averages perturbations that would grow quickly in a local medium, ensuring greater stability of solitons [24, 25]. The complex interactions between the beam and the medium can be modelled by coupling an NLS-like equation to equations accounting for the medium response.

When the spatial nonlocality of the medium is considered in the optical Kerr effect, the nonlinear refractive index $\Delta n$ is described by the equation

$$w_m^2 \nabla_\perp^2 \Delta n(x,y,z) - \Delta n(x,y,z) = -n_2 |E(x,y,z)|^2, \tag{1.15}$$

where $w_m$ is the nonlinear characteristic length of the material, which represents the characteristic parameter for the scale of space occupied by the nonlinear response function. The equivalent integral expression of Equation (1.15) is

$$\Delta n(x,y,z) = n_2 \int_\Omega K(x,s)|E(s,z)|ds, \tag{1.16}$$

where $K$ is a kernel accounting for the spatial nonlinear response of the medium, and $\Omega$ represents the whole range of the finite space.

Substituting $\Delta n$ into (1.12) and proceeding as before we obtain a more general basic equation encompassing nonlocal soliton (in particular, nematicon) evolution, this is the nonlocal nonlinear Schrödinger equation (NNLSE) [26, 27, 28]

$$i\frac{\partial u}{\partial z} + \frac{1}{2}\nabla_\perp^2 u + 2(K * |u|^2)u = 0. \tag{1.17}$$

Here $*$ denotes a convolution in the spatial variable, i.e,

$$K * |u|^2 = \int_\Omega K(x,s)|u(s,z)|^2 ds. \tag{1.18}$$

The nonlocal nonlinearity in the nematicon equations prevents catastrophic collapse. Solitary waves can then exist and be observed experimentally. Moreover, equation (1.17) is a significantly more general equation, reducing to the NLS equation for a Dirac kernel $K = \delta(x-s)$ and including a wide variety of physical phenomena. It is worth mentioning that equation (1.17) is no longer integrable, and is not possible to formulate an IST formalism, but it possesses a number of conserved quantities [29], such as beam power,

$$P = \int_{\mathbb{R}^2} |u|^2 d^2\mathbf{r}, \tag{1.19}$$

and momentum

$$\mathbf{M} = i\int_{\mathbb{R}^2} (u^*\nabla_\perp u - u\nabla_\perp u^*) d^2\mathbf{r}. \tag{1.20}$$

It should be noted that the power defined by Eq. (1.19) is not the real power carried by the optical beam, but proportional to it. The real power carried by the electromagnetic field is given by

$$P_b = \frac{\epsilon_0 n_0 c}{2}\int_{\mathbb{R}^2} |u|^2 d^2\mathbf{r}. \tag{1.21}$$

where $\epsilon_0$ is the permittivity in vacuum.

## 1.3 Outline of the Thesis

The inspiration for our work goes back to the study of curved nematicons in liquid crystal cells [30], whereby considering a standard geometry, i.e. a planar NLC cell of length $L$, a nonsymmetric modulation can be translated into a curved beam path. In this context, considering the effects of identical excitations launched from opposite ends of the cell can give valuable insights into nonreciprocity and time-symmetry breaking on passive optical systems, since the potential existence of nonoverlapping trajectories between the forward-propagating (FP) beam and the back-launched (BP) beam would correspond to a two-port diode-like device.

Therefore, in this thesis, we investigate the existence of two-port all-optical diodes based on nematicons waveguides in NLCs and study their applicability as optical isolators. Optical isolators, particularly those in guided-wave formats, are elements able to prevent a back-launched (BP) light signal from reaching the input port of the forward-propagating (FP) excitation [31]. There has been a large interest in optical diodes, with the most common approaches based on magneto-optics [32, 33, 34, 35], photonic crystals [34, 36] and passive Kerr-like response [37, 38], among others [39, 40, 41, 42, 43, 44]. Reciprocity breaking in such devices is achieved by either a bias or an all-optical nonlinearity in the

presence of asymmetry [40, 41].

The thesis is organized as follows. Chapter 2 presents a summary of concepts and terminology from optics physics necessary to define the nematicon evolution problem. Chapter 3 introduces the system of nematicon equations and gives a summary of the main theoretical results available. Chapters 4 and 5 explore the main results and the numerical methods employed are described. Finally, a general analysis of the results and possible future research will be presented in Chapter 6.

# Chapter 2

# Physical Background

## 2.1 Liquid Crystals

Liquid crystals are materials which have local positional and orientation correlation, but not long-distance correlation [45, 46], thus allowing them to flow, but also to present crystal-like properties. Positional order refers to regular distances between the molecules, whilst orientational order indicates a common averaged direction. They have been a great source of interest since their discovery, due to their optical properties and wide range of technological applications, one of the most widely known being the liquid crystal display (LCD) illustrated in Figure 2.1.

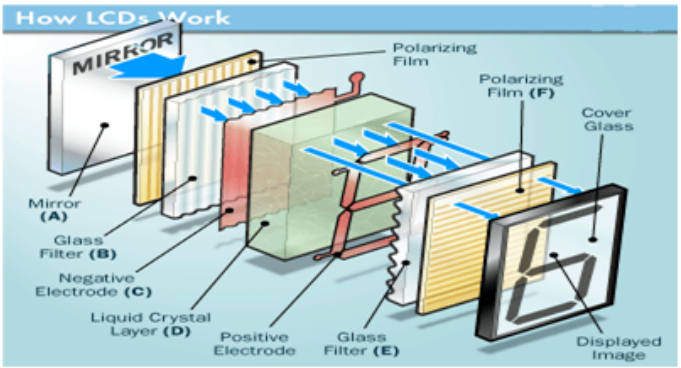


Figure 2.1: Liquid Crystal Display. The device operates by applying a varying electric voltage to a layer of liquid crystal inducing changes in its optical properties [47].

Liquid crystals can appear in different phases depending on temperature (thermotropic state), straining conditions, and the particular properties of the chemical compound [49]. There are three principal phases: nematic, cholesteric and smectic. The nematic phase has the least amount of order and the highest symmetry, presenting only orientational order along a long molecular axis. The cholesteric phase is similar to the nematic, but with chirality, meaning that it has a macroscopic helical structure. Finally, the smectic phase besides having orientational order also has positional order, with the molecules ordered in layers (cf. Fig. 2.2).

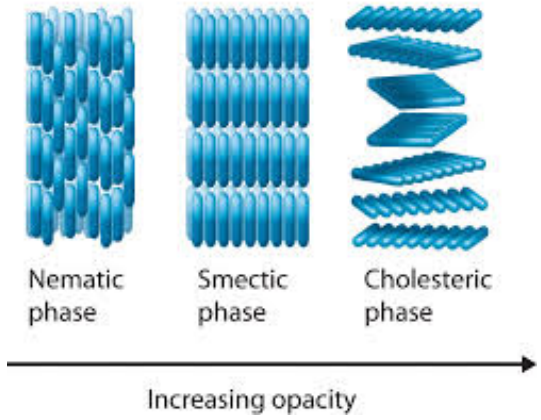


Figure 2.2: Main liquid crystal phases [48].

Nematic molecules are elongated with a rod-like shape. The preferred direction, which may vary throughout the medium, is called the director. The orientation of the director is represented by a unit vector $\vec{n}(\vec{r},t)$, which describes the average molecular orientation in the liquid crystal. In a nematic, the molecules are able to rotate around their long axes, and there is no preferential arrangement of their ends, even if they differ. Hence, the sign of the director has no physical significance, and the nematic behaves optically as a uniaxial material with a centre of symmetry.

To quantify the degree of molecular order at a specific position and the change of the average molecular orientation in space, an *order parameter* is introduced, given by the second rank tensor [49] (also known as the Q-tensor)

$$Q_{\alpha\beta}(\mathbf{r}) = \frac{1}{N}\sum_i \left( u_\alpha^{(i)} u_\beta^{(i)} - \frac{1}{3}\delta_{\alpha\beta} \right), \tag{2.1}$$

where the sum is performed over $N$ molecules in a small but macroscopic volume located at the point $\mathbf{r}$ and $\mathbf{u}^{(i)}$ is a unit vector that describes the orientation of the $i$-th molecule, as shown in Fig. 2.3.

The tensorial order parameter has the following properties:

1. $Q_{\alpha\beta}$ is symmetric.
2. It is traceless, i.e. $TrQ_{\alpha\beta} = Q_{xx} + Q_{yy} + Q_{zz} = 0$.
3. In the isotropic phase $Q_{\alpha\beta} = 0$.

In certain cases, it is possible to simplify the Q-tensor and introduce more physically intuitive quantities. In particular, for a *uniaxial* nematic, the Q-tensor simplifies to

$$Q_{\alpha\beta} = S(n_\alpha n_\beta - \delta_{\alpha\beta}), \tag{2.2}$$

where $n_\alpha$ are the components of the director $\mathbf{n}$ in the laboratory coordinate system and $S$ is an scalar order parameter. If $\theta_m$ is the angle between the nematic

molecules and the director $\mathbf{n}$, then [46]

$$S = \frac{1}{2}\langle 3\cos^2\theta_m - 1\rangle, \tag{2.3}$$

where the average $\langle\cdot\rangle$ is taken over the total solid angle. The range for $S$ is given by $-1/2 \leq S \leq 1$, with $S = 1$ corresponding to the perfect alignment of all the molecules along the director and $S = 0$ to the isotropic phase.

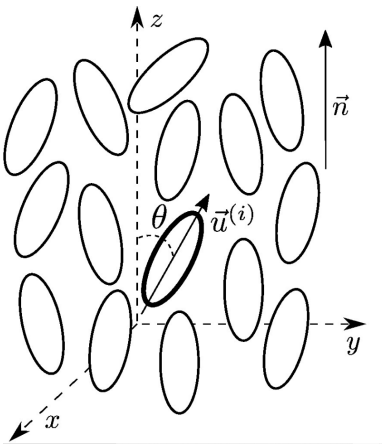


Figure 2.3: Orientation of the molecules in the nematic mesophase. The unit vector $\mathbf{u}^{(i)}$ along the axis of the $i$-th molecule describes its orientation The director $\mathbf{n}$ corresponds to the average molecular alignment. Reproduced from [49].

Experimentally uniform equilibrium configurations of the director are rarely observed and different textures can be observed under cross-polarizers, Fig. 2.4 presents an example of a schlieren texture in an NLC.

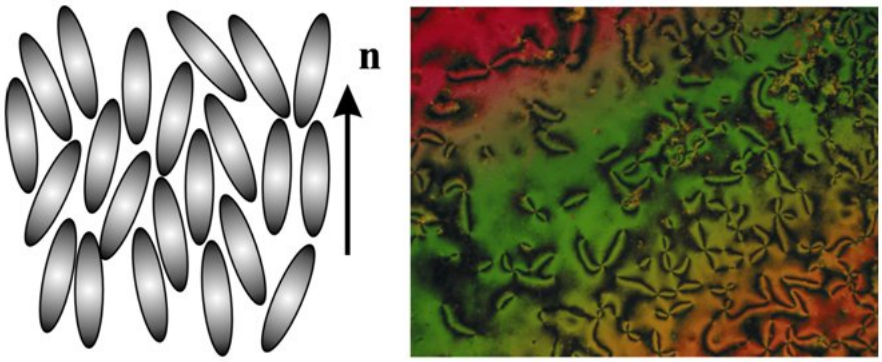


Figure 2.4: Right: Near uniform equilibrium distribution. Left: Schlieren texture in a nematic liquid crystal film under cross-polarizers. Two types of topological defects can be observed with different cores and opposite signs of their topological charges[51].

Liquid crystals are a highly dissipative medium whose dynamics is characterized by minimizing their elastic energy. In nematic materials there are three principal distinct and macroscopic director axis deformations: twist, splay and

bend (c.f. Fig. 2.5); each of these deformations has its own elastic constant, giving rise to the Frank-Oseen free energy density [45]

$$\mathcal{F} = \frac{K_1}{2}(\nabla \cdot \vec{n})^2 + \frac{K_2}{2}(\vec{n} \cdot (\nabla \times \vec{n}))^2 + \frac{K_3}{2}(\vec{n} \times (\nabla \times \vec{n}))^2, \tag{2.4}$$

where $K_1$ corresponds to the elastic constant for the splay deformations, $K_2$ is the elastic constant for the twist deformations, and $K_3$ is the elastic constant for the bend deformations. If the liquid crystal is subject to electric or magnetic fields, then those energy densities are added accordingly. These deformations occur on a much larger scale than the molecular size, allowing us to neglect the medium structure at the molecular scale associating energy contributions to specific macroscopic deformations [45, 46, 50].

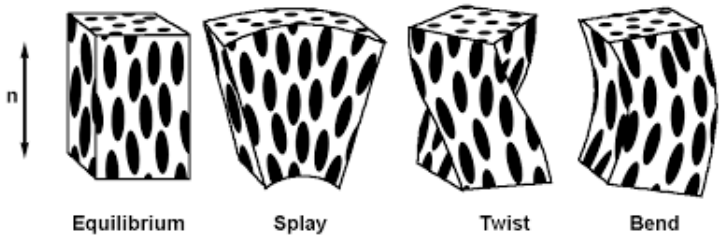


Figure 2.5: Principal deformations on a nematic liquid crystal [52].

## 2.2 Optical Response and Nematicons

Nematic liquid crystals are birefringent materials, meaning that their refractive index depends on the propagation direction and polarization of light. Birefringence is responsible for the phenomenon of double refraction whereby a ray of light incident upon a birefringent material, is split by polarization into two rays with slightly different paths, as seen in Fig. 2.6.

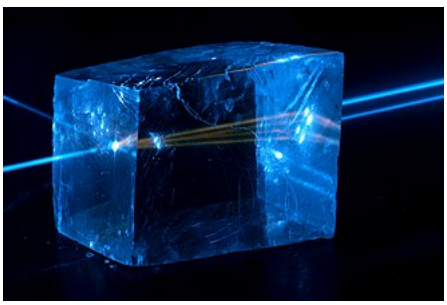

Figure 2.6: Fluorescence in calcite crystal and birefringence as laser beam splits in two while travelling from left to right [53].

When a light beam enters a birefringent material, it splits into ordinary and extraordinary rays. The two rays travel at different velocities and get out of phase. In the case of a nematic liquid crystal, the dielectric tensor in the director

frame of reference can be represented as [50].

$$\bar{\bar{\epsilon}} = \begin{pmatrix} \epsilon_\perp & 0 & 0 \\ 0 & \epsilon_\perp & 0 \\ 0 & 0 & \epsilon_\parallel \end{pmatrix} \tag{2.5}$$

Correspondingly, two distinct refractive indexes can be introduced, $n_\parallel = \sqrt{\epsilon_\parallel/\epsilon_0}$ and $n_\perp = \sqrt{\epsilon_\perp/\epsilon_0}$, where $\epsilon_0$ is the vacuum dielectric permeability and $\Delta n = n_\parallel - n_\perp$ is the birefringence. Light propagating parallel to the optical axis obeys the laws of normal refraction and is governed by the refractive index $n_\perp$ regardless of its specific polarization. This light ray is the *ordinary ray* mentioned earlier. However, a ray propagating in any other direction but with a polarization perpendicular to that of the ordinary ray travels with a velocity that is direction-dependent, and corresponds to the *extraordinary ray*, and will be governed by an extraordinary refractive index. For nematic liquid crystals, a linearly-polarised light beam yields an extraordinary refractive index increase given by [15]

$$n_e(\phi) = \frac{n_\parallel n_o}{\sqrt{n_\parallel^2 \cos^2\phi + n_o^2 \sin^2\phi}} \tag{2.6}$$

where $\phi$ is the angle between the beam and the optical axis. Here, $n_\parallel$ is the refractive index that is parallel to the nematic director $\hat{n}$, while $n_0 = n_\perp$ is the linear refractive index for an ordinary beam, perpendicular to the director.

When a homogeneous layer of nematic liquid crystal (NLC) is subjected to a low-frequency electric field, the molecules will tend to align perpendicular to the electric field if the dielectric anisotropy ($\epsilon_a = n_\parallel^2 - n_\perp^2$) is negative, and rotates towards the electric field if the electric anisotropy is positive. This is to minimize the dipolar interaction between the molecules and the electric field. Due to the competing effects of the torque generated by the applied electric field and the intrinsic elastic torque generated by the liquid-crystalline medium, an effective reorientation will occur when the electric torque overcomes the elastic one. Thus, above the critical voltage at which this balance occurs (known as *the Freederickz transition voltage* [46, 54]), the molecules will rotate until electric torque balances with elastic forces (c.f. Figure 2 .8). In the process, the refractive index of the nematic increases, thereby giving rise to positive lensing along the axis of a bell-shaped beam. When the reorientation effect is large enough, or in other words, when the refractive index increases sufficiently and the self-focusing balances natural diffraction )(c.f. Figure 2.7), a *nematicon* [59] is excited i.e a lightwave coupled with a matter distortion propagates down the cell with an invariant (or cyclically breathing) transverse profile. The term *nematicon* was first coined by Assanto et al. in 2003 [55] to denote self-trapped light beams in nematic liquid crystalline systems.

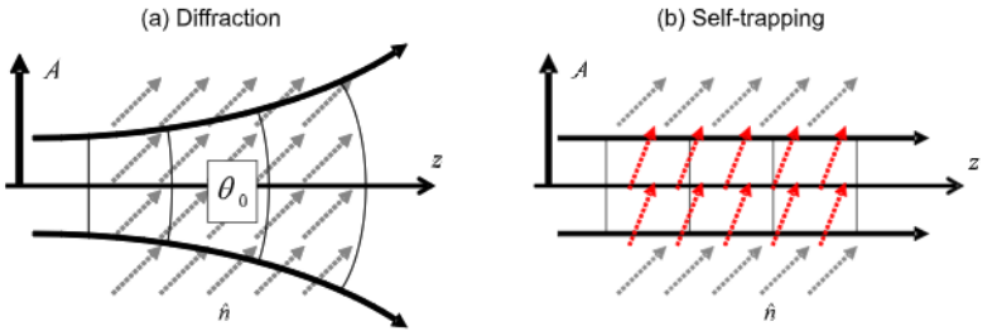


Figure 2.7: Self-confinement through reorientation and its physics in NLC. (a) A beam launched along $Z$ in homogeneously aligned NLC diffracts. (b) As reorientation is induced, the extraordinary refractive index increases and mediates beam self-focusing. When self-focusing balances diffraction, the beam becomes self-trapped in the waveguide sustained by light-induced reorientation [16].

Figure 2.8 shows a typical planar glass cell used in the experimental observation of nematicons [15]. The cell consists of two glass slides parallel to each other with a layer of commercially available NLC mixture (E7 or 5CB) filled between them. Indium-tin-oxide (ITO) film electrodes on the internal surfaces allow a low-frequency voltage to be applied across the NLC thickness. A third glass slide seals the cell entrance to avoid the formation of an undesired meniscus at the air-NLC interface that might alter the polarization and phase of an input beam [57]. The director is assumed to lie in the $yz$ plane, while an extraordinary light beam polarized in the $xz$ plane is launched into the cell using a microscopic objective [57]. Experimentally, by applying an external low-frequency electric field (also known as *bias*) the director orientation can be adjusted, this introduces a *pre-tilt* field across the cell that allows the molecules to overcome the Freedericksz transition threshold and provoke a reorientational response at lower optical powers. In principle, this pre-tilt is not needed if the optical beam has sufficient power, but it reduces unwanted thermal effects that can raise the temperature of the liquid crystal above the nematic phase threshold.

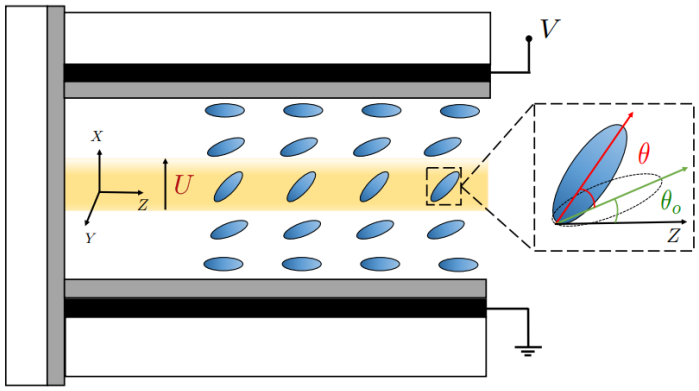


Figure 2.8: Sketch of the side view of a typical NLC cell and propagation geometry. A bright nematicon is generated when a linear-polarised laser beam is launched through a focusing nematic liquid crystal (yellow region). The far-right inset dashed box exhibits the angular positions of a nematic molecule with respect to the direction of the propagation $Z$ before and after releasing the light beam through the nematic cell. Reproduced from [56].

The pre-tilt can be achieved by different methods usually involving a change in the anchoring conditions at the boundaries of the NLC cell. One method is coating the glass slide interfaces bounding the cell with Polyvinyl alcohol (PVA) and then rubbing them, this produces a slight change in the molecular anchoring and director orientation at the boundaries and has a knock-on effect on the orientation of the molecules in the cell [62]. Another method is to mix the NLC with a small amount of dye dopant and then apply an external field coupled with UV light that causes an interaction between dye-doped nematic molecules and the molecules on the inner surface of the glass boundary. This interaction can be tuned to change the anchoring condition of the nematic molecules at the boundaries [58] (See Fig. 2.9)

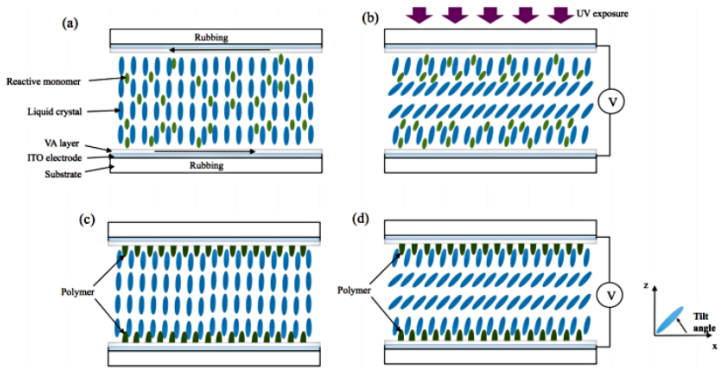


Figure 2.9: Creation of a pre-tilt angle in an NLC cell. (a) Uniform tilt is induced by rubbing the substrate. (b) A combined application of UV light and an electric field pins reactive molecules to the substrate surface. (c) Director orientation without external voltage. (d) Pre-tilted orientation with externally applied voltage. [58]

Figure 2.10 shows experimentally the emergency of nematicons after a linearly $x$-polarised Gaussian beam was launched into a planar NLC cell. Figure 2.10 (a) showcases the importance of the pre-tilt as a weak beam could not overcome the Freedericksz transition threshold and is diffracted along the cell. On the other hand, when a pre-tilt was induced, the nonlinear molecular reorientation enables self-focusing which balances natural diffraction and leads to a stable solitary wave propagating unchanged over a distance of 1 mm, roughly 20 times the diffraction length [57].

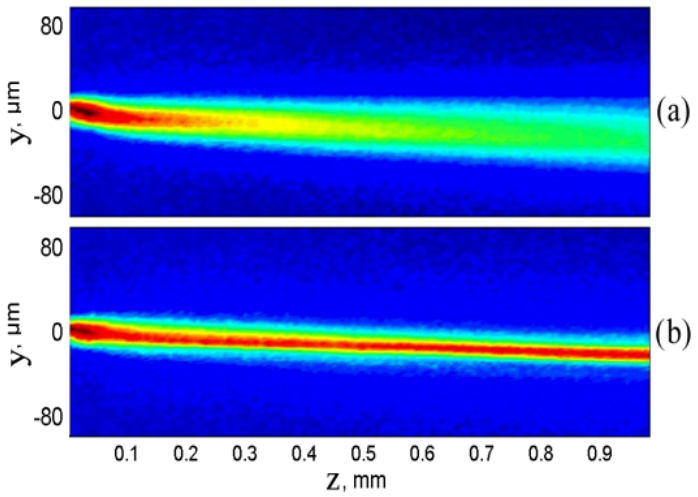


Figure 2.10: Beams resulting from a 4.2mW power argon-ion laser oscillating at 513 nm. (a) No pre-tilt is applied. (b)A low-frequency pre-tilt electric field of 0.8 V at 1kHz is applied across the cell. Image taken from [57]

In principle, nematicon propagation can be described by the Maxwell equations. However, the resulting system of equations is too complex to enable any mathematical modelling or physical interpretation, with numerical solutions the only remaining alternative [60, 61]. Since most typical experimental conditions can be assumed to be weakly nonlinear and with a slowly varying electric field envelope for the beam, it is possible to reduce the Maxwell equations to an NLS-type equation [3, 63] coupled to another PDE describing the nonlinear response of the medium (See Chapter 3 for a derivation of the nematicon equations).

In their most simplified form, the nematicon equations are given by

$$i\frac{\partial u}{\partial z} + \frac{1}{2}\nabla_\perp^2 u + 2\theta u = 0, \tag{2.7}$$

$$\nu\nabla_\perp^2\theta - 2q\theta + 2|u|^2 = 0. \tag{2.8}$$

where $u$ is the complex envelope of the beam's electric field, $\theta$ is the optically induced rotation of the nematic director due to the electric field of the light beam, $q$ is a measure of the strength of the external static electric field used to

pre-tilt the nematic molecules and $\nu$ measures the strength of the elastic response of the molecules and quantifies the nonlocality of the medium, with small values of $\nu$ corresponding to the local limit, while large values of $\nu$ correspond to the highly nonlocal limit. If $q = 0$ i.e. the pre-tilt is not included, the director equation (2.8) is simplified to the Poisson equation

$$\nu\nabla_\perp^2\theta + 2|u|^2 = 0. \tag{2.9}$$

Equations (2.7) and (2.8) are the basic system of coupled PDEs that govern nonlinear optical beam propagation in pre-tilted NLC cells. While they have been introduced in the context of light beam propagation in NLC, they are much more general. In particular similar equations apply to optical beams in photorefractive crystals [64] and thermo-optical materials [65]. They also arise in connection with the Schrödinger-Newton equations in astrophysics. Here, the coupled system consists of the Schrödinger equation for a particle moving in its own gravitational field, which is produced by its own probability density through the Poisson Equation [66]. Solitary wave solutions of the Schrödinger-Poisson systems (2.7) and (2.9), have been used to model dark matter [67] and the interaction between ordinary and dark matter [68]. As they apply to a broad spectrum of physical phenomena, the nematicon system can be considered a canonical model of nonlinear highly nonlocal waves.

Reorientational NLCs are a self-focussing medium so that their refractive index $n_e$ increases with beam intensity $|u|^2$. However, a light-induced reduction in the order parameter through the introduction of azo-dyes, can turn the NLC into a self-defocussing medium, so that dark solitary waves can be excited [69] i.e. solitary waves which are dips in a background carrier wave, rather than the intensity hump of bright solitons. For a defocussing NLC, the electric field equation (2.7) becomes

$$i\frac{\partial u}{\partial z} + \frac{1}{2}\nabla_\perp^2 u - 2\theta u = 0. \tag{2.10}$$

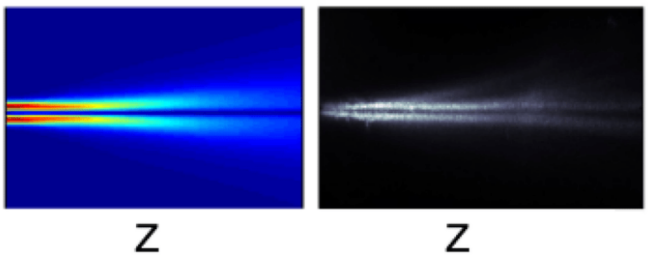


Figure 2.11: Left: Simulation of a dark nematicon. Right Experimental dark nematicon formed at high power (4 mW). Image taken from [70].

## 2.3 Nematicons in Waveguide Photonics

### 2.3.1 Birefringent Walk-off

An electromagnetic plane wave propagating with wave normal in a NLC can be described as the superposition of *ordinary* ($o-$) and *extraordinary* ($e-$) polarized wave components. As NLCs behave as birefringent uniaxial materials, extraordinary-wave nematicons display *birefrigent walk-off*, that is, the beam energy travels forming a nonzero angle (Usually denoted $\delta$) with respect to the wave-vector [50]. In other words, their e-wave flux vector (Poynting vector $\mathbf{S}$) is not collinear with the wave vector $\mathbf{k}$.

For a light beam propagating in NLC with its wavevector $\mathbf{k}$ at an angle $\theta$ with respect to the director $\mathbf{n}$. A linearly polarized e-wave (with the electric field $\mathbf{E}$ coplanar with $\mathbf{n}$ and $\mathbf{k}$) has a phase velocity $c_e$ given by

$$c_e = \frac{c_0}{n_e\theta} = c_0 \frac{[(n_\perp^2 - n_\parallel^2)\sin^2\theta + n_\parallel^2]^{1/2}}{n_\perp n_\parallel}, \tag{2.11}$$

where $c_0$ is the speed of light in vacuum. Correspondingly, the walk-off angle $\delta$ is given by

$$\delta(\theta) = -\frac{1}{n_e(\theta)}\frac{dn_e(\theta)}{d\theta} \tag{2.12}$$

Figure 2.12 illustrates the birefringent walk-off effect for near-infrared beams with wavevector $\mathbf{k}$ parallel to the $z$ axis in various cases: ordinary wave-beam at the input; low power extraordinary wave beam launched with a $y$-polarized electric field; finally a 2 mW self-confined nematicon walking-off in the observation plane. Geometry corresponds to a standard planar cell with uniform anchoring at $\theta = 60°$ on the lower and upper interfaces parallel to the principal plane $yz$. The interfaces are treated by a pre-tilting method to ensure the anchoring of the molecules in the prescribed direction. For the high birefringence of NLC, the walk-off can assume large values (up to $7-9°$ in commercial E7), affecting the nematicon dynamics. Moreover, the walk-off is sensitive to the optical beam power and nonlinear corrections to the walk-off could affect the nematicon direction of propagation, Peccianti et al.[71] showed that it can be tuned by several degrees allowing power-dependent optical steering.

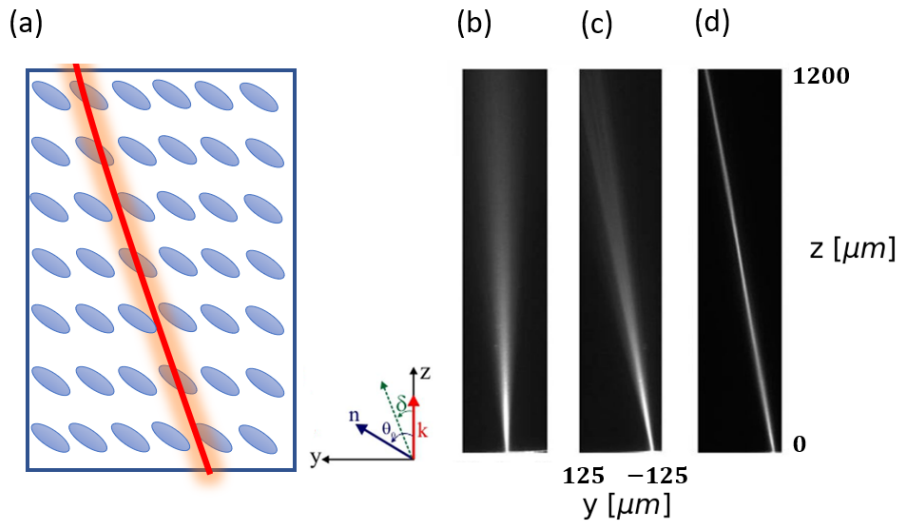


Figure 2.12: (a) Sketch of a typical planar NLC cell. (b) Photograph of a 3 $\mu$m waist near-infrared beam polarized as an ordinary wave diffracting along $z$. (c) extraordinary-wave low power beam diffracting in the walk-off direction. (d) Extraordinary wave high power beam (2 mW) forming a nematicon in the walk-off direction with $\delta \approx 6°$. Image adapted from [15].

### 2.3.2 Light-induced Waveguides

Nematicons are stable and robust self-confined beams that can propagate diffractionless within their own light-induced channel waveguide. This waveguide nature of a nematicon leads to its ability to guide co-polarized $e$-wave weak signals (also known as *probes*), regardless of their wavelength [72, 73]. Noteworthy, nematicon waveguides can trap and transmit weak signals of any modulation format and spectral content, including high-bit data streams for optical communications. Due to the high NLC nonlocality, nematicon waveguides exhibit a large numerical aperture; hence, the in-coupling of a weak signal is efficient even when the waveguide axis and probe are misaligned. Furthermore, nematicon waveguides can be multimode and confine several extraordinary-polarized guided modes [74, 75]. Figure 2.13 shows an example of weak signal steering in a nematicon optical waveguide.

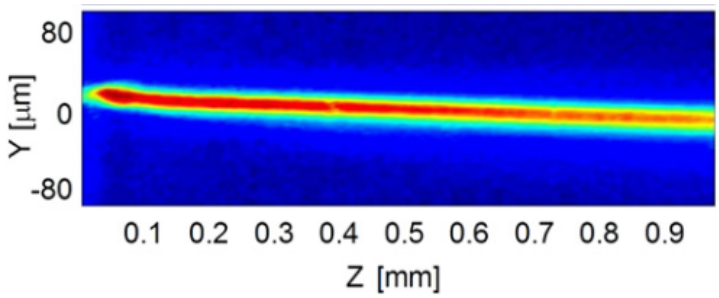


Figure 2.13: Measure evolution of a low-power (30 $\mu$W) He-Ne beam colaunched and copolarized with a 4.2 mW $Ar^+$ beam. Image taken from [15].

Nematicons are waveguides dynamically induced by light, therefore, they require the presence of a relatively intense input beam to exert guidance over additional light signals. Light-induced waveguides are relevant as they are shaped directly by the optical beam, rather than being realized by external means into the medium. Furthermore, a nematicon waveguide can be permanently imprinted in the material even after the input beam has been removed or turned off, changing real-time dynamic waveguides into permanent waveguides.

This concept was experimentally implemented via polymerization in a photopolymerizable NLC mixture, decoupling spatial solution generation from material polymerization [76]. The used material consisted of a doped NLC mixture with a host NLC and photopolymerizable guest compounds as dopants. A nematicon was generated by a $y$-polarized input 3mW Gaussian beam of wavelength $1.064\mu$m, focused to a waist of $4\mu$m and launched in the midplane of the sample. Once the nematicon was self-confined in the principal plane $yz$, then the whole sample was illuminated by a continuous UV light. Maintaining the illumination at constant intensity the material started to polymerize and the waveguide was permanently sculpted in the soft matter. Figure 2.14 illustrates the planar cell and nematicon moulding process.

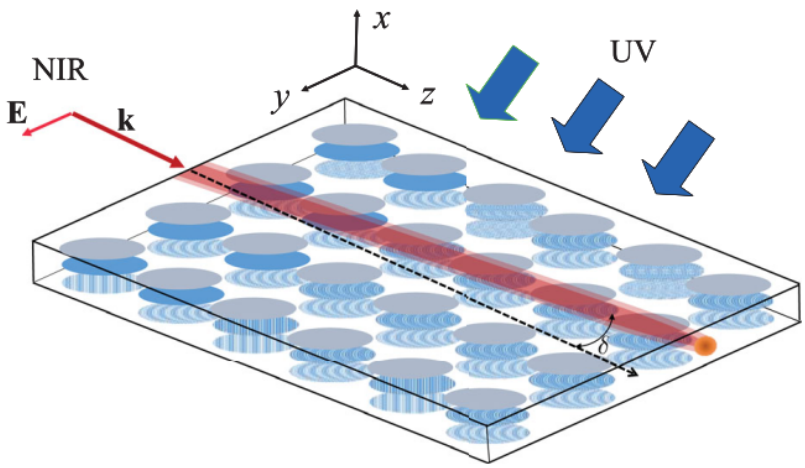


Figure 2.14: Sketch of the planar $100\mu$m-thick polymerizable NLC cell, optic axis is set at $\theta = 45°$ in the plane $yz$, a near-infrared (NIR) e-wave input beam is used to induce the waveguide and external UV illumination to initiate polymerization. Figure reproduced from [77].

The waveguiding effect of nematicons has been the basis for research in potential future all-optical routing and logic devices based on NLC [78, 79]. The advantage of a nematic liquid crystal as the intermediary medium is that there are no fixed circuits, unlike wired-based devices, so any path through the cell is possible. Potential applications of nematicons and their interactions were demonstrated in the framework of all-optical signal processing and readressing [80]. These results

are part of a growing interest in researching and developing all-optical analogues of electronics, to circumvent limitations associated with electronic devices, for example, in optical fibre communications, the process of converting optical signals to electrical ones uses extra power (generating heat) that can be expensive is the conversion has to happen quickly or regularly. The efficiency of optical communications could be increased if devices are designed to operate in an all-optical regime.

The magnitude and response speed of the underlying nonlinear mechanisms vary very widely, some studies emphasize the speed performance while others stress the optical power required [81, 82, 83, 84]. The saturating nature of the nonlinearity of nematics means that nematicons can be excited for relatively low optical power levels ($\sim$ 2 mW). However, whilst the nonlinear effect is strong, it is also slow ($\sim$ 0.1 s) [15, 50], which limits severely their use in optoelectric commercial applications in telecommunications, where current electrical interconnects can switch at microsecond speed, all-optical interconnects using nematicons would react over seconds [62]. Nonetheless, one of the main focuses of this thesis: all-optical diode devices has attracted interest in the last decades from a fundamental standpoint in proof-of-concept research [85].

### 2.3.3 Optical Isolators

A diode is an essential element in most electronic circuits, permitting a current in the forward direction and blocking it in the backward direction. We call a device an optical isolator or all-optical diode if it blocks light in one direction but allows light to pass in the reverse direction. This is important, for example, to shield equipment on its input side, from the effects of conditions on its output side. The use of an optical isolator improves the overall designability of a system as it suppresses spurious interference and undesired light interactions. One of the most important procedures to create optical isolation is via time-reversal symmetry breaking [86], examples include magneto-optical isolators [87], nonlinear optical structures [88] and time-dependent optical structures [89].

To describe at a basic level a linear optical isolator, we consider an optical device inside a domain $\Omega$. The device is assumed to be linear, time-independent and reciprocal. The only way for light to enter $\Omega$ is through lossless reciprocal waveguides, called *ports* (c.f. Figure 2.15). The surface $\Omega$ is chosen such that all waveguides and their guided modes are aligned normally to $\Omega$ and the waveguides and their guided modes are assumed to be essentially non-overlapping.

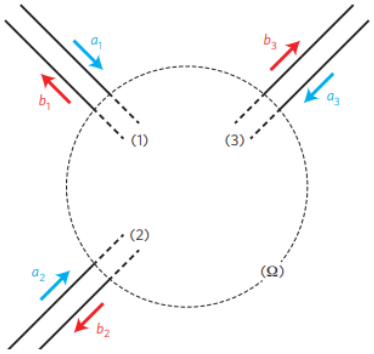


Figure 2.15: General optical circuit inside domain Ω. Reproduced from [31]

In the case of electronic circuits, different parameters can be used to describe their properties, such as impedance, admittance, transmission and scattering matrices [91]. These parameters determine some properties without obtaining an exact solution at all points in space. Now, when an external wave interacts with an optical device, we can study the output it produces for a given input, without solving all the electromagnetic fields inside the device. This establishes a concrete parallel between electronic circuits and optical circuits [92].

The scattering parameters ($S$ parameters) relate the input signal to the output signals, giving information about the reflected or transmitted power through the optical system. In matrix form, the scattering parameters for an $N-$port device can be written as

$$\begin{bmatrix} b_1 \\ b_2 \\ \vdots \\ b_N \end{bmatrix} = \begin{bmatrix} S_{11} & S_{12} & \dots & S_{1N} \\ S_{21} & & & \vdots \\ \vdots & & & \\ S_{N1} & & & S_{NN} \end{bmatrix} \begin{bmatrix} a_1 \\ a_2 \\ \vdots \\ a_N \end{bmatrix}, \tag{2.13}$$

where $a_i$ and $b_i$, with $i = 1, \dots, N$ represent the incoming and outgoing signals, respectively (c.f. Figure 2.15), the scattering coefficients $S_{ij}$ relate the normalized amplitudes of an incoming and outgoing signal, namely, an input amplitude of 1 injected to port $i$ produced an output $S_{ij}$ at port $j$.

With this definition, the tangential components of the electromagnetic fields in each port in Ω have the form [31]

$$\mathbf{E}_{t,i} = (a_i + b_i)\mathbf{e}_i \tag{2.14}$$
$$\mathbf{H}_{t,i} = (a_i - b_i)\mathbf{h}_i. \tag{2.15}$$

Here, the vectors $\mathbf{e}_i$ and $\mathbf{h}_i$ correspond to the electric and magnetic fields in port $i$. Additionally, all ports must be linearly independent, satisfying the orthogonality condition [90]

$$\int\int_{\Omega} \mathbf{e}_i \cdot \mathbf{h}_j^* dS = \delta_{i,j}. \tag{2.16}$$

where $\delta_{i,j}$ is the Kronecker delta and the integration is over the cross-section of the port.

The scattering matrix formalism allows a simple definition of the reciprocity condition given by

$$S_{ij} = S_{ji}. \tag{2.17}$$

We will be especially interested in two-port waveguide devices. Here, isolation imposes a particular requirement on the elements of the scattering matrix that connects its two ports. There needs to be a pair of modes, one belonging to each port, such that transmission from mode $\mu$ in port 1 to mode $\nu$ in port 2 is essentially non-zero, whereas the transmission from mode $\nu$ in port 2 to mode $\mu$ in port 1 is close to zero (c.f Figure 2.16 sketch an isolator that allows transmission in only one direction). It is unimportant where the energy in the latter case goes: it can be dissipated in the device, transmitted to a third port or radiated away.

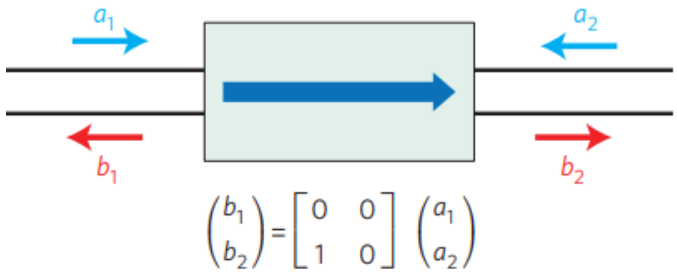


Figure 2.16: Simplest ideal isolator with 2 single-mode waveguide port and their respective scattering matrix. Image taken from [31]

### 2.3.4 Nematicon-based optical diode

Examining the generation and path of extraordinary-wave nematicons in planar cells of NLC when launching identical beams from opposite ends of samples with modulated background distributions of the optic axis gives valuable insights into asymmetrical power transmission, time-symmetry breaking and the realization of efficient all-optical diodes [31]. Figure 2.17 illustrates the operation of a nematicon-based optical diode where soliton waveguides exhibit non-reversible routing.

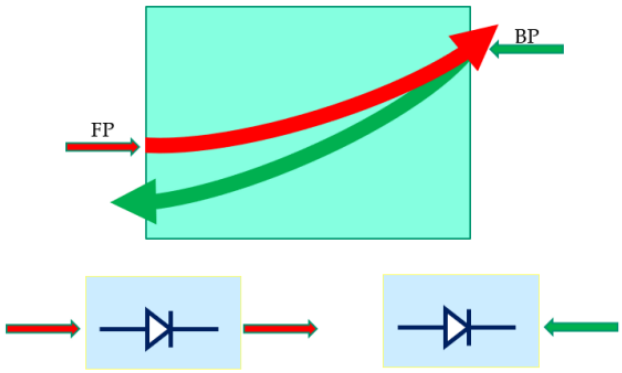


Figure 2.17: Artistic rendering of a nematicon-based all-optical diode

The first research direction will be to complete a numerical study of conditions that allow separation between FP and BP nematicons. To this end, two cases will be considered, (i) a varying director orientation across the propagation coordinate $z$ and (ii) along the transverse coordinate $y$ (c.f. Figure 2.18). This will be detailed in Chapter 4.

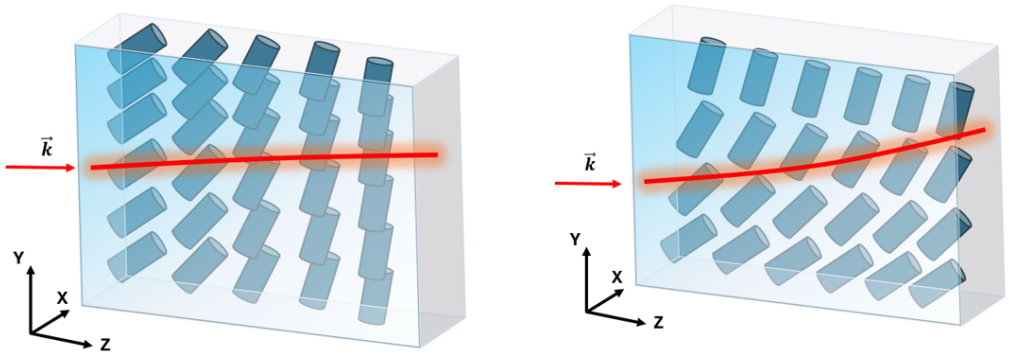


Figure 2.18: Left: Sketch of planar cell with preset orientation modulated along direction $z$ showing input beam with wavevector $\mathbf{k}$. Right: Arrangement of a planar cell with background orientation modulated across the $y$ direction.

# Chapter 3

# Mathematical Backgrounds: Nematicon Equations

We consider the propagation of a linearly polarized, coherent light beam in a planar cell with undoped, positive ($\Delta n = n_{\parallel} - n_{\perp} > 0$) uniaxial NLC. The extraordinary polarized beam is taken to initially propagate forward in the $z$ direction, with electric field $E$ oscillating in the $y$ transverse direction and $x$ completing the coordinate triad. To eliminate the Freéderickz threshold [45] and maximize the nonlinear response [97], the cell interfaces perpendicular to $x$ are rubbed so that the molecular director makes an angle $\theta_0$ with $z$ in the $(y, z)$ plane in the absence of light. An additional rotation $\theta_b(y, z)$ is given to the nematic director to modulate the uniaxial medium. Finally, the beam causes an additional all-optical reorientation denoted by $\psi$. Hence, the total angle of the optic axis to the $z$ direction is $\Theta = \theta_0 + \theta_b(y, z) + \psi(x, y, z)$ [45].

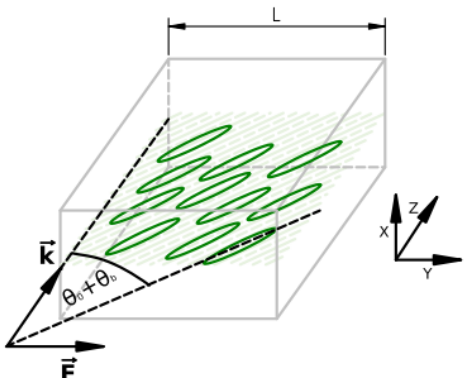


Figure 3.1: Sketch of the configuration and NLC alignment. The input beam is linearly polarized along $y$. The light beam is input at $y = y_0$ at $z = 0 (y_0 = 0$ in the figure). Figure reproduced from [61].

## 3.1 Beam Propagation and Elastic Theory

To study the nonlinear evolution of a light beam in NLCs, we consider the fully vectorial beam propagation method (FVBPM) [60] in conjunction with the

Frank-Oseen model for the NLC response [50]. The FVBPM can be derived from Maxwell's equations [98], considering harmonically oscillating electric and magnetic fields in an anisotropic dielectric:

$$\frac{\partial H_z}{\partial y} - \frac{\partial H_y}{\partial z} = i\omega\epsilon_0(\epsilon_{11}E_x + \epsilon_{12}E_y + \epsilon_{13}E_z), \tag{3.1}$$

$$\frac{\partial H_x}{\partial z} - \frac{\partial H_z}{\partial x} = i\omega\epsilon_0(\epsilon_{21}E_x + \epsilon_{22}E_y + \epsilon_{23}E_z), \tag{3.2}$$

$$\frac{\partial H_y}{\partial x} - \frac{\partial H_x}{\partial y} = i\omega\epsilon_0(\epsilon_{31}E_x + \epsilon_{32}E_y + \epsilon_{33}E_z), \tag{3.3}$$

$$H_x = -\frac{1}{i\mu_0\omega}\left(\frac{\partial E_z}{\partial y} - \frac{\partial E_y}{\partial x}\right), \tag{3.4}$$

$$H_y = -\frac{1}{i\mu_0\omega}\left(\frac{\partial E_x}{\partial z} - \frac{\partial E_z}{\partial x}\right), \tag{3.5}$$

$$H_z = -\frac{1}{i\mu_0\omega}\left(\frac{\partial E_y}{\partial x} - \frac{\partial E_x}{\partial y}\right). \tag{3.6}$$

Here $\vec{E} = (E_x, E_y, E_z)$ and $\vec{H} = (H_x, H_y, H_z)$ are the electric and magnetic fields, respectively, $\epsilon$ is the electric permittivity tensor, $\omega$ is the angular frequency, and $\mu_0$ is the vacuum permeability. We note that the director and the electric field of the beam lie in the principal plane $(y, z)$ and the nonlinear reorientation occurs in this plane; hence, the azimuthal components can be neglected and the director can be written in polar coordinates as $\vec{n} = (0, \sin\Theta, \cos\Theta)$.

Then, the electric tensor in Equations (3.1-3.7) is given by

$$\bar{\bar{\epsilon}} = \begin{pmatrix} \epsilon_\perp & 0 & 0 \\ 0 & \epsilon_\perp + \Delta\epsilon\sin^2\Theta & \Delta\epsilon\sin\Theta\cos\Theta \\ 0 & \Delta\epsilon\sin\Theta\cos\Theta & \epsilon_\perp + \Delta\epsilon\sin^2\Theta \end{pmatrix}, \tag{3.7}$$

with $\Delta\epsilon = n_\parallel^2 - n_\perp^2 > 0$ the optical anisotropy. The electromagnetic equations (3.1-3.7) are coupled to the NLC response, given by the Frank-Oseen energy density [50]

$$\mathcal{F} = \frac{K_1}{2}(\nabla\cdot\vec{n})^2 + \frac{K_2}{2}(\vec{n}\cdot(\nabla\times\vec{n}))^2 + \frac{K_3}{2}(\vec{n}\times(\nabla\times\vec{n}))^2 - \frac{1}{2}\epsilon_0\Delta\epsilon(\vec{n}\cdot\vec{E})^2. \tag{3.8}$$

Here $K_1$, $K_2$, and $K_3$ are the Frank elastic constants for the splay, twist and bend deformations of the director $\vec{n}$, respectively [45] and the last term corresponds to the energy associated to the field-dipole interaction.

Since the changes in the orientation along $z$ are slow compared with the wavelength of light, the derivatives with respect to $z$ can be neglected. The elastic response is given by the minimization of the Frank-Oseen energy, so the Euler-Lagrange equations determine it

$$\frac{\partial}{\partial x}\frac{\partial \mathcal{F}}{\partial \Theta_x} + \frac{\partial}{\partial y}\frac{\partial \mathcal{F}}{\partial \Theta_y} - \frac{\partial \mathcal{F}}{\partial \Theta} = 0. \tag{3.9}$$

Then, the all-optical director rotation $\Theta$ is governed by the equation

$$K_2\Theta_{xx} + (K_1\cos^2\Theta + K_3\sin^2\Theta)\Theta_{yy} - \frac{1}{2}\sin 2\Theta(K_1 - K_3)(\Theta_y)^2 + \frac{\epsilon_0\Delta\epsilon}{2}[2E_yE_z\cos 2\Theta - \sin 2\Theta(E_y^2 - E_z^2)] = 0. \tag{3.10}$$

The full system of equations governing the propagation of a light beam in a non-uniform NLC cell is extensive and can only be solved numerically. However, typical light beams are of milli-watt power and much narrower than the length of the cell, for such beams the optical response $\psi$ is small in comparison to the imposed director background ($|\psi| \ll \theta_b$) we can then apply the Slowly Varying Envelope Paraxial Approximation (SVEA) [15, 100], effectively neglecting $E_x$ and $E_z$, the equations governing the evolution of a paraxial beam with wavevector $\vec{k} = k_0\hat{z}$ in NLC are then [50]

$$ik_0n_e\frac{\partial E_y}{\partial z} + 2ik_0n_e\Delta(\Theta)\frac{\partial E_y}{\partial y} + \nabla_\perp^2 E_y + k_0^2(n_\perp^2\cos^2\Theta + n_\parallel^2\sin^2\Theta - n_\perp^2\cos^2\theta_0 - n_\parallel^2\sin^2\theta_0)E_y = 0, \tag{3.11}$$

for the electric field of the light beam and

$$K\nabla_\perp^2\Theta + \frac{1}{4}\epsilon_0\Delta\epsilon|E_y|^2\sin 2\Theta = 0. \tag{3.12}$$

for the medium response. Here, the single elastic constant approximation has been made so that the elastic constants for twist, bend and splay are taken equal to $K$ in (3.10). The wavenumber $k_0$ of the input light beam is intended as in a vacuum, and $n_e$ is the background extraordinary refractive index of the NLC [50],

$$n_e^2(\Theta) = \frac{n_\perp^2 n_\parallel^2}{n_\parallel^2\cos^2\Theta + n_\perp^2\sin^2\Theta} \tag{3.13}$$

The coefficient $\Delta$ is related to the birefringent walk-off $\delta$ of the extraordinary wave beam, with $\tan\delta = \Delta$ in the $(y, z)$ plane, and is given by

$$\Delta(\Theta) = \frac{\Delta\epsilon\sin 2\Theta}{\Delta\epsilon + 2n_\perp^2 + \Delta\epsilon\cos 2\Theta} \tag{3.14}$$

which depends nonlinearly on the beam power through the reorientation $\psi$, but can be taken as $\Delta(\Theta) \approx \Delta(\theta_0 + \theta_b)$ in the weakly nonlinear regime.

The single constant approximation $K_1 = K_2 = K_3 = K$ is one of the most common approaches adopted when describing the molecular reorientation in NLCs. Sala and Karpierz [98] showed that no significant differences existed between results obtained using all Frank elastic constants and the single constant

approximation, and choosing appropriate values of $K$ is more relevant to model the phenomena under study.

In their full form, the nematic equations (3.11) and (3.12) are difficult to solve, or even find approximate solutions for, but a low-power approximation can be made so that asymptotic solutions can be derived. For low-power beams, the optical reorientation $\psi$ is much less than the imposed orientation $\theta_0(0) + \theta_b$. In this low-power limit, the trigonometric functions can be expanded in Taylor series about $\theta_0(0) + \theta_b$ and equations (3.11) and (3.12) become

$$\begin{aligned} 2ik_0 n_e \frac{\partial E_y}{\partial z} + 2ik_0 n_e \Delta(\theta_0(0) + \theta_b + \psi)\frac{\partial E_y}{\partial y} \\ +\nabla_\perp^2 E_y + k_0^2 n_\perp^2 [\cos^2(\theta_0(0) + \theta_b) - \cos^2\theta_0(0)]E_y \\ +k_0^2 n_\parallel^2 (\sin^2(\theta_0(0) + \theta_b) - \sin^2\theta_0(0)]E_y \\ +k_0^2 \Delta\epsilon \sin 2(\theta_0(0) + \theta_b)\psi E_y = 0, \end{aligned} \tag{3.15}$$

and

$$K\nabla_\perp^2 \psi + \frac{1}{4}\epsilon_0 \Delta\epsilon |E_y|^2 \sin 2(\theta_0(0) + \theta_b) = 0. \tag{3.16}$$

Note that this derivation does not depend on whether the background director modulation $\theta_b$ is transverse $\theta_b(y)$ or longitudinal $\theta_b(z)$, therefore this is the most general set of equations that govern nematicon propagation in a modulated NLC cell.

Now, redefining variables $\theta = \theta_0 + \theta_b$ and considering a purely longitudinal modulation,

$$\theta = \theta(z) = \theta_0 + (\theta_L - \theta_0)\frac{z}{L}, \tag{3.17}$$

where $L$ is the length of the cell, $\theta_0$ and $\theta_L$ are the director's angle at $z = 0$ and $z = L$, respectively. The electric field equation (3.15) can be then simplified using the phase transformation

$$E_y \to \tilde{E}_y \exp\left\{\frac{ik_0}{2n_e}\int_0^z \left[\Delta\epsilon(\sin^2\theta - \sin^2\theta_0)\right]\right\}. \tag{3.18}$$

After this transformation, the nematic equations become

$$2ik_0 n_e \frac{\partial \tilde{E}_y}{\partial z} + 2ik_0 n_e \Delta[\theta + \psi]\frac{\partial \tilde{E}_y}{\partial y} + \nabla_\perp^2 \tilde{E}_y + k_0^2 \Delta\epsilon[\sin(2\theta)]\psi\tilde{E}_y = 0, \tag{3.19}$$

$$K\nabla_\perp^2 \psi + \frac{1}{4}\epsilon_0 \Delta\epsilon |\tilde{E}_y|^2 \sin(2\theta) = 0. \tag{3.20}$$

The reduced equations can be set in non-dimensional form via the transformations [98]

$$x = WX, \quad y = WY, \quad z = BZ, \quad \tilde{E}_y = Au, \tag{3.21}$$

where

$$W = \frac{\lambda}{\pi\sqrt{\Delta\epsilon \sin 2\theta_0}}, \quad B = \frac{2n_e\lambda}{\pi\Delta\epsilon \sin 2\theta_0}, \quad A^2 = \frac{2P_0}{\pi\Gamma W_b^2}, \quad \Gamma = \frac{1}{2}\epsilon_0 c n_e, \quad (3.22)$$

for a reference Gaussian input beam power of $P_0$, width $W_b$ and wavelength $\lambda$ ($\lambda = 2\pi/k_0$) [99].

So the nematicon equations for a $z$-modulated background in non-dimensional form are

$$i\frac{\partial u}{\partial Z} + i\gamma\Delta(\theta+\psi)\frac{\partial u}{\partial Y} + \frac{1}{2}\nabla^2 u + 2\frac{\sin(2\theta(Z))}{\sin(2\theta(0))}\psi u = 0, \quad (3.23)$$

$$\nu\nabla^2\psi + \frac{\sin(2\theta(Z))}{\sin(2\theta(0))}|u|^2 = 0, \quad (3.24)$$

with the Laplacian $\nabla^2$ in the transverse nondimensional variables $(X, Y)$ and the scaled walk-off $\gamma$ and NLC elasticity $\nu$ factors in these non-dimensional equations are

$$\gamma = \frac{2n_e}{\sqrt{\Delta\epsilon \sin 2\theta_0}}, \quad \nu = \frac{8K}{\epsilon_0\Delta\epsilon A^2 W^2 \sin 2\theta_0}. \quad (3.25)$$

In the case of a uniform NLC, i.e. $\theta = 0$ and neglecting the walk-off effects, Equations (3.23) and (3.24) reduce to the standard form

$$i\frac{\partial u}{\partial z} + \frac{1}{2}\nabla^2 u + 2\psi u = 0, \quad (3.26)$$

$$\nu\nabla^2\psi + 2|u|^2 = 0. \quad (3.27)$$

which corresponds to equations (2.7) and (2.8) without pretilt.

The system of equations (3.23) and (3.24) form a non-dissipative, saturating (the reorientational angle response cannot exceed $\pi/2$), non-linear wave system. If we take into account the unavoidable photon scattering due to dielectric inhomogeneities and the consequent power dissipation, optical losses can be incorporated into the electric field equation (3.23) by adding a damping term

$$i\frac{\partial u}{\partial Z} + i\gamma\Delta(\theta+\psi)\frac{\partial u}{\partial Y} + \frac{1}{2}\nabla_\perp^2 u + 2\frac{\sin(2\theta(Z))}{\sin(2\theta(0))}\psi u = -i\alpha u, \quad (3.28)$$

where $\alpha$ corresponds to the nondimensional attenuation coefficient, with typical experimental values around $\alpha_s = 5$ cm$^{-1}$ [101].

### 3.1.1 Thermal effects

The propagation of light beams in NLC can also be affected by thermal heating, and this can be important for two reasons (i) the refractive indices $n_\perp$ and $n_\parallel$ and the walk-off $\delta$ are temperature dependent [106] and (ii) the nematic mesophase exists in a restricted temperature interval [45] ($-30$ to 61°C for the commercial

mixture E7). If the intensity of the beam is $|E|^2$, the temperature of the nematic is governed by the steady, forced heat equation

$$\kappa\nabla_\perp^2 T = -\alpha\Gamma|E|^2, \quad \Gamma = \frac{1}{2}\epsilon_0 c n_e, \tag{3.29}$$

with $\alpha$ the optical absorption coefficient and $\kappa$ the thermal conductivity.

In common NLC the thermo-optic refractive response is self-defocussing for extraordinary waves, opposite to the reorientation. These two contributions then compete with each other, having as a result the formation of a thermo-reorientational nematicon if focusing dominates defocusing. In some cases, when the two non-linearities are carefully tailored by the introduction of dopants and specific wavelengths are employed to maximise thermal absorption, the (2+1)-dimensional nematicon solution has a central dip with a surrounding ridge, resulting in a nematicon with a volcano profile [105].

Taking into account thermo-reorientational effects into the nematic equations (3.11) and (3.12) [105]

$$2ik_0 n_e \frac{\partial E}{\partial Z} + \nabla_\perp^2 E + k_0^2[n_\perp^2 \cos^2\Theta + n_\parallel^2 \sin^2\Theta - n_\perp^2 \cos^2\theta_0 - n_\parallel^2 \sin^2\theta_0]E = 0, \tag{3.30}$$

$$K\nabla_\perp^2\Theta + \frac{1}{2}\Delta\epsilon_{RF}E_{lf}^2 \sin 2\Theta + \frac{1}{4}\epsilon_0\epsilon_a|E|^2 \sin 2\Theta = 0, \tag{3.31}$$

$$\kappa\nabla_\perp^2 T = -\alpha\Gamma|E|^2, \tag{3.32}$$

where now the refractive indices are taken to depend on the temperature $T$, the parameter $\Delta\epsilon_{RF}$ is the low-frequency anisotropy of the medium and $E_{lf}$ is the external biasing electric field needed to pre-tilt the background nematic molecules.

The presence of a pre-tilt field defined by the low-frequency electric field $E_{lf}$ is necessary to keep a weak thermal dependency of the refractive index. The pre-tilt lowers the optical power needed to overcome the Freedericksz transition and sustain a self-focusing optical soliton, which weakens the thermal defocusing response compared with the focusing director response.

| Typical Parameter Values | | |
|---|---|---|
| Symbol | Parameter | Value |
| $K$ | elastic constant | $1.2 \times 10^{-11}$ N |
| $W_b$ | beam width | $3 \to 7$ $\mu$m |
| $\epsilon_0$ | free-space permittivity | $8.8542$ $\frac{F}{m}$ |
| $\mu_0$ | free-space permeability | $4\pi \times 10^{-7}$ $\frac{kg}{F}\frac{m}{s^2}$ |
| $\epsilon_a$ | optical anisotropy | 0.64 |
| $\alpha_s$ | optical absorption | 5 cm$^{-1}$ |
| $\alpha$ | nondimensional absorption | $10^{-4}$ |
| $\kappa$ | thermal conductivity | $0.7$ $\frac{W}{mK}$ |
| $\lambda$ | incident beam wavelength | 1.064 $\mu$m |
| $n_\parallel$ | extraordinary refractive index | 1.7 |
| $n_e$ | background $e$-index $n_e(\theta_0)$ | 1.63 |
| $n_\perp$ | ordinary refractive index | 1.5 |
| $P_b$ | Gaussian input beam power | $2 \to 20$ mW |
| $\Gamma$ | $\frac{1}{2}\epsilon_0 c n_e$ | $2.39063 \times 10^9$ $\frac{F}{s}$ |
| $\nu$ | elasticity parameter | $\mathcal{O}(100)$ |
| $(h, d, L)$ | typical planar cell size | $(30, 400, 1000)$ $\mu$m |
| $\theta_0$ | angle at $z = 0$ | $10 \to 80°$ |
| $\theta_L$ | angle at $z = L$ | $45 \to 80°$ |

Table 3.1: Typical experimental parameters values considered.

## 3.2 Analytical solutions and related models

The equations (3.23) and (3.24) governing nonlinear light beam propagation in a modulated NLC cell form a system consisting of a nonlinear Schrödinger-type equation for the electric field envelope and an elliptic equation for the reorientational response. The solution of the elliptic equation depends on the electric field in the whole domain, implying that the medium responds *non-locally*. In principle, the elliptic equation could be solved through the use of a Green's function, so that $\psi$ would be given by an integral of $|u|$ and the whole system could be written as a single integrodifferential equation; however, the Green's function kernel is the modified Bessel function $K_0$ [107], with a singularity at the origin, which recludes accurate and simple analytical treatment. To avoid the singular nature of the kernel, it is possible to use bounded kernels with a comparable asymptotic at infinity, such as Gaussian, sech-shaped or Lorentzian [28, 29]

Assuming a weakly nonlinear response i.e. neglecting nonlinear correction to

the walk-off $\Delta = \Delta(\theta)$ the system Eqs. (3.23-3.24) can be shown to support nematicon solutions, but general analytical solutions have not been found, even in (1+1)-D, except isolated solutions for fixed parameter values [108]. In the absence of analytic solutions, most of the studies of nematicons and other nonlinear beams in NLCs have been carried out by numerical solutions [15, 109], with some analytical modelling based on approximations such as variational methods [15]. Alternatives consist of treating nematicons as mechanical particles in a potential [110] or studying the local and global well-posedness of the evolution problem and decay of small initial conditions based on Hamiltonian mechanics together with powerful functional analysis techniques [107]. But, even then, it is necessary to reduce the system to its most basic formulation with each additional generalization presenting a difficult if not unsolvable mathematical challenge.

To illustrate this and some of the existing results we consider the single-color nematicon system studied by Panayotaros and Marchant [107].

$$i\partial_z u + \frac{1}{2}\nabla_\perp^2 u + 2\psi u, \;\; = \;\; 0 \tag{3.33}$$

$$\nu\nabla_\perp^2 \psi - 2q\psi \;\; = \;\; -2|u|^2, \tag{3.34}$$

In this limit, the system (3.33-3.36) is closely related to a Schrödinger-Poisson system, also known as Schrödinger-Newton [67] which arises as the weak-gravity limit of a system of self-gravitating and self-interacting particles in general relativity.

The inhomogeneous elliptic equation (3.34) has a unique solution $\psi = G(|u|^2)$, with $G$ a linear operator of convolution type, so that the system is equivalent to

$$iu_z - \frac{1}{2}\nabla_\perp^2 u + 4G(|u|^2) = 0. \tag{3.35}$$

Taking the Fourier transform of (3.34) we have

$$\hat{\psi}_k = \frac{\hat{f}_k}{|k|^2 + m^2}, \quad f = \frac{2}{\nu}|u|^2, \quad m^2 = \frac{2q}{\nu}, \tag{3.36}$$

and then we can write

$$\psi = \frac{2}{\nu}\int_{\mathbb{R}^2} K_0\left(\sqrt{\frac{2q}{\nu}}|x-y|\right)|u(y)|^2 d^2y, \tag{3.37}$$

where $K_0$ is the modified Bessel function [107].

The nematicon equation (3.33) with $\psi$ given by (3.37) can also be cast as

$$\frac{\partial u}{\partial z} = -i\frac{\delta \mathcal{H}}{\delta u^*}, \tag{3.38}$$

where $\mathcal{H}$ is the Hamiltonian

$$\mathcal{H} = \int_{\mathbb{R}^2} \left( \frac{1}{2} |\nabla u|^2 - 2|u|^2 G(|u|^2) \right). \tag{3.39}$$

Let $L^p(\mathbb{R})$ denote the usual Lebesgue space for $p \geq 1$, and $H^1(\mathbb{R})$ denote the usual Sobolev space. Seeking spatially localized wave solutions by studying solutions of the form $u(x,z) = e^{i\omega z}\varphi(x)$, we have the following nonlinear eigenvalue problem

$$\omega\varphi = -\frac{1}{2}\nabla^2\varphi - 4\varphi G(|\varphi|^2). \tag{3.40}$$

Panayotaros and Marchant proved for the first time in 2004 [107] that solutions of (3.40) correspond to minimizers of the Hamiltonian $\mathcal{H}$ over certain $H^1$ functions. Namely, let $\lambda > 0$ and define

$$I_\lambda = \inf \left\{ \mathcal{H}(u) : u \in H^1(\mathbb{R}^2), P(u) = \int_{\mathbb{R}^2} |u|^2 = \lambda \right\} \tag{3.41}$$

A function $\tilde{u}$ in $H^1(\mathbb{R}^2)$, satisfying $\mathcal{H}(\tilde{u}) = I_\lambda$ is referred to as a *minimizer or ground state* of $\mathcal{H}$ at power $\lambda$. Note that the power $P$ is also the $L^2$-norm. The set of minimizers of $\mathcal{H}$ at power $\lambda$ is denoted as $\mathcal{M}_\lambda$. The following results can be proved:

**Theorem 1.** *There exists $\lambda_0 > 0$ such that for all $\lambda > \lambda_0$: (i) The set $\mathcal{M}_\lambda$ is not empty. (ii) Any $\tilde{u} \in \mathcal{M}_\lambda$ is a $C^2$-solution of (3.41) and can be chosen to be real-valued. (iii) $\tilde{u} \in \mathcal{M}_\lambda$ (up to translation and global phase changes) can be taken as positive, radial and strictly decays to 0 at infinity.*

**Theorem 2.** *Let $\lambda > \lambda_0$. The set $\mathcal{M}_\lambda$ of solutions is orbitally stable.*

These properties of radial symmetry, monotonic decay to zero and stability suggest that an energy minimizer $\tilde{u}$ corresponds to an experimentally observable nematicon. Moreover, the existence of a threshold $\lambda_0$ suggests that nematicons cannot be observed for arbitrarily small powers.

Similar results of existence, regularity and symmetry have been proved for related systems: Borgna et al. [111] considered the following nematic system with saturation effect

$$i\partial_z u + \frac{1}{2}\nabla^2 u + u\sin(2\psi) = 0, \tag{3.42}$$

$$\nu\nabla^2\psi - q\sin(2\psi) + 2\cos(2\psi)|u|^2 = 0, \tag{3.43}$$

which correspond to the nematicon equations in a uniform cell without assuming a low-power approximation in Eq. (3.15), well-posedness was studied and the existence of global solutions was proved via the Banach fixed point theorem. Recently, Zhang et al. [112] studied the existence of local and global solutions of

two-colour nematicon equations given by systems of the form

$$i\partial_z u + \frac{d_1}{2}\nabla^2 u + g_1 u \sin(2\psi) = 0, \quad d_1, g_1 \in \mathbb{R}, \tag{3.44}$$

$$i\partial_z v + \frac{d_2}{2}\nabla^2 v + g_2 v \sin(2\psi) = 0, \quad d_2, g_2 \in \mathbb{R}, \tag{3.45}$$

$$\nu\nabla^2\psi - q\sin(2\psi) - 2(g_1|u|^2 + g_2|v|^2) = 0, \tag{3.46}$$

and established the global well-posedness and obtained the existence of ground-state nematicon solutions by applying variational methods.

### 3.2.1 Variational Method

One of the most widely used methods to obtain approximate solutions of NLS-type equations is the variational method. The method was applied for the first time by Anderson[113] in 1983 to approximate nonlinear pulse propagation in optical fibres modelled by the NLS equation. To illustrate the method in general, we consider the functional

$$I[u, u^*] = \int_{\Omega\times[z_0,z_f]} \mathcal{L}(u, u^*, \partial_{x_i}u, \partial_{x_i}u^*, \partial_z u, \partial_z u^*)d\mathbf{x}dz, \tag{3.47}$$

where $\mathcal{L}$ is the Lagrangian density of the system, $\Omega \subset \mathbb{R}^n$ is some open, bounded domain, $z_0$ to $z_f$ defines the trajectory of propagation and $u^*$ is the complex conjugate of $u$. Taking variations of this functional

$$\delta I = 0 \tag{3.48}$$

we obtain the following two Euler-Lagrange equations [114]

$$\frac{\partial}{\partial_z}\left(\frac{\partial\mathcal{L}}{\partial u_z^*}\right) + \sum_i \frac{\partial}{\partial x_i}\left(\frac{\partial\mathcal{L}}{\partial u_{x_i}^*}\right) - \frac{\partial\mathcal{L}}{\partial u^*} = 0, \tag{3.49}$$

$$\frac{\partial}{\partial_z}\left(\frac{\partial\mathcal{L}}{\partial u_z}\right) + \sum_i \frac{\partial}{\partial x_i}\left(\frac{\partial\mathcal{L}}{\partial u_{x_i}}\right) - \frac{\partial\mathcal{L}}{\partial u} = 0. \tag{3.50}$$

Now, considering a Lagrangian density of the form

$$\mathcal{L} = \frac{i}{2}\left(u^*\frac{\partial u}{\partial z} - u\frac{\partial u^*}{\partial z}\right) - \frac{1}{2}|\nabla u|^2 + \frac{1}{2}|u|^2\int_{-\infty}^{\infty} K(\mathbf{x}-\mathbf{s})|u(z,\mathbf{s})|^2 d\mathbf{s}, \tag{3.51}$$

where the kernel $K$ is symmetric about the argument $\mathbf{x}$. It can easily be shown that the NNLSE (1.15) in bulk media without boundary can be deduced from the Euler-Lagrange equations associated with the Lagrangian density (3.51).

The key step to finding an approximate solution of the NNLSE by the variational method is to choose a suitable *trial* function, replace it into the Lagrangian and take the average over the domain of interest. The first variation (3.48) is made to vanish for the trial function and variations are taken with respect to each of the

trial parameters in the averaged Lagrangian [3], where the averaged Lagrangian is defined by

$$L = \int_{-\infty}^{\infty} \mathcal{L} d\mathbf{x} dz. \tag{3.52}$$

There is no rigorous mathematical approach to selecting an appropriate trial function. It must be chosen either as a good match to solutions obtained from numerical methods or by the physical meaning of the particular problem without depending on too many parameters [102]. In general, trial functions are taken in the form of a basic beam profile with parameters (amplitude, width, phase) that are allowed to vary with $z$. For example, typical trial functions are perturbations of the fundamental NLS soliton (1.12) or perturbations of a Gaussian beam.

For the NNLSE equations, a trial function can be selected as a perturbation of a Gaussian beam, given by

$$u(x, y, z) = q_a(z) \exp\left(-\frac{x^2 + y^2}{2q_w^2(z)}\right) \exp\left[iq_V(z)(x^2 + y^2) + iq_\sigma(z)\right]. \tag{3.53}$$

Substituting into the averaged Lagrangian and integrating, the first variation $\delta I = 0$ becomes

$$\delta \int_0^{\infty} \mathcal{L}(q_a, q_w, q_V, q_\sigma, \dot{q_a}, \dot{q_w}, \dot{q_V}, \dot{q_\sigma}) dz = 0 \tag{3.54}$$

where $\dot{q_i} = dq_i/dz$. This variational equation corresponds to 4 Euler-Lagrange equations (4 ODEs) with generalized coordinates $q_i$ (beam parameters), that can be solved to obtain the variational approximation solutions of the Nonlinear Nonlocal Schrodinger Equation,

$$\frac{d}{dz}\left(\frac{\partial \mathcal{L}}{\partial \dot{q_i}}\right) - \frac{\partial \mathcal{L}}{\partial q_i} = 0, \quad (i = a, w, V, \sigma). \tag{3.55}$$

These equations are usually known as *modulation equations* and can trace their origin to the study of perturbative methods for nonlinear dispersive waves developed by Whitham [3].

In the absence of general exact solutions, the variational method has proved useful in analysing the propagation of optical solitary waves, providing solutions in good agreement with numerical solutions [102] and experimental results [115, 116], and allowing analytical modelling of radiative losses [117]. The solutions derived from variational methods can be simple enough to determine the behaviour of propagation beams in various scenarios [15]. Nevertheless, one of its drawbacks is their potential sensibility to the choice of a good trial function, being necessary to compare several different trial functions to determine their absolute and relative accuracies [118]. This pose also a challenge as calculating the integrals in the averaged Lagrangian cannot be done analytically for some trial functions. Finally, we should remark that the variational method is an approximate method that requires a Lagrangian formulation for the governing equations, and including

realistic experimental factors could render the variational problem analytically unattainable.

### 3.2.2 Modulation Theory for the Nematicon Equations

In the case of nematicon propagation through a sample with nonuniform background orientation either $y-$ or $z-$ dependent, it is possible to derive mechanical equations for the trajectory applying the variational method described in the previous sections only when the all-optical reorientation $\psi$ is small compared to the background angle $\theta_b$ and the nonlinear contribution to the walk-off is neglected i.e. $\Delta(\Theta) \approx \Delta(\theta_b)$. For simplicity, we can consider the Lagrangian formulation of Eqs. (3.23) and (3.24), but the method can be applied without losing generality to the system Eqs. (3.15) and (3.16). The corresponding Lagrangian is

$$\begin{aligned}\mathcal{L} = i(u^* u_z - u u_z^*) + i\gamma\Delta(\theta_b)(u^* u_y - u u_y^*) \\ -|\nabla u|^2 + 4\frac{\sin 2\theta_b}{\sin 2\theta_0}\psi|u|^2 - \nu|\nabla\psi|^2. \end{aligned} \tag{3.56}$$

We then take trial functions for the profiles of the electric field and the director distribution of the form

$$u = \{a(z)\,\mathrm{sech}(\rho_e) + ig(z)\}e^{i\sigma(z)+iV(z)(y-\xi(z))}, \quad \psi = \alpha(z)\,\mathrm{sech}^2(\rho_d), \tag{3.57}$$

where

$$\rho_e = \frac{\sqrt{x^2+(y-\xi(z))^2}}{w(z)}, \qquad \rho_d = \frac{\sqrt{x^2+(y-\xi(z))^2}}{\beta(z)}. \tag{3.58}$$

Here, $a$ and $w$ are the amplitude and waist of the nematicon, $\alpha$ and $\beta$ are the amplitude of the director distribution, $\xi$ is the nematicon position, $V$ is the velocity and $\sigma$ is the nematicon phase. The first term in the trial function for the electric field $u$ in (3.57) represents a perturbation of the profile of the exact soliton solution of the NLS equation. The second term represents diffractive radiation that accumulates as the nematicon evolves [15]. As the nematicon evolves due to changes in the medium, its amplitude $a$ and width $w$ oscillate while it refracts, so its velocity $V$ and position $\xi$ evolve, as well. The main effect of the oscillations is to cause the solitary wave to shed radiation, enabling the nematicon to reach a steady state. This radiation has momentum and in turn, affects the nematicon trajectory. If we are interested only in the nematicon trajectory, we can assume the amplitude $a, \alpha$ and width $w, \beta$ constant and take only the velocity $V$ and position $\xi$ to depend on $z$. Substituting the nematicon trial functions (3.57) into the Lagrangian (3.56), averaging results in the averaged Lagrangian by integrating over $x$ and $y$ from $-\infty$ to $\infty$.[1], leaving an averaged Lagrangian $\mathcal{L}$ which is a function of $z$. Finally, taking variations with respect to the velocity $V$ and position $\xi$ results in mechanical equations for the beam trajectory [3].

[1]Note that a solitary wave has an infinite period.

The averaged Lagrangian is found as [30, 110]

$$\mathcal{L} = -2S_2(\sigma' - V\xi')a^2w^2 - S_{22}a^2 - S_2[V^2 + 2V\gamma\Delta(\theta_b)]a^2w^2 \\ +4\frac{\sin(2\theta_b)}{\sin(2\theta_0)}\alpha a^2w^2S_m - 4\nu S_{42}\alpha^2, \tag{3.59}$$

where primes denote differentiation with respect to $z$ and the $S_i$, $S_{ij}$ are integrals arising at the moment of averaging the Lagrangian in (3.56), explicitly they are given by

$$S_2 = \int_0^\infty sf_e^2(s)ds, \quad S_{22} = \int_0^\infty sf_e'^2(s)ds, \quad S_m = \int_0^\infty f_d(ws/\beta)f_e^2ds, \\ S_{42} = \frac{1}{4}\int_0^\infty s\left[\frac{d}{ds}f_d(s)\right]^2 ds. \tag{3.60}$$

Taking variations of (3.58) with respect to $V$ and $\xi$ we obtain the mechanical equations mentioned before

$$\frac{dV}{dz} = 0, \tag{3.61}$$

$$\frac{d\xi}{dz} = V + \gamma\Delta(\theta_b(z)). \tag{3.62}$$

These modulation equations are momentum equations for the nematicon trajectory, they offer a condensed form to describe nematicon evolution, as an alternative to numerical methods, which require significant computational powers. However, the difference with experimental results can grow significant with the propagation distance and beam power which limits the predictive power of modulation theory in more general settings where (i) the optical contribution $\psi$ is significant to the walk-off $\Delta$; (ii) the optical reorientation $\psi$ is not small; (iii) scattering losses are not neglected and more.

# Chapter 4

# Optical diode effect and direction-dependent nematicons

We introduce the concept of a guided wave all-optical diode based on nematicons and corresponding waveguides in a planar sample encompassing a nonsymmetric modulated orientation (alignment) of the optical axis, directly linked to a nonuniform nonlinear (reorientational) strength, with varying transverse spatial velocity (walk-off). Such geometry provides all-optical self-focussing in a nonspecular arrangement, in other words, solitary waves launched by identical input beams from opposite ends, experience different evolution trajectories. Moreover, for a two-port device corresponding to the FP nematicon waveguide connecting the input port to the output location upon propagation, a backward-launched signal (BP nematicon waveguide) would not be transmitted through the former. Using realistic NLC physical parameters and sample features, we analyze the role of background orientation and nonlocality, power and losses, demonstrating the feasibility of solitary-wave-based nonspecular signal transmission featuring direction-dependent beam and signal routing. The results are presented in the published article Opt. Lett. 47(11), 2782-2785 (2022) [119]. (See Appendix A)

## 4.1 Geometry

We consider nematicons excited in a planar cell of fixed (uniform) thickness, with upper and lower interfaces treated to ensure planar anchoring of the NLC molecules and a linearly varying distribution of the optical axis. Figure 4.1 depicts the main molecular director configurations considered throughout this work.

The polarization of the electric field $\vec{E} = E_y\hat{y}$ is taken to be the $y$ direction. The NLC molecular director rotates in the $(y, z)$ plane, with its orientation $\theta$ measured from $\mathbf{k} \parallel \hat{z}$. The light beam is input at $y = 0$ at $z = 0$ at which point the director forms an angle $\theta_0$. The background orientation varies with $z$ down the cell with $\theta_0(z) = \theta_0(0) + \theta_b(y, z)$. Finally, the beam causes an additional all-optical reorientation denoted by $\psi$. Hence, the total angle of the optic axis with the $z$ direction is $\Theta = \theta_0(0) + \theta_b(y, z) + \psi(x, y, z)$.

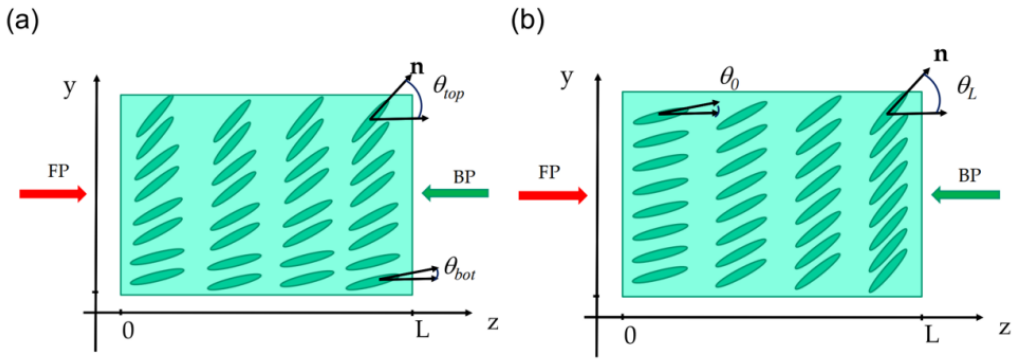


Figure 4.1: Sketch of planar NLC cells with linearly modulated orientation of the optical axis $\vec{n}$(green ellipses) along one of the spatial coordinates. The red arrow indicates the input of the FP beam, and the green arrow refers to the BP beam, with FP and BP beams linearly polarized $e$-waves. (a)Transverse modulation across $y$; $\theta_{bot}$ is the orientation in $y = y_{bot}$, $\theta_{top}$ is the orientation in $y = y_{top}$, with $d = y_{top} - y_{bot}$ the width of the cell. (b) Longitudinal modulation of the background orientation; $\theta_0$ is the orientation in $z = 0$, $\theta_L$ is the orientation in $z = L$.

When an electromagnetic wavepacket of wavevector $\vec{k}$ and electric field $\vec{E}$ polarized in the principal plane propagates through the NLC sample, the reaction between the polarization field $\vec{P} = \epsilon\chi\vec{E}$ and $\vec{E}$ results in a rotational torque $\vec{\Gamma} = \vec{P} \times \vec{E}$ which, acting on the molecular dipoles, increases the orientation angle by the power-dependent amount $\psi$, producing a Kerr-like self-focusing with $n_e(\Theta) > n_e(\theta_b)$, $\Theta = \theta_b + \psi$ and $\psi \ll \theta_b$ in the usual weak nonlinear regime. The equilibrium distribution of the director $\vec{n}$ is determined by the counteracting role of the electrical torque $\vec{\Gamma}$ and the elastic forces acting in the liquid state. When $\vec{n}$ is perpendicular to the electric field, reorientation can only occur above the power threshold given by the Freedericksz transition [54] (c.f Section 2.2).

Nematicons arise from the stable balance between linear diffraction and self-focusing produced by the nonlinear $e$-index increase (4.1) in the planar geometries of interest and in the presence of a nonlocal and saturable optical self-focusing response [100].

$$n_e = n_e[\Theta(x, y, z)] \approx n_e[\theta_b(y, z)] + \psi \frac{dn_e(\theta_b)}{d\theta_b}. \tag{4.1}$$

The light-induced reorientation gives rise to graded-index channel waveguides featuring a large numerical aperture and able to confine extraordinarily polarized signals, with the energy flux $\vec{S}$ at an angle $\delta$ with respect to $\vec{k}$ (c.f. Chapter 2).

Owing to the birefringence of NLCs, the propagation of extraordinary waves is governed by an angle-dependent refractive index and has phase velocity $v =$

$c/n_e(\Theta)$, with the extraordinary refractive index $n_e$ given by

$$n_e(\Theta) = \frac{n_\parallel n_\perp}{\sqrt{(n_\perp^2 - n_\parallel^2)\sin^2\Theta + n_\parallel^2}}, \tag{4.2}$$

where $n_\parallel$ and $n_\perp$ are the extraordinary and ordinary refractive index eigenvalues respectively, and the spatial group velocity (walk-off) is given by

$$\delta(\Theta) = \arctan\Delta(\Theta) = \arctan\left[\frac{\Delta\epsilon\sin\Theta\cos\Theta}{n_\perp^2 + \Delta\epsilon\cos^2\Theta}\right]. \tag{4.3}$$

Note that the light-induced response $\psi(x, y, z)$ depends on the beam power and size as well on the alignment distribution $\theta_b(y, z)$ and the NLC parameters, including the nonlocality range related to the elasticity.

## 4.2 Interaction of nematicons with cell boundaries

In early studies on the formation and steering of nematicons, the NLC cell was considered to be infinite and the effects of the cell walls were assumed negligible to the propagation dynamics of the nematicon. This is a good approximation for nematicons propagating in the centre of the cell with a typical width being 24 times the width of the input beam [100]. However, the cell boundaries can play a major role, particularly when the soliton comes close to one of them [120, 121]. It can be demonstrated that the anchoring gives rise to an effective repulsive force which repels an approaching nematicon. Owing to nonlinearity and nonlocality, such repulsion depends on the beam power and entails power-dependent interaction with the boundaries that were experimentally studied by Alberucci et al. [121], launching intense beams with initial transverse velocity in the principal plane in order to enhance the interaction with the cell wall (c.f. Figure 4.2).

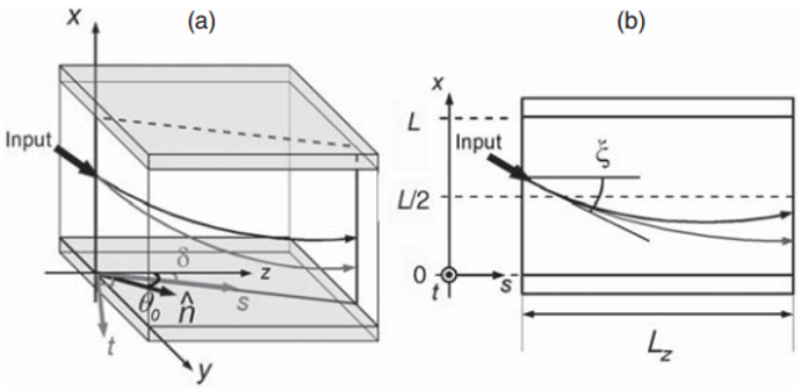


Figure 4.2: (a)3D Sketch and (b) side view (plane $xz$ of a planar cell depicting repulsive cell boundaries. Nematicons are launched with an initial momentum with respect to $x$ and the repulsive force increases with power (darker trajectory). Image reproduced from [120]

Throughout this work, we consider nematic cells of length $L$, width $d$ and thickness $h$ along $z$,$y$ and $x$, respectively, with $(x, y, z)$ a standard system of mutually orthogonal axes. The cells are taken with $h \ll d, L$, but $h$ is much larger than the nonlinear wavepacket's spot size ($\sim 4\mu$m). This assures that the resulting nematicons will travel through the sample with minimal interactions with the boundaries.

## 4.3 Linear Longitudinal Modulation

First, we consider a planar cell where the background orientation $\theta_b$ (at rest) has a linear dependence across the length $L$ of the NLC sample and is uniform across the width (c.f. Figure 4.1 (b)),

$$\theta_b = \theta_b(z) = \theta_0 + (\theta_L - \theta_0)\frac{z}{L}, \tag{4.4}$$

with $\theta_0 = \theta_b(z = 0)$ and $\theta_L = \theta_b(z = L)$. This choice allows us to illustrate the basic phenomena in the simplest limit, leaving other functional dependencies to be considered in later sections.

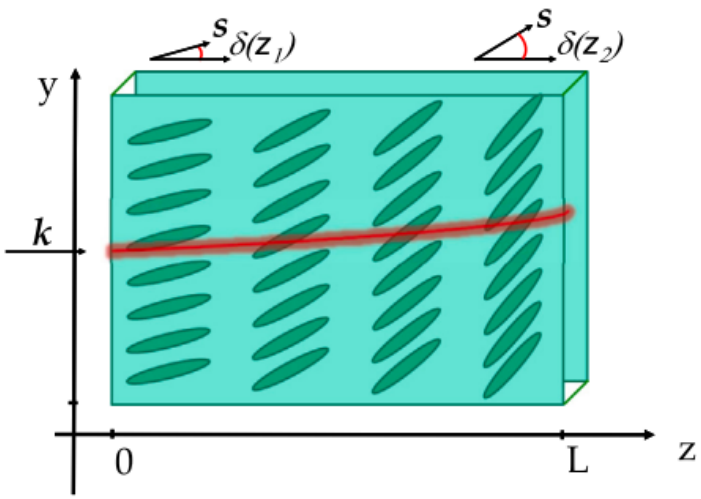


Figure 4.3: Sketch of a planar NLC sample with a modulated orientation $\theta(z)$ along $z$, displaying the trajectory (red) of an extraordinary wave soliton with input wave vector $\vec{k}$ and walk-off $\delta = \delta(z)$. Group velocity $\delta$ and Poynting vector $\vec{S}$ are indicated in two locations along the cell. Reproduced with permission from Wave Motion, Volume 130,2024,103379.[122]

The model describing nonlinear light beam propagation and solitary wave generation in NLCs subject to pure reorientation is known [61] and was outlined in Chapter 3. We will focus on the principal plane $(y, z)$ where the extraordinary wave eigensolutions propagate and reorientation takes place since the orthogonal coordinate $x$ does not affect the dynamics in the regime of self-confinement.

In the paraxial, slowly varying envelope approximation, we adopt a reduced (1+1)-D NLC model that can be written in a non-dimensional form (in the absence of scattering losses) as [61]

$$i\frac{\partial u}{\partial Z} + i\gamma\Delta(\theta_b(Z)+\psi)\frac{\partial u}{\partial Y} + \frac{1}{2}\frac{\partial^2 u}{\partial Y^2} + 2\frac{\sin(2\theta_b(Z))}{\sin(2\theta_b(0))}\psi u = 0, \tag{4.5}$$

$$\nu\frac{\partial^2 \psi}{\partial Y^2} + 2\frac{\sin(2\theta_b(Z))}{\sin(2\theta_b(0))}|u|^2 = 0. \tag{4.6}$$

$(Y, Z) \in \left[-\frac{D}{2}, \frac{D}{2}\right] \times [0, L]$ are the scaled principal plane coordinates and $u(Y, Z)$ is the beam electric field, with

$$y = \frac{\lambda}{\pi\sqrt{\Delta\epsilon \sin 2\theta_0}}Y, \quad z = \frac{2n_e\lambda}{\pi\Delta\epsilon \sin 2\theta_0}Z, \quad E = \sqrt{\frac{4P_b}{\pi\epsilon_0 c n_e W_b^2}}u. \tag{4.7}$$

Here, $c$ is the speed of light in vacuum and $\lambda$ is the wavelength, while the walk-off

coefficient $\gamma$ and elasticity parameter $\nu$ are

$$\gamma = \frac{2n_e}{\sqrt{\Delta\epsilon \sin 2\theta_0}} \quad \text{and} \quad \nu = \frac{2\pi^3 n_e c K W_b^2}{\lambda^2 P_b}. \tag{4.8}$$

The dimensionless scaling above is based on a Gaussian reference beam of power $P_b$ and half-width $W_b$, with typical experimental [15] values $P_b = 2.7$mW and $W_b = 3.5\mu$m, respectively.

The initial electric field envelope for the light beam $u$ is set to a normalized Gaussian beam profile

$$u(Y, Z = 0) = A_b \exp\left(Y^2/W_b^2\right), \tag{4.9}$$

where $A_b$ and $W_b$ are the maximum electric field amplitudes and width of the beam. Conversely, the all-optical reorientational angle $\psi$ is uniformly set equal to zero

$$\psi(Y, Z = 0) = 0 \tag{4.10}$$

The BP nematicon equations can be directly obtained from equations (4.5) and (4.6) after changing $Z$ to $L - Z$ (equivalent to reversing the wavevector $\vec{k}$) and adjusting the initial angle to $\theta_b(L)$, namely

$$-i\frac{\partial v}{\partial Z} + i\gamma\Delta(\theta_b(L - Z) + \tilde{\psi})\frac{\partial v}{\partial Y} + \frac{1}{2}\frac{\partial^2 v}{\partial Y^2} + 2\frac{\sin(2\theta_b(L - Z))}{\sin(2\theta_b(L))}\tilde{\psi}v = 0, \tag{4.11}$$

$$\nu\frac{\partial^2 \tilde{\psi}}{\partial Y^2} + 2\frac{\sin(2\theta_b(L - Z))}{\sin(2\theta_b(L))}|v|^2 = 0. \tag{4.12}$$

$(Y, Z)$ are the scaled principal plane coordinates and $v(Y, Z)$ is the BP beam electric field envelope, with

$$y = \frac{\lambda}{\pi\sqrt{\Delta\epsilon \sin 2\theta_L}}Y, \quad z = \frac{2n_e\lambda}{\pi\Delta\epsilon \sin 2\theta_L}Z, \quad E = \sqrt{\frac{4P_b}{\pi\epsilon_0 c n_e W_b^2}}u. \tag{4.13}$$

The initial conditions for the BP beam are set to

$$v(Y, Z = L) = A_b \exp\left((Y - y_{FP}(L))^2/W_b^2\right), \tag{4.14}$$

$$\tilde{\psi}(Y, Z = L) = \psi(Y, Z = L) \tag{4.15}$$

where $y_{FP}(L)$ is the transverse position at $Z = L$ of the FP beam $u$ and $\psi(Y, Z = L)$ is the all-optical molecular reorientation generated by the FP beam at $z = L$.

The choice of a reduced (1+1)-D model was made for the sake of computational savings. Typical computer runs to simulate the (1+1)-D system took between 20 and 40 minutes for propagation lengths of $1000\mu m$ in a single In-

tel Xeon E5-2680 at 2.5 GHz, while typical computations times for the (2+1)-D system were close to 10000 minutes for the same propagation distance. The reduced (1+1)-D accounts for all the features of the original nematicon system [15], that is, nonlocality, self-confinement and dissipative response, but the dynamic is shifted to lower beam powers and it has been shown [15] that nematicon formation requires an effective two-dimensional power smaller than the actual power in a general (2+1)-D system. Thus, we should remark that the reduced (1+1)-D is a useful approximation to establish proof-of-concept, but it may miss or misestimate important power effects.

In the numerical experiments, we adopted material parameters characteristic of the standard NLC mixture E7, with $n_{\parallel} = 1.7$, $n_{\perp} = 1.5$ and $K = 1.2 \times 10^{-11} N$, with nonlocality $\nu = 350$ (unless stated otherwise in the results). A NLC planar cell was chosen with dimension $30\mu m \times 400\mu m \times 1mm$ in $(h, d, L)$. We launch identical input beams with $\vec{k} = \vec{z}$ for forward propagation and $\vec{k} = -\vec{z}$ for backward propagation, using values of beam power, width and wavelength to ensure formation and propagation of nematicons. FP and BP input beams of wavelengths $1064nm$ were extraordinary waves with Gaussian profiles launched at $(y, z)_{FP} = (0, 0)$ for FP inputs and $(y, z)_{BP} = (y_{FP}(L), L)$ for BP beams, with $y_{FP}(L)$ the transverse output position of the FP wave packet.

To model the system numerically, the electric field equation (4.5), was solved using a pseudo-spectral method with Fast Fourier transform (FFT) used to calculate the spatial derivatives in $Y$ and propagated in $Z$ using the fourth-order Runge-Kutta (RK4) scheme. The director equation (4.6), was solved using second-order centred finite differences.

### 4.3.1 Numerical Methods

The numerical scheme introduced here is developed from the split-step spectral method derived by Fornberg and Whitham [93] to solve numerically the NLS equation. The main difference from the scheme created by Fornberg and Whitham is that the propagation of the numerical solution in the $z$ direction is performed on the Fourier transform of the equation using the RK4 method, rather than in physical space using a second-order scheme. Additionally, a damping layer can be included to absorb outgoing radiation at the boundaries of the computational domain [94]. Adding a damping term to the electric field equation (4.5) yields

$$i\frac{\partial u}{\partial z} + i\gamma\Delta(\theta_b(z) + \psi)\frac{\partial u}{\partial y} + \frac{1}{2}\frac{\partial^2 u}{\partial y^2} + 2\frac{\sin(2\theta_b(z))}{\sin(2\theta_0(0))}\psi u + i\epsilon(y)u = 0, \tag{4.16}$$

where the absorption function is given by

$$\epsilon(y) = \gamma_0[\mathrm{sech}^2(\zeta(y - d/2)) + \mathrm{sech}^2(\zeta(y + d/2))]. \tag{4.17}$$

Here $\gamma_0$ and $1/\zeta$ are the strength and width of the damping layer, respectively. The inclusion of a damping layer leaves the solution undisturbed by radiation that cannot escape the system without an absorbing boundary.

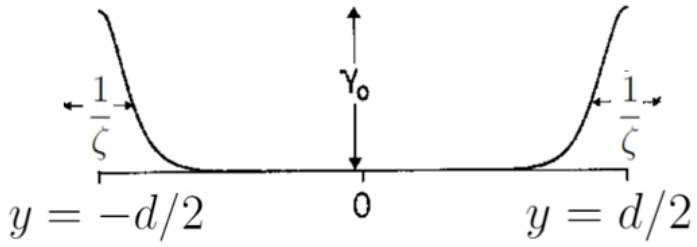


Figure 4.4: The absorption function $\epsilon(y)$ introduces losses in the neighborhood of the boundaries at $y \pm d/2$. The parameters $\gamma_0$ and $\zeta$ are chosen such that the scattering from the absorption walls is small. Figure adapted from [94].

We can rewrite Equation (4.16) as

$$\underbrace{i\partial_z u + \frac{1}{2}\partial_{yy} u}_{\text{Linear Part}} + \underbrace{i\gamma\Delta(\theta_b + \psi)\partial_y u + i\epsilon(y)u + 2\frac{\sin(2\theta_b)}{\sin(2\theta_0)}\psi u}_{=NON} = 0. \tag{4.18}$$

Taking the Fourier transform of (4.18) yields

$$\partial_z \hat{u} - \frac{i}{2}s^2\hat{u} + \mathcal{F}(NON(u,\psi)) = 0, \tag{4.19}$$

where $s \in \mathbb{R}$ represents the Fourier transform variable or frequency. Here, the adopted definition of the continuous Fourier transform is

$$\mathcal{F}(u(y,z);s) = \hat{u}(s,z) = \int_{-\infty}^{\infty} u(y,z)e^{2\pi i y s}dy. \tag{4.20}$$

Equation (4.19) is an ODE in the time-like variable $z$. The spatial domain $\left[-\frac{d}{2}, \frac{d}{2}\right]$ is discretized into $N$ equidistant samples such that $N$ satisfies $N = 2^j$ for some $j \in \mathbb{N}$. Such a choice is necessary to apply the fast Fourier transform method (FFT). Then a discretization of the variable $y$ is

$$y_n = n\Delta y; \quad n \in \left\{-\frac{N}{2}+1, \ldots, \frac{N}{2}\right\},$$

where the sampling rate is $\Delta y = d/N$. To prevent aliasing the frequency domain is restricted to the values

$$s_k = k\Delta s; \quad k \in \left\{-\frac{N}{2}+1, \ldots, \frac{N}{2}\right\},$$

where the frequency resolution satisfies $\Delta s = 2\pi/N = 2\pi\Delta y/d$. Therefore, equa-

tion (4.19) takes the following discretized form

$$\frac{d}{dz}\hat{u}_k(z) + \frac{i}{2}s_k^2\hat{u}_k(z) + i\mathcal{F}\{NON(u_k(z),\psi_k(z));s\} = 0. \tag{4.21}$$

To suppress instabilities at high frequencies, an integrating factor method is applied to solve this ODE [123]

$$\frac{d}{dz}\left\{e^{is_k^2 z/2}\hat{u}_k(z)\right\} = -i\mathcal{F}\{NON(u_k(z),\psi_k(z));s\}e^{is_k^2 z/2}. \tag{4.22}$$

The director angle $\psi_k(z)$ is determined from the director equation (4.6) with $\psi = 0$ at the boundaries $y = \pm d/2$, i.e. a two-point boundary problem in $y$

$$\begin{cases} \dfrac{d^2\psi}{dy^2} = -\dfrac{2}{\nu}\dfrac{\sin(2\theta_b)}{\sin(2\theta_0)}|u|^2, \\ \psi(\pm d/2) = 0. \end{cases} \tag{4.23}$$

This system can be solved using standard second-order finite difference to obtain

$$\psi_{i+1} - 2\psi_i + \psi_{i-1} = (\Delta y)^2 f(\psi_i), \tag{4.24}$$

where $f$ includes all the nonlinear terms. This can be written in matrix form

$$A\psi = b, \quad A = \begin{pmatrix} 2 & -1 & 0 & \cdots\cdots & 0 \\ -1 & 2 & -1 & \cdots\cdots & 0 \\ & \ddots & \ddots & & \\ \cdots\cdots & \cdots\cdots & \cdots\cdots & -1 & 2 \end{pmatrix}. \tag{4.25}$$

Given an initial guess $\psi_0$ for $\psi$, we iterate

$$A\psi_{i+1} = b(\psi_i), \tag{4.26}$$

until $\psi_i$ converges.

We can now substitute this solution into the electric field equation (4.22) and solve the ODE. Fornberg and Whitham [93] used a leapfrog $z$ stepping scheme where $\hat{u}_z$ was approximated by $\hat{u}_z \approx \hat{u}(y, z+\Delta z) - \hat{u}(y, z-\Delta z)$. However, in Fourier space, the calculation of $\hat{u}_z$ is more accurately performed using the RK4 method.

Equation (4.22) can be rewritten in the form

$$\frac{d\phi_k}{dz} = G(\phi_k, z), \tag{4.27}$$

where $\phi_k(z) = \hat{u}_k(z)e^{is_k^2 z}$ and $G(\phi_k, z)$ comprises the elements on the right-hand side of (4.19). Now, with these definitions, the RK4 method takes $\phi_k^n$ at the

current step $n$, and computes $\phi_k^{n+1}$ at the next step $z_{n+1} = z_n + \Delta z$ as follows

$$\phi_k^{n+1} = \phi_k^n + \frac{1}{6}(k_1 + 2k_2 + 2k_3 + k_4), \quad z_{n+1} = z_n + \Delta z, \tag{4.28}$$

where

$$\begin{aligned} k_1 &= G(z_n, \phi_k^{n+1}), & (4.29)\\ k_2 &= G\left(z_n + \frac{\Delta z}{2}, \phi_k^n + \frac{\Delta z}{2}k_1\right), & (4.30)\\ k_3 &= G\left(z_n + \frac{\Delta z}{2}, \phi_k^n + \frac{\Delta z}{2}k_2\right), & (4.31)\\ k_4 &= G\left(z_n + \Delta z, \phi_k^n + \Delta z k_3\right). & (4.32) \end{aligned}$$

Finally, $u^{n+1}$ is extracted from $\phi_k^{n+1}$ by multiplying by the integrating factor and then inverting $\hat{u}$ using the inverse FFT algorithm to return to physical space. This process is iterated until the final $z$ value is reached.

To summarize, we consider that the propagation length $[0, L]$ (time-like domain) is discretized into $N_z$ points

$$z_n = n\Delta z; \quad n \in \{1, \ldots, N_z\} \tag{4.33}$$

where $\Delta z = L/N_z$.

1. For simplicity, we consider an input Gaussian beam launched from the midplane of the cell $y_0 = 0$ (in principle, the beam can be launched from any position) as the initial condition at $z = 0$

   $$u_0(y) = u(0, y) = A_b e^{-y^2/W_b^2}, \tag{4.34}$$

   where $A_b$ and $W_b$ are the nondimensional amplitude and width of the beam, respectively. On the other hand, the all-optical reorientational angle $\psi$ is uniformly set equal to zero $\psi_0(y) = 0$. The initial electric field condition $u_0(y)$ is used to determine the distribution of the reorientation angle $\psi_1(y)$ at $z = \Delta z$ from the discretized director equation (4.24).

2. $\psi_1(y)$ is used in the discretized electric field equation (4.22) and the solution is propagated one time step $\Delta z$ to obtain $u_1(y) = u(\Delta z, y)$.

3. The process is iterated until we obtain $u_{N_z}(y) = u(L, y)$, the solution at $z = L$.

4. At $z = L$, the position at the centre of the beam is obtained by

   $$y_{FP}(L) = y^* = k^* \Delta y, \tag{4.35}$$

   where $k^* = \arg\max\{u(L, y_k) : k \in -N/2 + 1, \ldots, N\}$.

The initial condition for the BP beam is then

$$v_0(y) = A_b e^{(y-y_{FP}(L))^2/W_b^2} \tag{4.36}$$

5. Steps 1, 2 and 3 are repeated to solve the BP system (4.11) and (4.12) after changing $z$ by $L - z$ in the electric field equation.

| Typical Numerical Parameter | | |
|---|---|---|
| Symbol | Parameter | Value |
| $N$ | Number of spatial modes | 2048 |
| $D$ | Nondimensional spatial interval | 1250 |
| $\Delta y$ | Spatial sampling rate | 0.6 |
| $N_z$ | Number of time-like steps | 189000 |
| $L$ | Nondimensional propagation interval | 948 |
| $\Delta z$ | Time-like step | 0.005 |
| $A_b$ | Nondimensional amplitude | $0.05 \rightarrow 0.12$ |
| $W_b$ | Nondimensional width | $5 \rightarrow 12$ |
| $\gamma_0$ | Strength of the damping layer | 40 |
| $1/\eta$ | Width of the damping layer | 1 |
| $\nu$ | Nonlocality parameter | 250 |
| $\alpha$ | Nondimensional loss coefficient | 0.001 |

Table 4.1: Typical numerical parameters for the linear longitudinal modulation problem.

## 4.4 Results Longitudinal Modulation

Figure 4.5 compares the trajectories and amplitudes of FP and BP nematicons launched by identical input Gaussian beams with $\vec{k}_{FP} = \vec{z}$ for the FP beam and $\vec{k}_{BP} = -\vec{z}$ for the backwards propagation, using beam parameters of $P_b = 1.7$ $mW$, $W_b = 3.5$ $\mu m$ and $\lambda = 1064$ $nm$. The $z-$modulated director variation is defined by $\theta_0 = 45°$ and $\theta_L = 80°$ and the inset shows the corresponding extraordinary refractive index $n_e$ and beam walk-off $\delta$. The injected wave packet experiences self-focusing (since the extraordinary refractive index increases) and self-routing (through walk-off change) at varying rates as it initially travels along regions oriented at either $\theta_0$ (FP) or $\theta_L$ (BP), respectively.

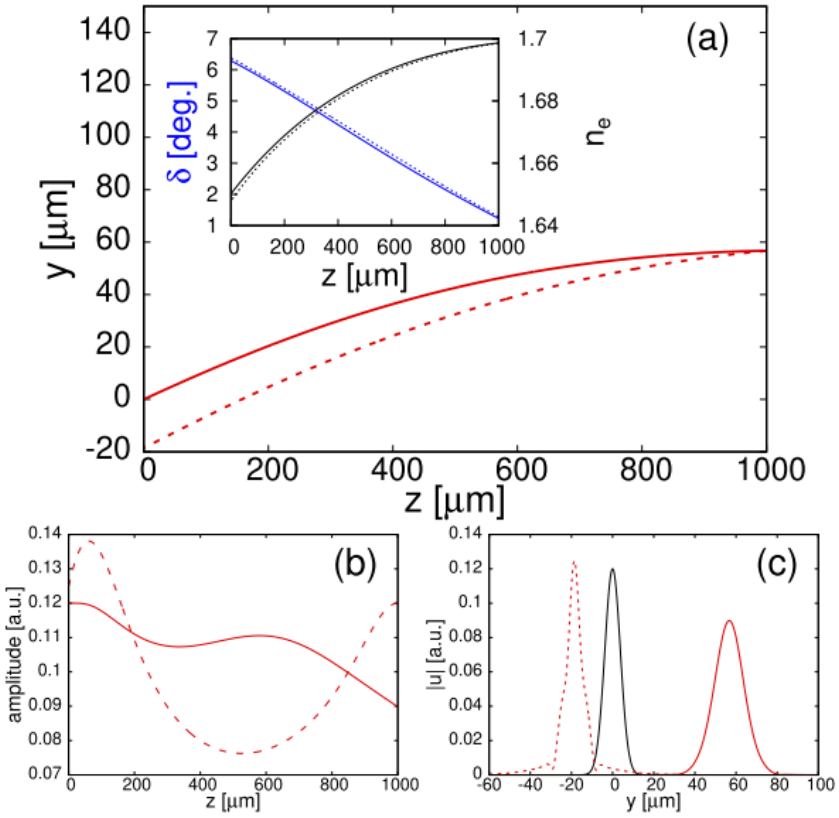


Figure 4.5: Diode-like response for 1.7 mW input beams and $\theta_0 = 45°$,$\theta_L = 80°$. (a) FP (solid line) and BP (dashed line) beam trajectories in $(y, z)$. Inset: walk-off angle $\delta$ (blue lines) and extraordinary refractive index $n_e$ (black lines). (b) Dimensionless amplitudes $|u|_{\max}$. (c) Transverse profiles of input beam (black solid lines). Reproduced with permission from Opt. Lett. 47(11), 2782-2785 (2022) [119].

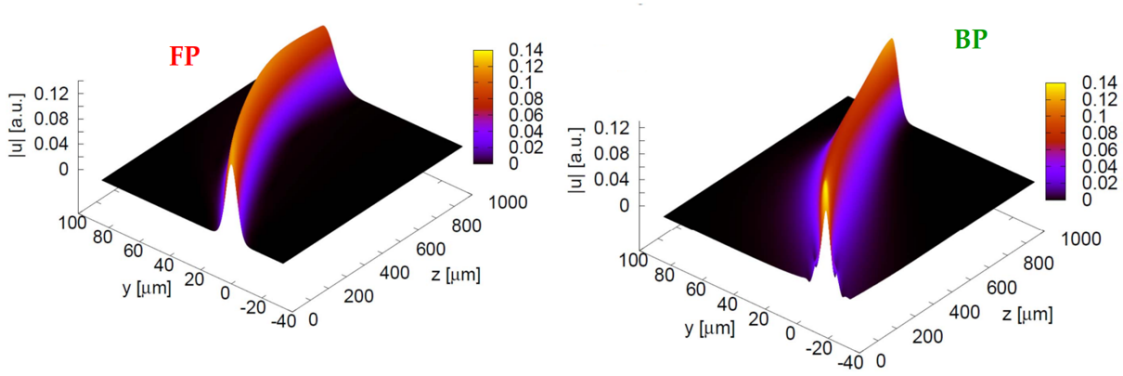


Figure 4.6: Distinct FP and BP nematicon evolution profiles (normalized field amplitude $u$ in arbitrary units) for 1.7 $mW$ input beams and $\theta_0 = 45°$, $\theta_L = 80°$.

Figure 4.5(c) displays well-separated FP and BP nematicons profiles compared with the Gaussian input, with a transverse displacement $\approx 20\mu m$ at $z = 0$ consistent with a diode-like response albeit some small amount of energy reaches the FP input port. Figure 4.6 shows a 3D plot of the FP and BP nematicon trajectory evolution. Unequal shelves are formed due to radiation shedding around the self-trapped beams as consequence of amplitude and phase adjustments in nonspecular dielectric environments, as anticipated. Figures 4.7 and 4.8 present similar results for $\theta_0 = 25°$ and linear modulation up to $\theta_L = 65°$. The BP-FP transverse beam separation can exceed $40\mu m$ displaying isolator-like behaviour with no BP energy reaching the FP input port. This is expected, as the background reorientation interval crosses the mid-value 45° where the maximum reorientational response is anticipated (maximum of the walk-off).

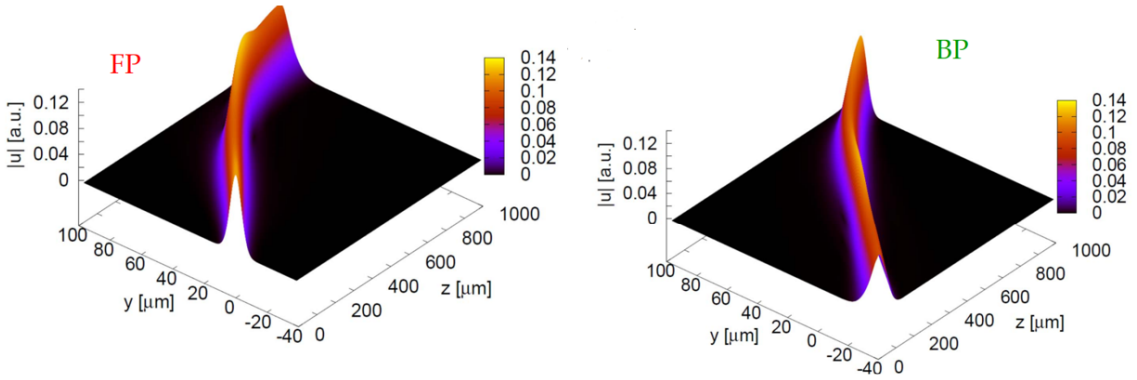


Figure 4.7: Distinct FP and BP nematicon evolution profiles (normalized field amplitude $u$ in arbitrary units) for 1.7 $mW$ input beams and $\theta_0 = 25°$, $\theta_L = 65°$.

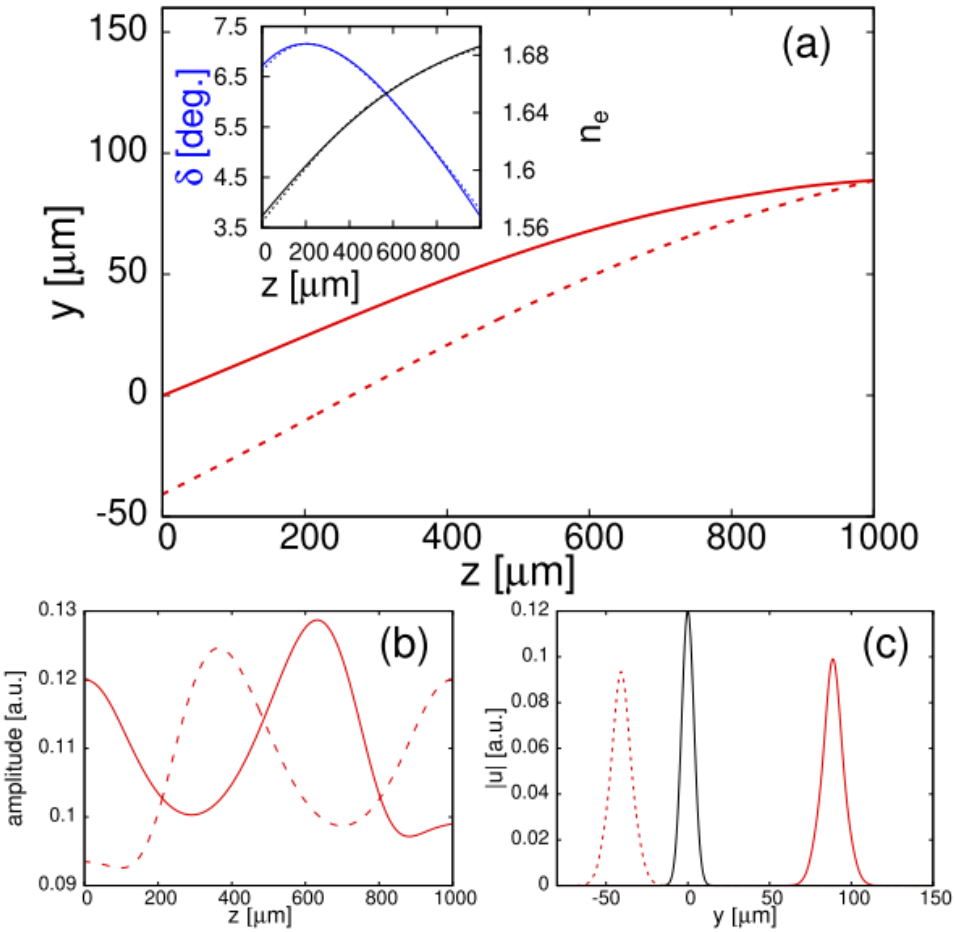


Figure 4.8: Isolator-like response for 1.7 mW input beams and $\theta_0 = 25°$,$\theta_L = 65°$. (a) FP (solid line) and BP (dashed line) beam trajectories in $(y, z)$. Inset: walk-off angle $\delta$ (blue lines) and extraordinary refractive index $n_e$ (black lines). (b) Dimensionless amplitudes. (c) Transverse profiles of input beam (black solid lines). Reproduced with permission from Opt. Lett. 47(11), 2782-2785 (2022) [119].

Since the amount of radiation and momentum shed by the FP and BP beams depends on the pointwise optical parameters of the nematic [30, 100] and the strength of the nonlinear effects had been observed to be different and power-dependent between small and large values of $\theta_0$ [15]. Then, the output nematicons are expected to exhibit distinct evolutions in a nonuniform sample.

From Figures 4.5(c) and 4.8 (c), we observed that although amplitude evolution is not completely symmetric there is an amplitude reduction due to radiation. This radiation takes away momentum and the beam angle decreases to conserve the total momentum.

### 4.4.1 Director response

Figures 4.6 and 4.7 show that the electric field has the form of a localized beam, yet due to the high nonlocality of the medium the all-optical director response $\psi$ is, as expected, not localized and has a triangular shape (c.f. Figure 4.9).

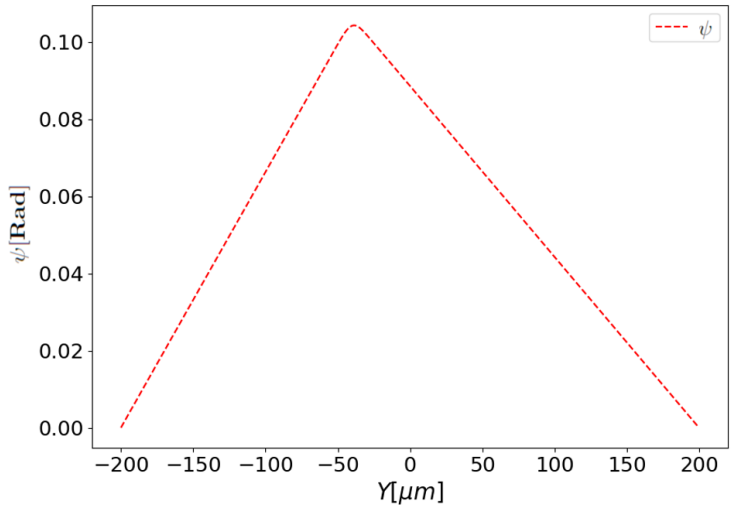


Figure 4.9: Typical all-optical director response $\psi$ at $z = L$ for nematic samples cells $z$-modulated with $\theta_0 = 10°$, $\theta_L = 45°$

The form of this solution can be explained directly from the director equation (4.6) since far away from the optical field of the beam $u = 0$ the equation becomes

$$\frac{\partial^2 \psi}{\partial y^2} = 0, \tag{4.37}$$

which has a linear solution consistent with the linear regions in Figure 4.9.

We should note that this solution is qualitatively different to the one obtained if a static pre-tilt electric field is applied to the sample to overcome the Freedericksz transition (See Section 2.2). This can be deduced from the pre-tilted director equation (2.8) far away from the beam, in this limit the director equation is

$$\frac{\partial^2 \psi}{\partial y^2} - \frac{2q}{\nu}\psi = 0, \tag{4.38}$$

which has the bounded solution $\psi = e^{-\sqrt{2q/\nu}y}$ for $y > 0$, corresponding to the exponential decay of the director away from the optical beam in the presence of a pre-tilt low-frequency electric field.

Finally, it's important to remark that the all-optical director response $\psi$ should remain *small* for the equations (4.5) and (4.6) to be valid. In practical terms, this means that $\psi$ should not exceed 0.25 radians ($\sim 15°$), under this condition the relative error of the small-angle approximation remains below 1%, which

assures the validity and accuracy of the paraxial approximation and the Taylor expansions performed in the equations (3.16) and (3.17).

### 4.4.2 Power dependence of the diode-like effect

In the linear beam limit (negligible all-optical reorientation $\psi \approx 0$) FP and BP wavepackets follow indistinguishable evolution without transverse separation of the trajectories, i.e $\Delta y = y_{BP}(z = 0) - y_{FP}(z = 0) = 0$, as seen in Figures 4.10,4.11 and 4.12. Moreover, self-focusing is not sustainable, and propagation is dominated by diffraction after a short distance; highlighting the critical importance of the nonlinear response in the nematicon generation and the diode-like effect.

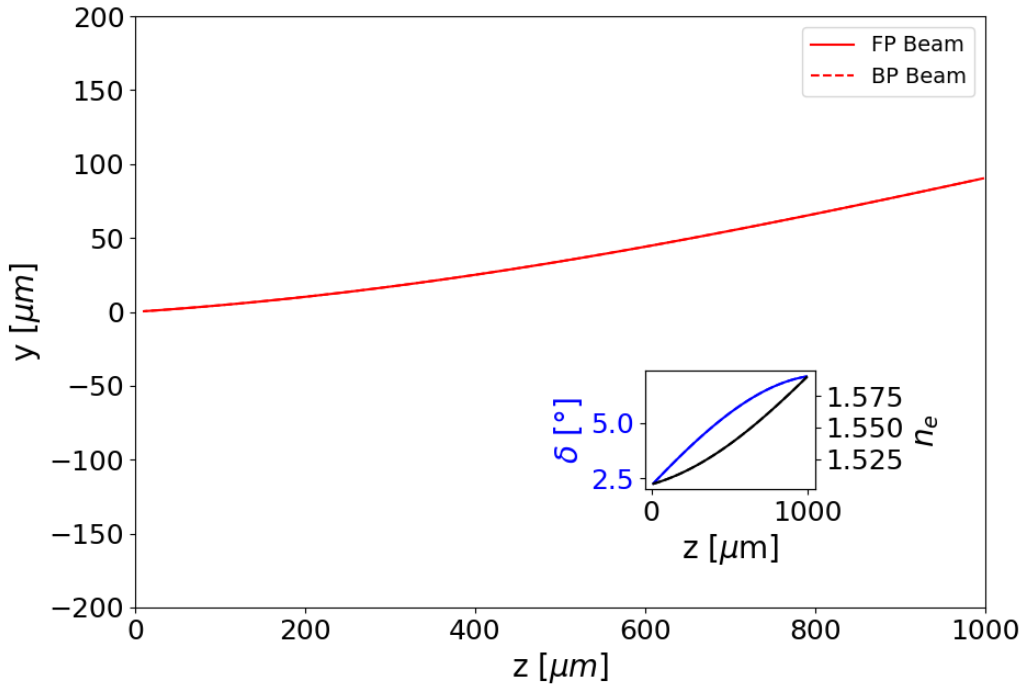


Figure 4.10: Beam trajectory in the linear limit for an input beam of dimensional power $P_b = 3.1\ mW$, width $W_b = 4.2\ \mu m$. The nonlocality is given by $\nu = 250$ and the background modulation defined by $\theta_0 = 10°$ and $\theta_L = 45°$. Inset: Computed linear walk-off $\delta$ (blue) and extraordinary refractive index $n_e$ (black)

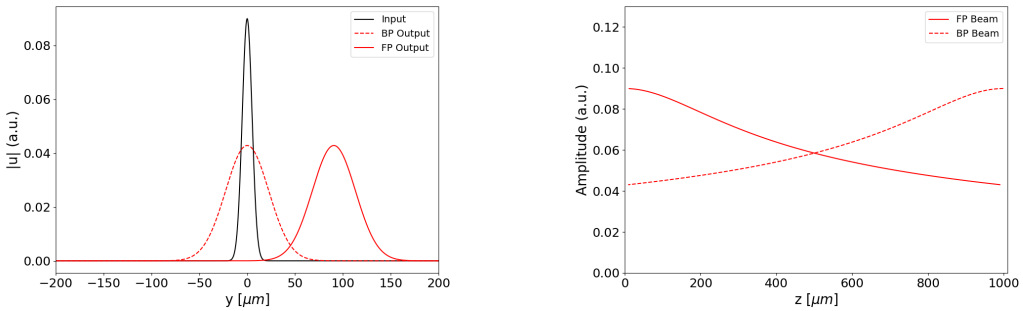


Figure 4.11: (a) Transverse profiles of input beam (black), FP beam at $z = L$ (red solid line), BP beam at $z = 0$ in the linear limit ($\psi = 0$). (b) dimensionless amplitudes of FP(solid line) and BP (dashed line) beams

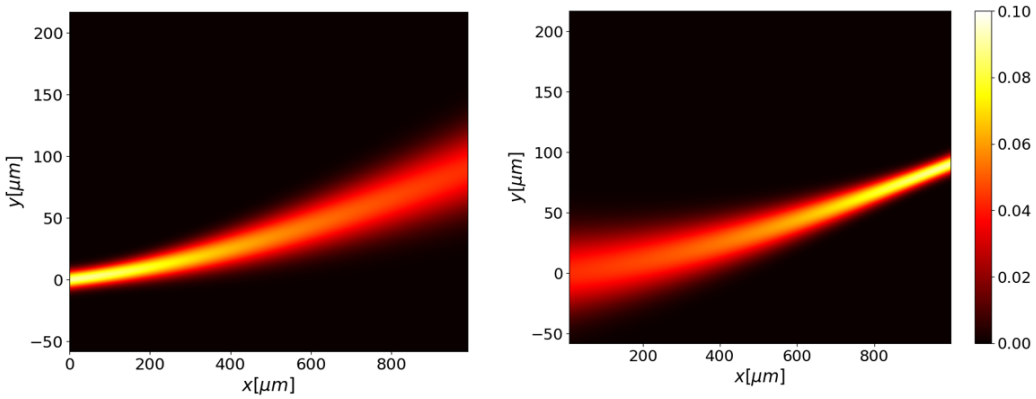


Figure 4.12: Acquired beam evolution in $(y, z)$ plane of FP (Left) and BP (Right) beams in the linear limit

In the reorientational regime, the transverse separation $\Delta y$ at $z = 0$ between the FP and BP wavepackets is a function of the input power and increases with it. Figure 4.13 (a) and (b) show the calculated transverse separation of FP and BP nematicons versus input power for the configurations of Figure 4.5. and 4.9, respectively. Due to the finite width of the solitary waves, cross-talk between (extraordinarily polarized) signals guided along FP and BP nematicons is present and could be minimized by adjusting NLC parameters, excitations and sample length, allowing for potential diode optimization.

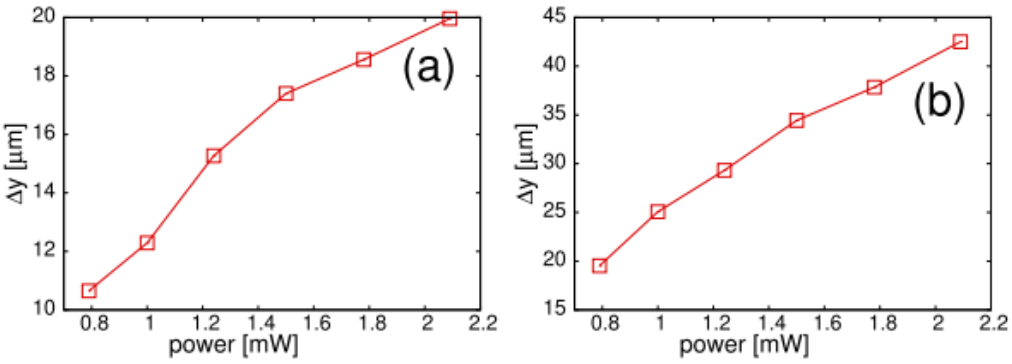


Figure 4.13: Isolator performance: nematicon waveguide-to-waveguide separation $\delta y$ versus input power. Self-trapping resulted from all excitations in the range (a) Sample with $\theta_0 = 45°$,$\theta_L = 80°$. (b) Sample with $\theta_0 = 25°$, $\theta_L = 65°$. Reproduced with permission from Opt. Lett. 47(11), 2782-2785 (2022) [119].

The transverse separation of the resulting trajectories yields an effective diode-like transmission, as the BP output port (transverse location) does not coincide with the FP input port, even if the BP beam is launched from the FP output. Otherwise stated, the backward transmission through the FP input port is negligible as the FP and BP trajectories do not overlap (notwithstanding the residual signal cross talk), effectively resulting in an optical diode-like behaviour through power-dependent direction-sensitive transmission. The latter diode, yielding a non-symmetric scattering matrix by way of the NLC reorientational response in a geometry with signal ports defined by light-induced nematicon waveguides, operates as a two-port all-optical diode device.

### 4.4.3 Dependence on the background directors angle

In the absence of nonlinear reorientational effects, the walk-off (4.3) is maximum when the reorientation angle $\Theta$ is $\pi/4$, the presence of an additional all-optical reorientation given by $\psi$ causes the director angle to be $\Theta = \theta_b(z) + \psi$, with $\theta_b \in [\theta_0, \theta_L]$, and the optical nonlinear response now varies when the angle $\theta_L$ is over or below $\pi/4$.

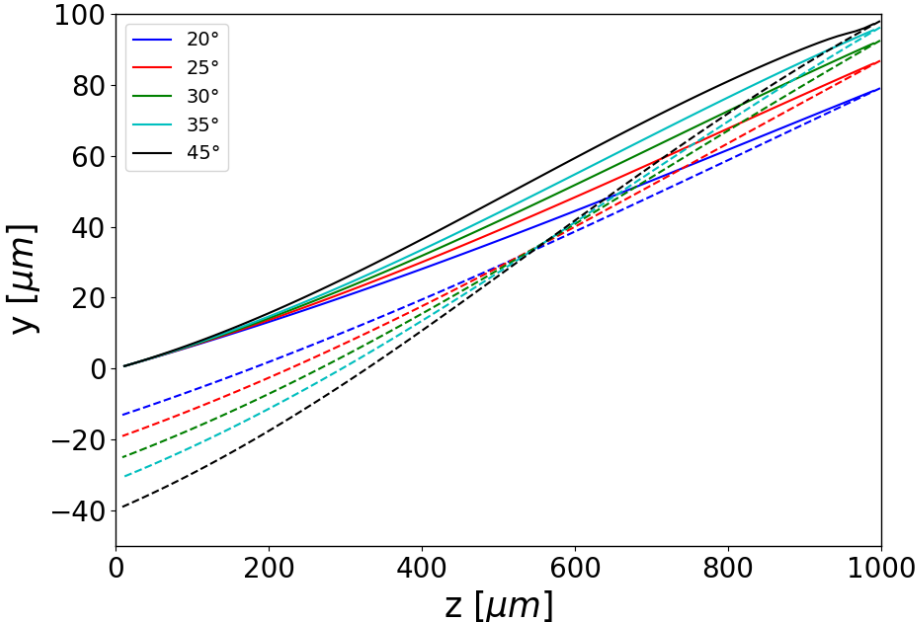


Figure 4.14: FP (solid lines) and BP (dashed lines) trajectories when $\theta_L \leq \pi/4$ for an input beam of dimensional power $P_b = 3.1\ mW$, width $W_b = 4.2\ \mu m$.

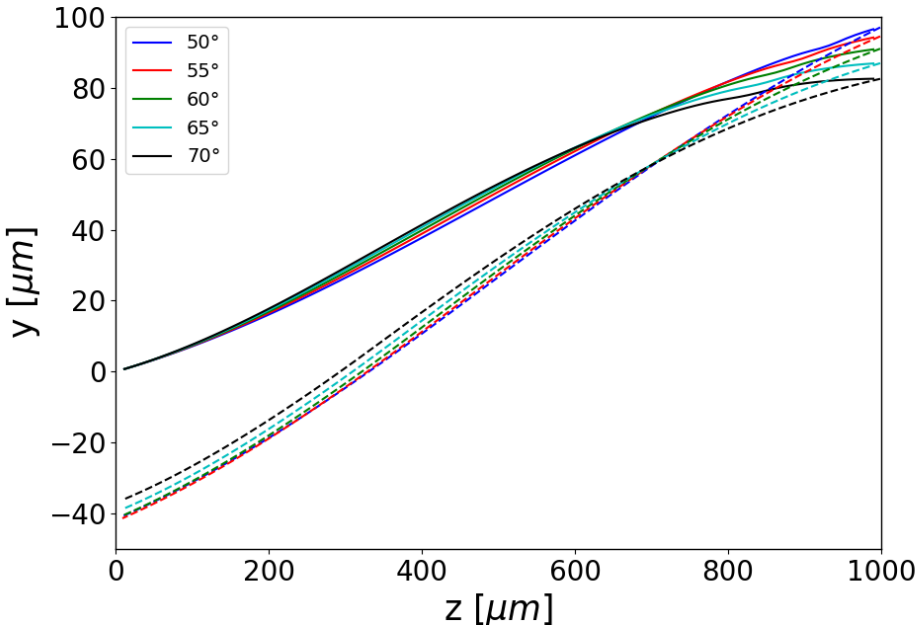


Figure 4.15: FP (solid lines) and BP (dashed lines) trajectories when $\theta_L \geq \pi/4$ for an input beam of dimensional power $P_b = 3.1\ mW$, width $W_b = 4.2\ \mu m$. The initial angle remains fixed $\theta_0 = 10°$

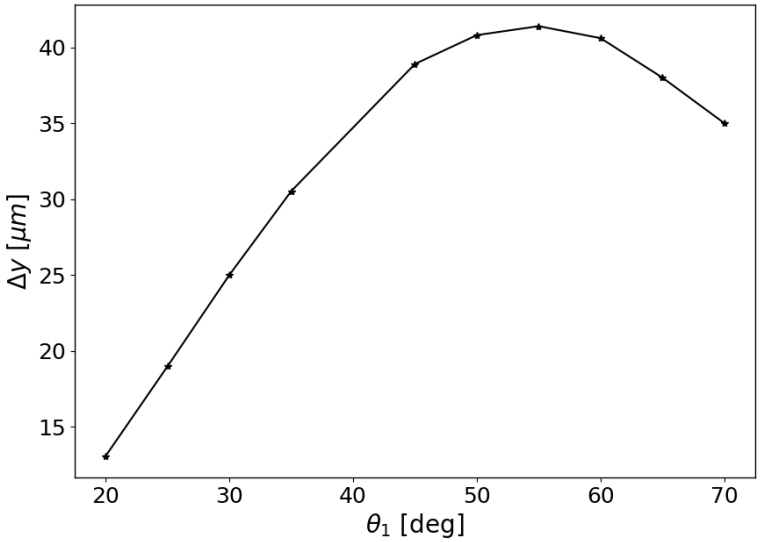


Figure 4.16: Isolator performance: nematicon waveguide-to-waveguide transverse separation $\Delta y$ (distance between the FP and BP solitary peaks on axis at $z = 0$) versus $\theta_1$ for an input beam of dimensional power $P_b = 3.1\ mW$, width $W_b = 4.2\ \mu m$. The initial angle remains fixed $\theta_0 = 10°$. Self-trapping resulted from all excitations in the range. Squares are computed values, lines are guides to the eye.

We noted that the transverse separation $\Delta y$ between the FP and BP solitary peaks on the axis at $z = 0$ increases with $\theta_1$ until it achieves a maximum around $\theta_1 = 55°$. FP and BP beams experience unequal radiation losses due to changes in the medium depending on the relative distance between their position and the point where the maximum walk-off is achieved, in other words, both beams must pass over a point $z^*$ where the total angle reorientation at that point $\Theta = \theta_b(z^*)+\psi(z^*)$ maximizes the nonlinear walk-off, but due to the power dependence of the nonlinear walk-off and the asymmetry in the increase of the extraordinary refractive index for the all-optical response $\psi$ is not the identical between FP and BP beams.

### 4.4.4 Effect of nonlocality and losses on the diode

The large nonlocality parameter $\nu$ in the director response equation (4.6), provides a nonlocal response (See Section 4.4.1) that extends across distances much larger than the size of the optical excitation (beam spot size or width). The direction-dependent routing and consequent diode-like behaviour observed here are then affected by the intrinsic nonlocality of the nematic. Figure 4.17 (a) compares the diode response in two NLC samples with a different nonlocality range $\nu$ (this can be achieved by engineering samples with different elastic constants $K$). With a larger nonlocality the FP-BP waveguide separation $\Delta y$ reduces as the overall nonlinear optical response $\psi$ decreases in magnitude [124]. On the other hand, in non-absorbing liquid crystals (such as the commercials E7 or 5CB),

inherent Rayleigh scattering is the main responsible for losses, with the loss constant $\alpha$ (sometimes referred to as absorption constant) (c.f. Equation (3.29)) taking values between $\mathcal{O}(1)$ $cm^{-1}$ to $\mathcal{O}(100)$ $cm^{-1}$ [125], depending on the sample thickness (thicker samples scatter more intensely). Figure 4.17 (b) compares the lossless nematicon waveguide routing with the case of realistic linear losses, i.e. an intensity variation given by $I(z) = I_0 \exp(\alpha z)$. We expect scattering losses to play a significant role in the (2+1)-D model increasing the optical beam power necessary to sustain nematicon confinement along the length of the sample.

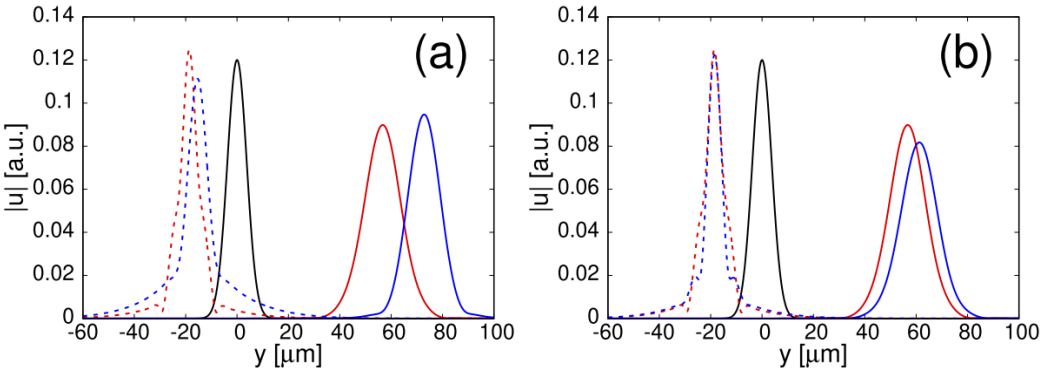


Figure 4.17: Diode transmission dependence on nonlocality and losses for a 1.7 $mW$ input beam (black solid lines) with $\theta_0 = 45°$ and $\theta_L = 80°$. FP (solid lines) and BP (dashed lines) nematicon profiles (a) in a lossless sample for $\nu = 350$ (red) or $\nu = 500$ (blue) and (b) in a sample with $\nu = 350$ for $\alpha = 0$ $cm^{-1}$ (red) or $\alpha = 15$ $cm^{-1}$(blue). Reproduced with permission from [119].

We observed that scattering losses contribute slightly to the transverse separation between the FP and BP respective waveguides. This is a consequence of the adopted (1+1)-D reduced model defined by Equations (4.5) and (4.6), which to practical effects neglects thickness scattering losses, while the low-power threshold allows for evolution compatible with self-location in the presence of losses. It is necessary to increase the scattering losses by a factor of 10, i.e. $\alpha = 150$ $cm^{-1}$ (while keeping the optical beam power compatible with self-localization) to result in noticeable differences, as seen in Figure 4.18 for an input beam of dimensional power $P_b = 3.1$ $mW$, width $W_b = 4.2$ $\mu m$. Figure 4.19 shows a comparison of the BP output profiles when the nonlocality parameter $\nu$ is increased in the presence of scattering losses $\alpha = 15$ $cm^{-1}$ resulting in significant crosstalk as the nonlocality increases.

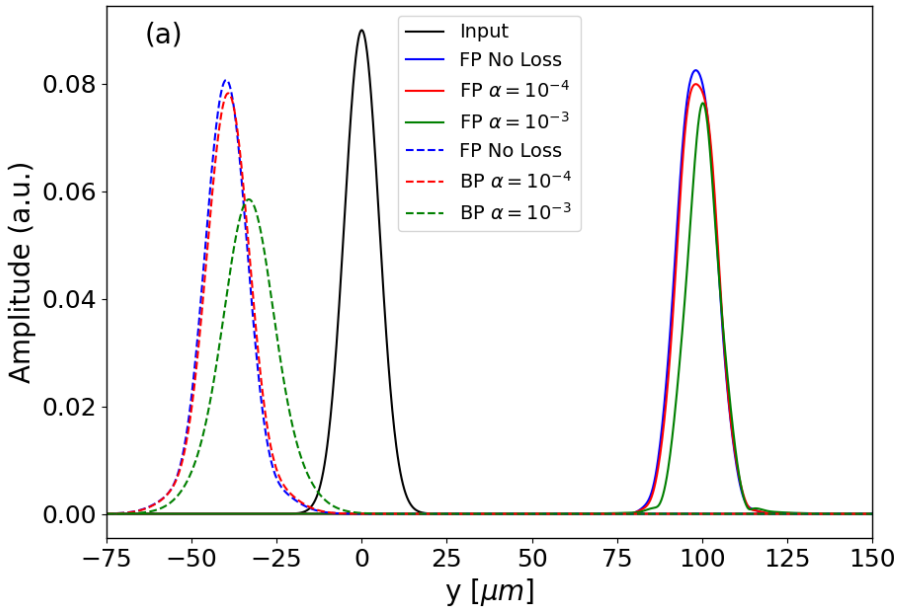


Figure 4.18: Diode transmission dependence on losses for an input beam of dimensional power $P_b = 3.1\ mW$, width $W_b = 4.2\ \mu m$. The nonlocality is given by $\nu = 250$ and the background modulation defined by $\theta_0 = 10°$ and $\theta_L = 45°$. The scattering losses $\alpha$ are nondimensional units

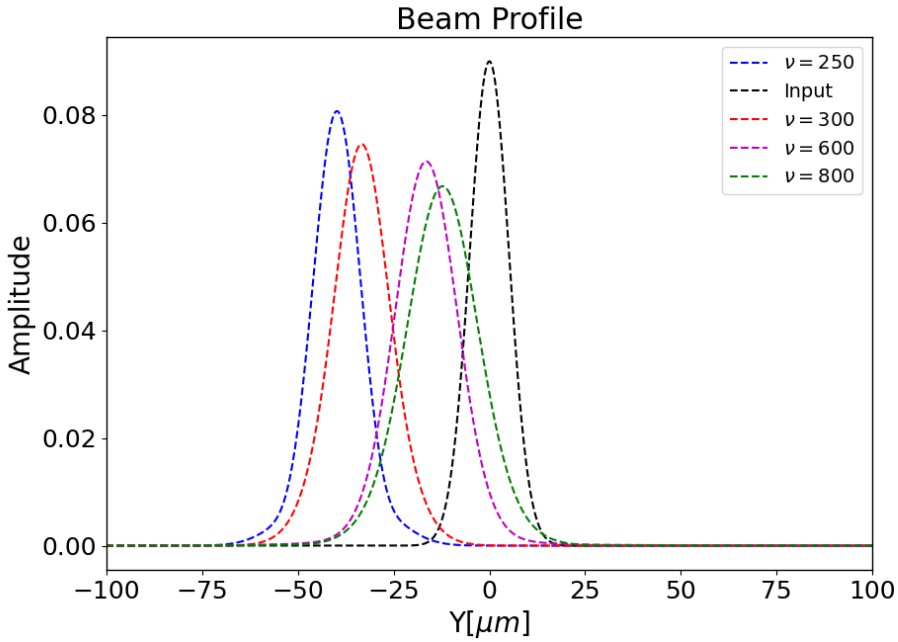


Figure 4.19: Comparison of the effects of increasing the nonlocality parameter $\nu$ on the BP output in the presence of scattering losses for an input beam of dimensional power $P_b = 3.1\ mW$, width $W_b = 4.2\ \mu m$.

### 4.4.5 High birefringence diode transmission performance enhancement

The high NLC birefringence results in large walk-off angles, making nematicon steering feasible with large displacements; at the same time, electrode patterning allows engineering of the induced background modulation of director distribution, that is, the refractive index for extraordinarily polarized light waves. We can explore the enhancement of diode-like transmission by employing nematic liquid crystals with high birefringence. For this, we consider experimental refractive index values reported by Dabrowski [145] for tolane compounds which exhibit nematic phase with a high birefringent effect ($n_\perp = 1.56$ and $n_\parallel = 1.86$), as expected, we find that the transverse separation between FP and BP beams increases in higher birefringence media and results are displayed in Figures 4.20 and 4.21.

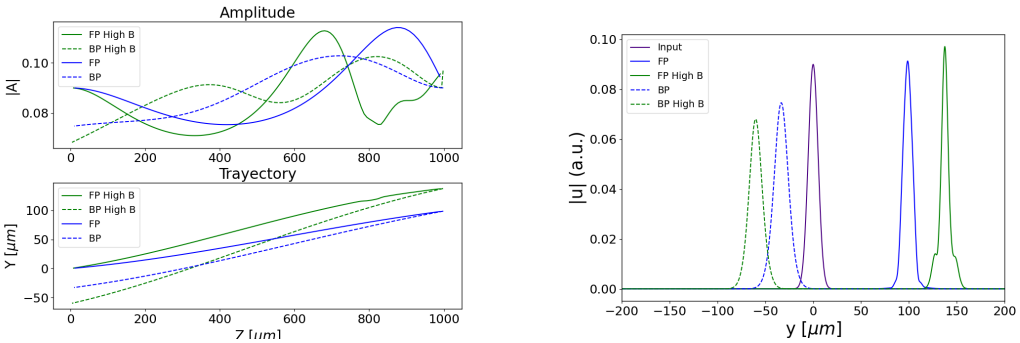


Figure 4.20: Left: Trajectories for high birefringence medium (green) and E7 (blue) for an input beam of dimensional power $P_b = 3.1\ mW$, width $W_b = 4.2\ \mu m$. The nonlocality is given by $\nu = 250$ and the background modulation defined by $\theta_0 = 10°$ and $\theta_L = 45°$. Right: Corresponding profiles for both regimes.

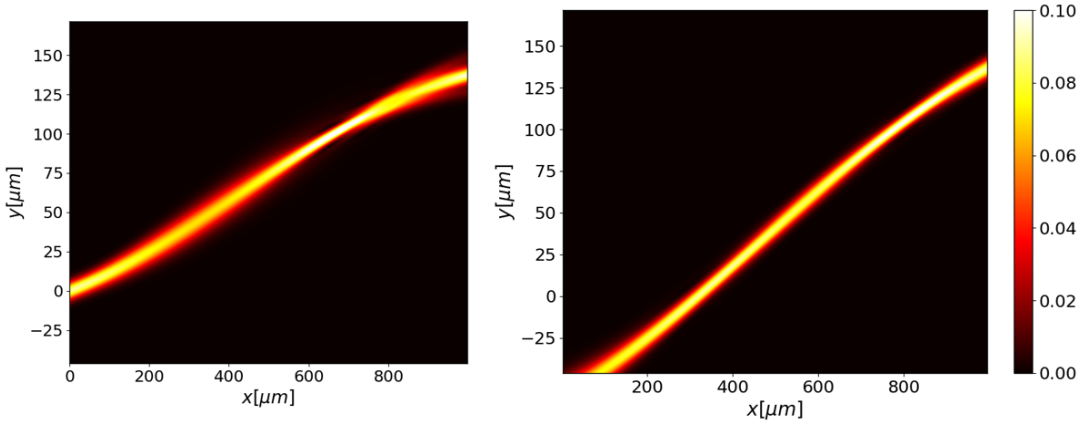


Figure 4.21: Acquired beam evolution in $(y, z)$ plane of FP (Left) and BP (Right) beams a high birefringence medium with $n_\perp = 1.56$ and $n_\parallel = 1.86$). Parameters as in Figure 4.20

The interest in studying the performance of all-optical devices in high birefringence liquid crystal lies not only in their larger optical response but in their reduced response times (See comments in Section 2.3.2) which have decreased in the last decades from 25 $ms$ to 3 $ms$ and below [148], by engineering liquid crystal mixtures with high birefringence and low rotational viscosity [145].

## 4.5 Transverse linear modulation

We proceed to replicate the previous study for a linearly varying modulation $\theta_b$ of the optical axis along the transverse coordinate $y$ in the principal plane $(y, z)$ as sketched in Figure 4.22, namely,

$$\theta_b = \theta_b(y) = \theta_b + \left(\frac{\theta_{top} - \theta_{bot}}{d}\right)\left(y + \frac{d}{2}\right) \tag{4.39}$$

where $\theta_{top}$ and $\theta_{bot}$ are the angles at the top and bottom end of the cell (along $y$) respectively. The results detailed in this section are presented in an article published in the published article Physical Review A 108 (4), 043509 [146] (see Appendix A).

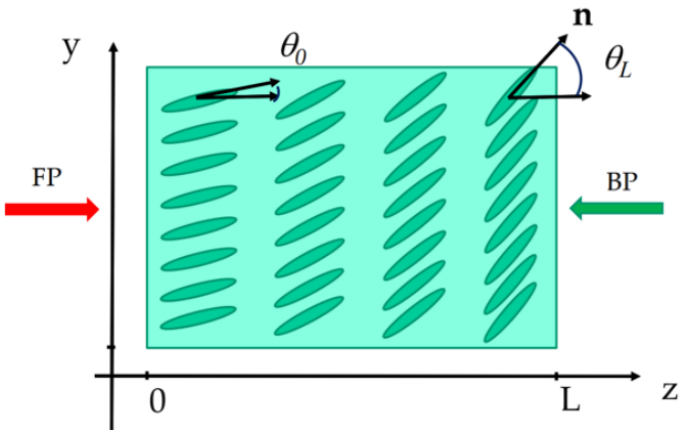


Figure 4.22: Sketch of a thick planar cell with linearly varying orientation along the transverse $y$ direction; $\theta_{bot}$ is the director angle in $y = y_{bot} = -d/2$ and $\theta_{top}$ the director orientation in $y = y_{top} = d/2$. The red arrow indicates the input of the FP beam, and the green arrow to the BP beam. Reproduced from [146], Copyright (2023) by the American Physical Society.

As in the previous case of longitudinal modulation, a reduced (1+1)D model of two coupled equations for nonlinear propagation and light-induced reorientation along and across the wavepacket is appropriate.

In the paraxial, slowly varying envelope approximation, the (1+1)-D equations

governing the propagation of a light beam in a NLC are given by

$$2ik_0n_e\frac{\partial E_y}{\partial z}+2ik_0n_e\Delta(\Theta)\frac{\partial E_y}{\partial y}+\frac{\partial^2E_y}{\partial y^2}+k_0^2\left(n_\perp^2\cos^2\Theta+n_\parallel^2\sin^2\Theta-n_\perp^2\cos^2\theta_0\right.$$
$$\left.-n_\parallel^2\sin^2\theta_0\right)E_y=0, \tag{4.40}$$

for the dimensional electric field of the light beam and

$$K\frac{\partial^2\Theta}{\partial y^2}+\frac{1}{4}\epsilon_0\Delta\epsilon|E_y|^2\sin 2\Theta=0, \tag{4.41}$$

for the medium response.

Here, $\Theta=\theta_0(0)+\theta_b(y,z)+\psi(x,y,z)$, with $\psi$ the all-optical reorientation. If we assume that $|\psi|\ll\theta_0$, but that $\theta_b$ is not necessarily small, the electric field equation becomes

$$2ik_0n_e\frac{\partial E_y}{\partial z}+2ik_0n_e\Delta(\Theta)\frac{\partial E_y}{\partial y}+\frac{\partial^2E_y}{\partial y^2}+k_0^2\left[n_\perp^2\left(\cos^2(\theta_0+\theta_b)-\cos^2\theta_0\right)\right.$$
$$\left.+n_\parallel^2\left(\sin^2(\theta_0+\theta_b)-\sin^2\theta_0\right)+\Delta\epsilon\sin 2(\theta_0+\theta_b)\,\psi\right]E_y=0. \tag{4.42}$$

Using $\cos^2(\theta_0+\theta_b)=1-\sin^2(\theta_0+\theta_b)$ gives

$$2ik_0n_e\frac{\partial E_y}{\partial z}+2ik_0n_e\Delta(\Theta)\frac{\partial E_y}{\partial y}+\frac{\partial^2E_y}{\partial y^2}+k_0^2\Delta\epsilon\left[\sin^2(\theta_0+\theta_b)-\sin^2\theta_0\right.$$
$$\left.+\sin 2(\theta_0+\theta_b)\,\psi\right]E_y=0. \tag{4.43}$$

On the other hand, the director equation becomes

$$K\frac{\partial^2\psi}{\partial y^2}+\frac{1}{4}\epsilon_0\Delta\epsilon|E_y|^2\sin 2(\theta_0+\theta_b)=0, \tag{4.44}$$

where we use that $\theta_b(y,z)$ varies linearly, then $\nabla^2\theta_b=0$, and we recover (3.15) and (3.16) in the (1+1)-D model.

In the case of a longitudinal modulation $\theta_b=\theta_b(z)$, it was possible to simplify the electric field equation (See Chapter 3, Equation (3.17)) using the phase transformation

$$E_y=\bar{E}_y\exp\left(\frac{ik_0}{2n_e}\int_0^z\left\{\Delta\epsilon[\sin^2(\theta_0+\theta_b)-\sin^2\theta_0]\right\}du\right) \tag{4.45}$$

Now, for a transverse modulation $\theta_b=\theta_b(y)$, the electric field equation (4.40) can not be simplified using the same phase transformation. One would be tempted to use the phase transformation

$$E_y=\bar{E}_y\exp\left(\frac{ik_0}{2n_e\Delta(\Theta)}\int_0^y\left\{\Delta\epsilon[\sin^2(\theta_0+\theta_b)-\sin^2\theta_0]\right\}du\right) \tag{4.46}$$

which does not work, as $\Delta(\Theta)$ depends on $y$ through the definition of $\Theta$.

Coming back to equations (4.43) and (4.44), we can now non-dimensionalise the electric field equation and the director equation using

$$x = WX, \quad y = WY, \quad z = BZ, \quad E_y = A_b u. \tag{4.47}$$

We then find

$$i\frac{4n_e}{k_0\Delta\epsilon B}\frac{\partial u}{\partial Z} + i\frac{4n_e}{k_0\Delta\epsilon W}\Delta(\psi)\frac{\partial u}{\partial Y} + \frac{2}{k_0^2\Delta\epsilon W^2}\frac{\partial^2 u}{\partial Y^2} + \left[\sin^2(\theta_0+\theta_b) - \sin^2\theta_0 + \sin 2(\theta_0+\theta_b)\,\psi\right]u = 0, \tag{4.48}$$

$$\frac{8K}{\epsilon_0\Delta\epsilon A_b^2 W^2}\frac{\partial^2\psi}{\partial Y^2} + 2|u|^2\sin 2\left(\theta_0+\theta_b\right) = 0 \tag{4.49}$$

We then take

$$\frac{4n_e}{k_0\Delta\epsilon B} = 1 \quad \text{and} \quad \frac{2}{\Delta\epsilon k_0^2 W^2} = 1. \tag{4.50}$$

Solving we have

$$B = \frac{2\lambda n_e}{\pi\Delta\epsilon} \quad \text{and} \quad W = \frac{\lambda}{\pi\sqrt{\Delta\epsilon}}. \tag{4.51}$$

To find $A$ we use a Gaussian reference beam of power $P_b$, amplitude $A_b$ and width $W_b$, where $P_b$ and $W_b$ are based on a Gaussian reference beam of typical values $P_b = 2.7mW$ and full width $3.5\mu m$. Then

$$P_b = \frac{\pi}{2}\Gamma A_b^2 W_b^2, \quad A_b^2 = \frac{2P_b}{\pi\Gamma W_b^2}. \tag{4.52}$$

The non-dimensional equations are then

$$i\frac{\partial u}{\partial Z} + i\gamma\Delta(\Theta)\frac{\partial u}{\partial Y} + \frac{1}{2}\frac{\partial^2 u}{\partial Y^2} + \left[\sin^2(\theta_0+\theta_b) - \sin^2\theta_0 + \sin 2(\theta_0+\theta_b)\,\psi\right]u = 0, \tag{4.53}$$

$$\nu\frac{\partial^2\psi}{\partial Y^2} + 2|u|^2\sin 2\left(\theta_0+\theta_b\right) = 0. \tag{4.54}$$

Here

$$\nu = \frac{2\pi^3 c n_e K W_b^2}{\lambda^2 P_b}, \quad \gamma = \frac{2n_e}{\sqrt{\Delta\epsilon}}. \tag{4.55}$$

Note that $\gamma$ is the same as the $z$ dependent case (c.f Equation (4.16)) but without the $\sin 2\theta_0$ term.

Using realistic NLC physical parameters and sample features, we analyze the role of a transversally modulated background orientation and nonlocality, power and losses, demonstrating the feasibility of solitary wave-based nonspecular signal transmission featuring direction-dependent beam and signal routing.

Within this simple configuration of a transversely non-uniform director ar-

rangement, two regimes were considered:

(i) Trajectories when the increase of the walk-off and refractive index counteract.

(ii) Trajectories when the walk-off and the refractive index act in the same direction.

## 4.6 Results For Transverse Modulation

In the numerical experiments, we adopted material parameters characteristic of the standard NLC mixture E7, with $n_{\parallel} = 1.7$, $n_{\perp} = 1.5$ and $K = 1.2 \times 10^{-11} N$, with nonlocality $\nu = 250$ (at variance with Section 4.4). A NLC planar cell was chosen with dimension $30\mu m \times 600\mu m \times 1mm$ in $(h, d, L)$, this in order to minimize any potential boundary effect. We neglect scattering losses and consider an input of dimensional power of $P = 2.43mW$ and full-width $4.2\mu m$. First, we studied the effects of walk-off and refraction on the FP and BP paths for the case of a director alignment varying at the linear rate $40°/600\mu m$ across the cell width. Higher rates of change cause a collision with the edges of the cell for the BP nematicon.

While in the case of a linear longitudinal modulation (Section 4.4) nematicons launched from opposite sites of the sample underwent different (power-dependent) walk-offs, in an NLC sample with modulation in the transverse coordinate $y$, both walk-off and refraction act on the wave packets, as they propagate through regions with modulated refraction. Figures 4.23(a)-4.23(d) show the extraordinary refractive index $n_e(y)$ and walk off $\delta(y)$ distributions in a $y-$modulated cell with orientation linearly modulated from $\theta_{bot} = 65°$ to $\theta_{top} = 25°$ across the width $d$ and an FP input launched from $(y_0, z) = (100\mu m, 0)$ with $\theta_0(y_0) = 38°$. In this case, refraction and nonlinear walk-off tend to counteract each other on the FP beam whereas they act in the same direction on the BP nematicon, with a resulting transverse separation between the solitary peaks $\Delta y \approx -180\mu m$. The increase in refractive index is monotonic across $y$ and causes refraction towards $y = -300$, whereas the initial walk-off tends to move the Poynting vector towards $y = 300$, with the walk-off and refractive index effect counteracting along the cell. The FP beam's initial direction is then affected by the transverse modulation of the director orientation, eventually leading to a reversed transverse velocity and an FP nematicon trajectory bending with the trajectory exhibiting a maximum. Figures 4.25(a)-4.25(d) display another case, where the background orientation goes from $\theta_{bot} = 25°$ to $\theta_{top} = 65°$ and the FP beam is launched from $(y_0, z) = (-200\mu m, 0)$ with $\theta_0(y_0) = 32°$ and the transverse separation is given by $\Delta y \approx 180\mu m$. We note that in this case, the role of the non-uniform orientation becomes more important earlier than in the competing case, owing to the synergistic contributions of the walk-off and phase front distortion.

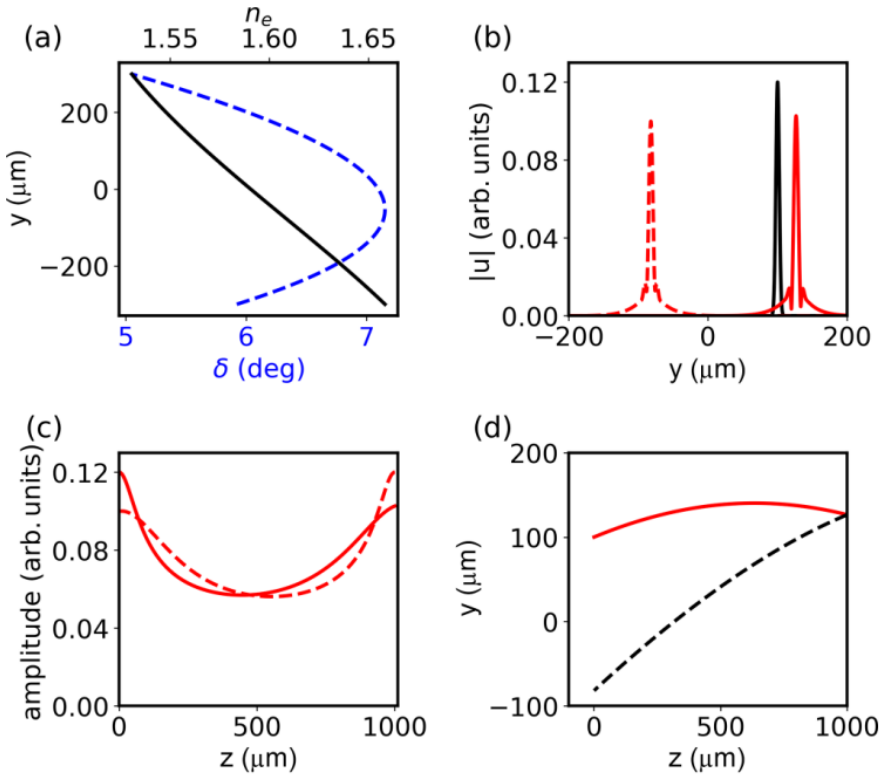


Figure 4.23: Linear transverse modulation from $\theta_{bot} = 65°$ to $\theta_{top} = 25°$ across a cell width $d = 600\mu m$. (a) extraordinary refractive index $n_e(y)$(black solid ) and angular walkoff $\delta(y)$(blue dashed). (b) Transverse profiles of input (black solid), FP output (red solid), and BP output(red dashed) nematicons. (c) Amplitudes of FP (solid) and BP (dashed) wavepackets. (d) Trajectories of FP (red solid) and BP (black dashed) nematicons. Reproduced from [146], Copyright (2023) by the American Physical Society.

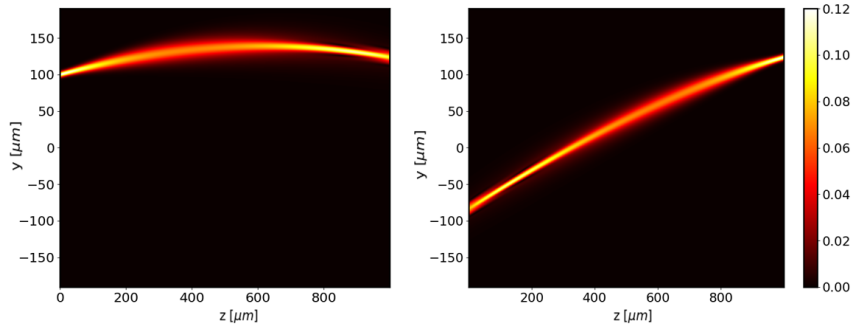


Figure 4.24: Acquired nematicon evolution in the principal $(y, z)$ plane of FP (Left) and BP (Right) nematicons for the case of Figure 4.23

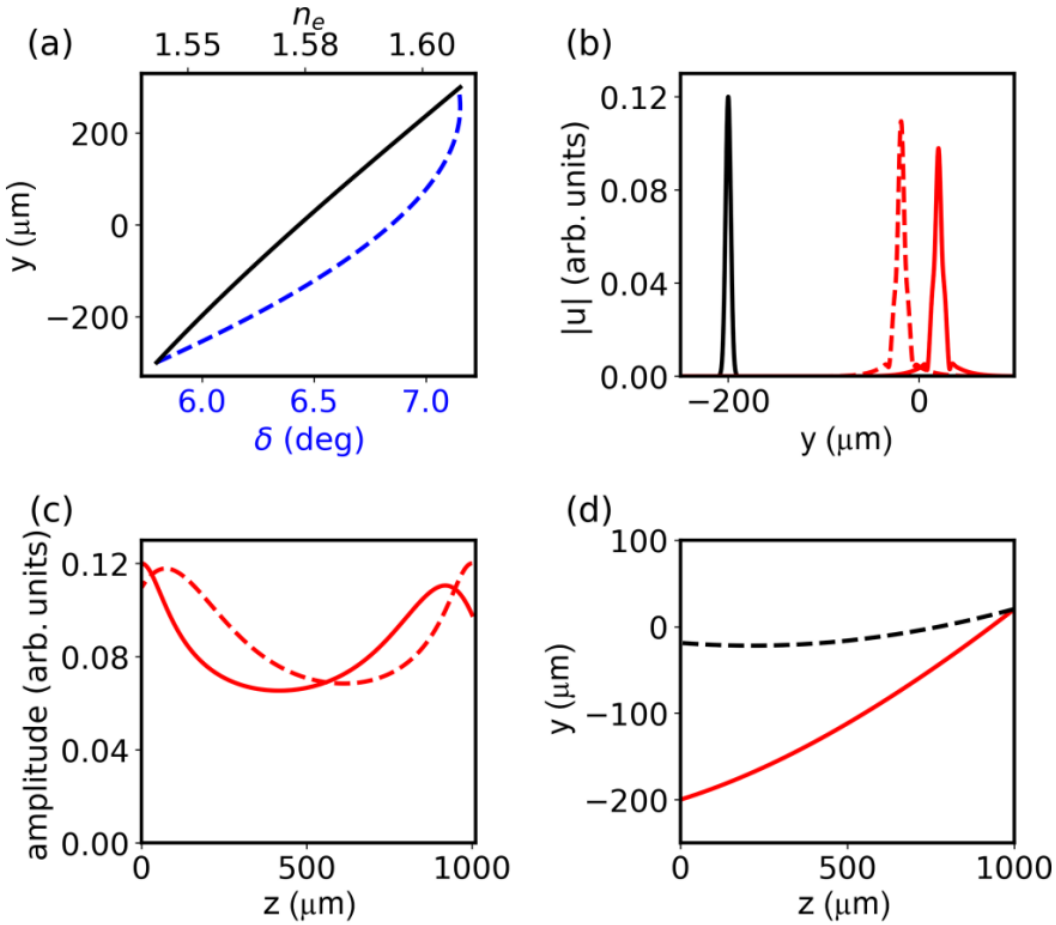


Figure 4.25: Linear transverse modulation from $\theta_{bot} = 25°$ to $\theta_{top} = 65°$ across a cell width $d = 600\mu m$. (a) extraordinary refractive index $n_e(y)$(black solid ) and angular walkoff $\delta(y)$(blue dashed). (b) Transverse profiles of input (black solid), FP output (red solid), and BP output(red dashed) nematicons. (c) Amplitudes of FP (solid) and BP (dashed) wavepackets. (d) Trajectories of FP (red solid) and BP (black dashed) nematicons. Reproduced from [146], Copyright (2023) by the American Physical Society.

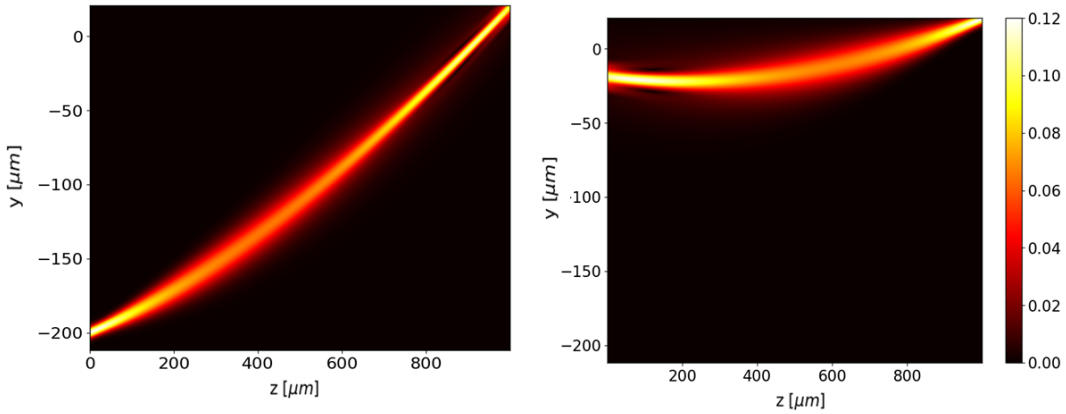


Figure 4.26: Acquired nematicon evolution in $(y, z)$ plane of FP (Left) and BP (Right) nematicons

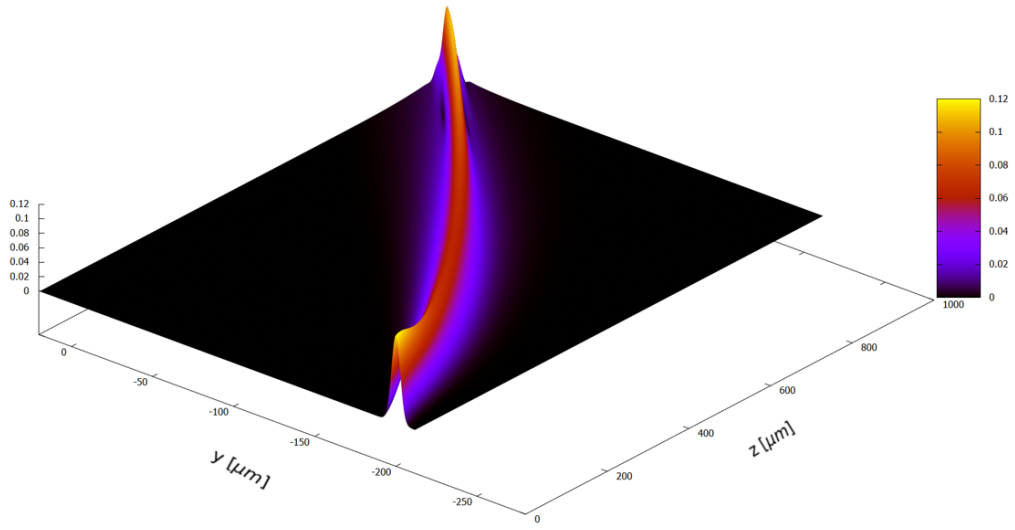


Figure 4.27: 3D plot for nematicon evolution in $(y, z)$ plane of the FP nematicon

### 4.6.1 Power dependence in the transverse modulated case

As in the $z$-modulated case (Section 4.4.2), the transverse separation $\Delta y = y_{BP}(z = 0) - y_{FP}(z = 0)$ is excitation-level dependent in the reorientational weakly nonlinear regime governed by Equations (4.46) and (4.47), Figure 4.28 (a)-(b) displays the power dependence for the two $y$-modulated cases considered before.

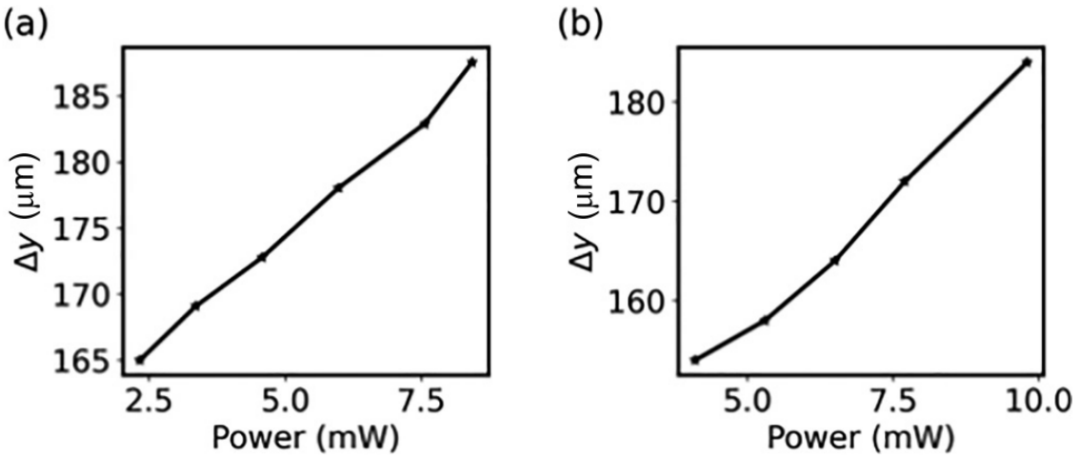


Figure 4.28: Power dependence of the transverse separation $\Delta y$ in the $y-$modulated case. (a)$\theta_{bot} = 25°$, $\theta_{top} = 65°$ and (b)$\theta_{bot} = 65°$, $\theta_{top} = 25°$. Dots are calculated points and lines are guides to the eye. Reproduced from [146], Copyright (2023) by the American Physical Society.

Figure 4.29 shows increasing transverse separation $\Delta y$ at $z = 0$ when the optical power of the input beam is increased in a $y$-modulated cell with $\theta_{bot} = 25°$ and $\theta_{top} = 65°$.

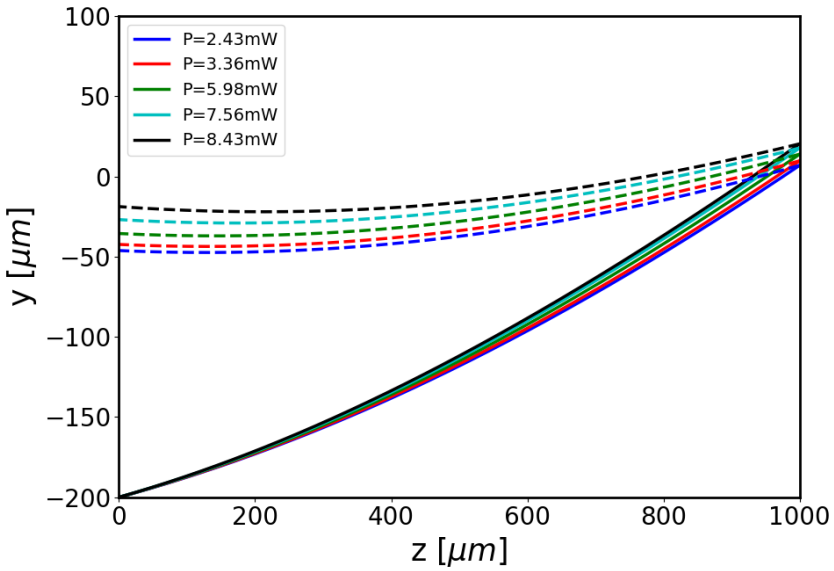


Figure 4.29: Increasing input beam power trajectories for a linear transverse modulation from $\theta_{bot} = 25°$ to $\theta_{top} = 65°$ across a cell width $d = 600\mu m$.

Similarly, Figure 4.30 shows increasing transverse separation $\Delta y$ at $z = 0$ when the optical power of the input beam is increased in a $y$-modulated cell with $\theta_{bot} = 65°$ and $\theta_{top} = 25°$.

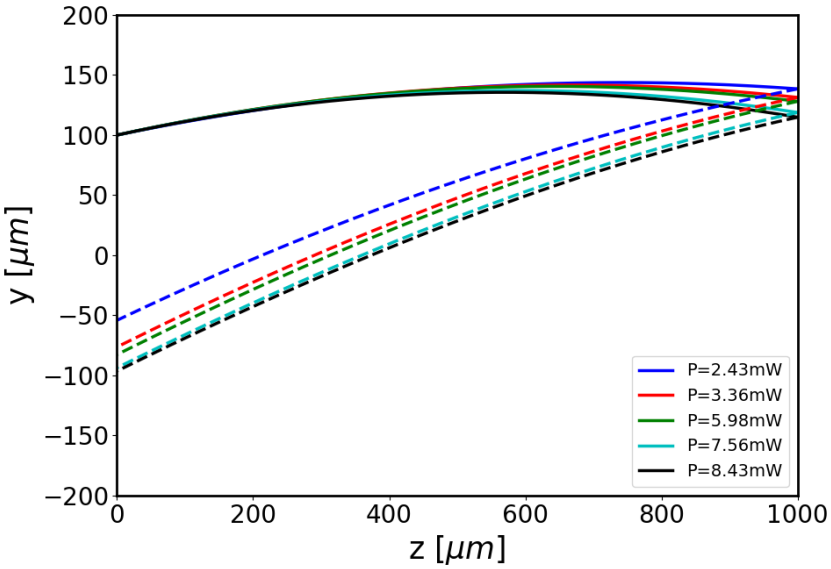


Figure 4.30: Increasing input beam power trajectories for a linear transverse modulation from $\theta_{bot} = 65°$ to $\theta_{top} = 25°$ across a cell width $d = 600\mu m$.

One of the drawbacks of the reduced (1+1)-D model adopted is their limited optical power operation, as the beam power can not be increased arbitrarily and input power higher than $10mW$ results in an all-optical reorientation $\psi$ comparable to or higher than the background director orientation at rest $\theta_b$, breaking down the small angle assumptions employed when deriving the equations. Furthermore, the absence of a low power threshold in the (1+1)-D equations, results in the model allowing self-focused beams with power too low to sustain nematicon propagation under experimental conditions or in the (2+1)-D model, as seen in Figure 4.31.

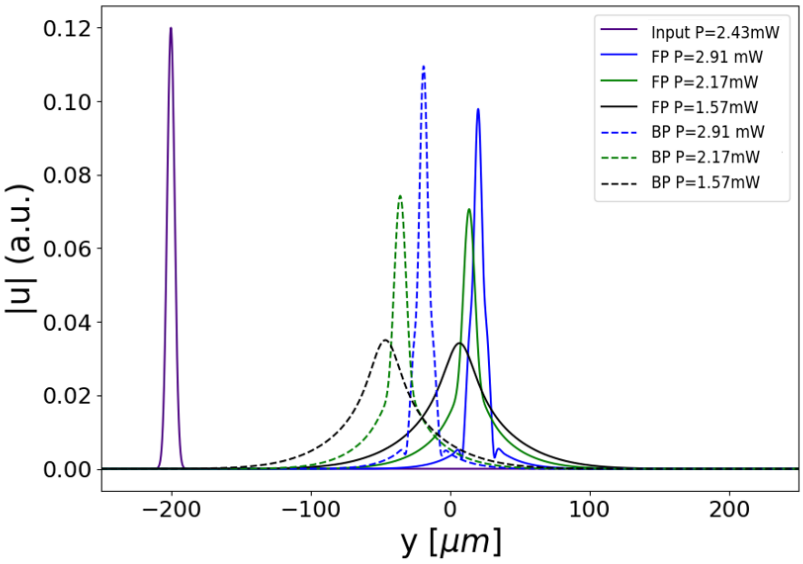


Figure 4.31: Profile comparison for different input beam power in a linear transverse modulated nematic cell from $\theta_{bot} = 65°$ to $\theta_{top} = 25°$. FP (solid) and BP(dashed) beam output profile for (i) $P = 2.43mW$ (blue), (ii) $P = 2.17mW$ (green), at this power nematicon are excited under typical experimental condition (ii)$P = 1.57mW$ (black) nematicon does not sustain themselves at this power in experimental conditions

### 4.6.2 Effect of the nonlocality

Analogously to the longitudinal modulated case of Section 4.5, the direction-dependent routing observed is affected by the intrinsic nonlocality parameter $\nu$. Figure 4.32 (a) compares the FP-BP trajectories in two NLC samples with a different nonlocality parameter $\nu$, while Figure 4.32(b) displays the corresponding beam output profiles. As expected, with a larger nonlocality the FP-BP waveguide separation $\Delta y$ reduces, while the width of the optical beams increases with $\nu$, this is consistent as the beam is trying to evolve to an exact nematicon, which increases in width as $\nu$ increases [99].

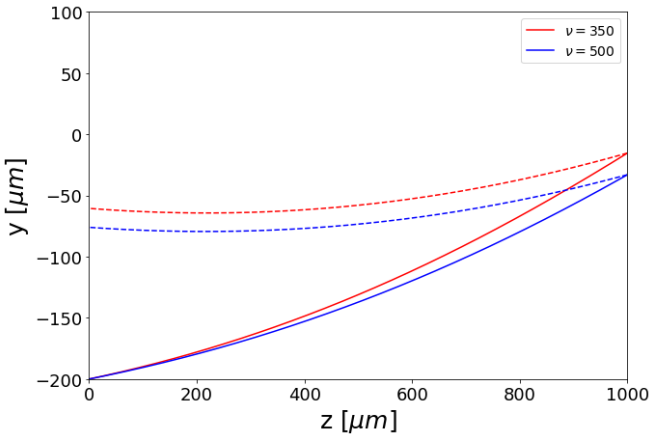


Figure 4.32: Comparison of trajectories for different values of the nonlocality parameter $\nu$; $\nu = 350$ (red) and $\nu = 500$ (blue). The input beam has dimensional power $P_b = 2.45mW$, width $W_b = 4.2\mu m$ and the $y$-dependent transverse modulation is defined by $\theta_{bot} = 15°$ and $\theta_{top} = 45°$.

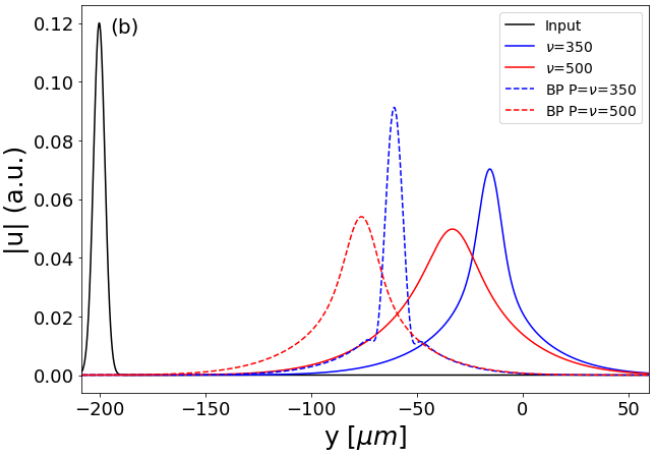


Figure 4.33: Comparison of output beam profiles for different values of the nonlocality parameter $\nu$; $\nu = 350$ (red) and $\nu = 500$ (blue). The input beam has dimensional power $P_b = 2.45mW$, width $W_b = 4.2\mu m$ and the $y$-dependent transverse modulation is defined by $\theta_{bot} = 15°$ and $\theta_{top} = 45°$.

### 4.6.3 Input angle dependence

At variance with the longitudinal modulated case, beam propagation is not independent of the input position $y_0$ at $z = 0$, since the transverse modulation entails different initial director angles, i.e. $\theta_0 = \theta_0(y_0)$. Figure 4.34 presents acquired beam evolution along $z$ for different input locations across $y$. As expected, the BP nematicon trajectory bends differently when launching the wavepacket at different initial orientations $\theta_0$, with an increase of the overall transverse separation $\Delta y$ between the FP port and the final BP nematicon position as the initial angle $\theta_0$ increases.

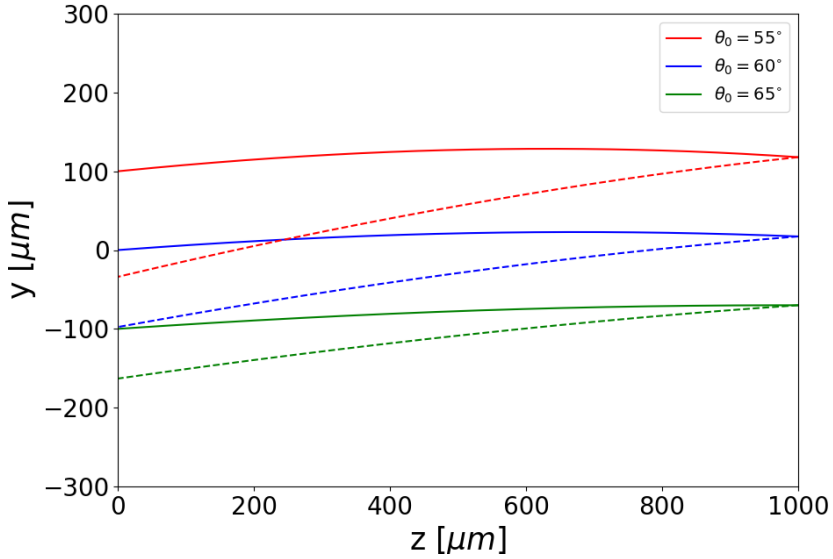


Figure 4.34: FP (solid line) and BP (dashed line) beam trajectories in $(y, z)$ for an input beam of dimensional power $P_b = 2.45mW$, width $W_b = 4.2\mu m$ and the $y$-dependent transverse modulation is defined by $\theta_0 = 75°$ and $\theta_1 = 45°$ ($\theta_{in}(y_0) = 55°$ (red lines), $\theta_{in} = 60°$ (blue lines), $\theta_{in} = 65°$ (green lines).

### 4.6.4 Comparison with the longitudinal case

The most distinguishable difference between the longitudinal and transverse modulation is the overall increase in the transverse separation $\Delta y$ between FP and BP nematicons in $z = 0$, as depicted in Figures 4.35, 4.36 and 4.37.

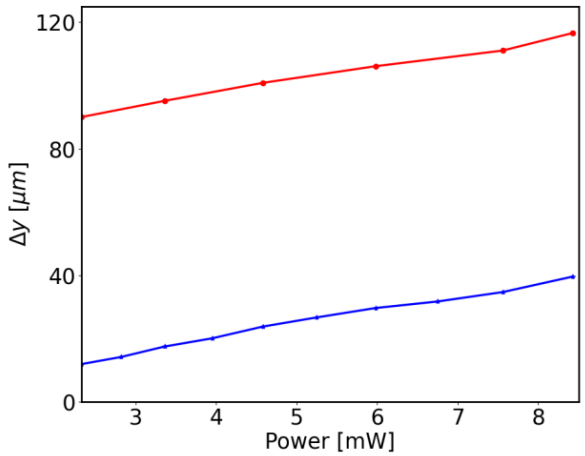


Figure 4.35: Beam power dependence of the transverse separation $\Delta y$ for linear longitudinal modulation (blue line with calculated data points) and linear transverse modulation (red line with calculated data points) for the modulation interval $\theta_b$ as in Figures 4.36 and 4.37 below, respectively. Reproduced with permission from [147].

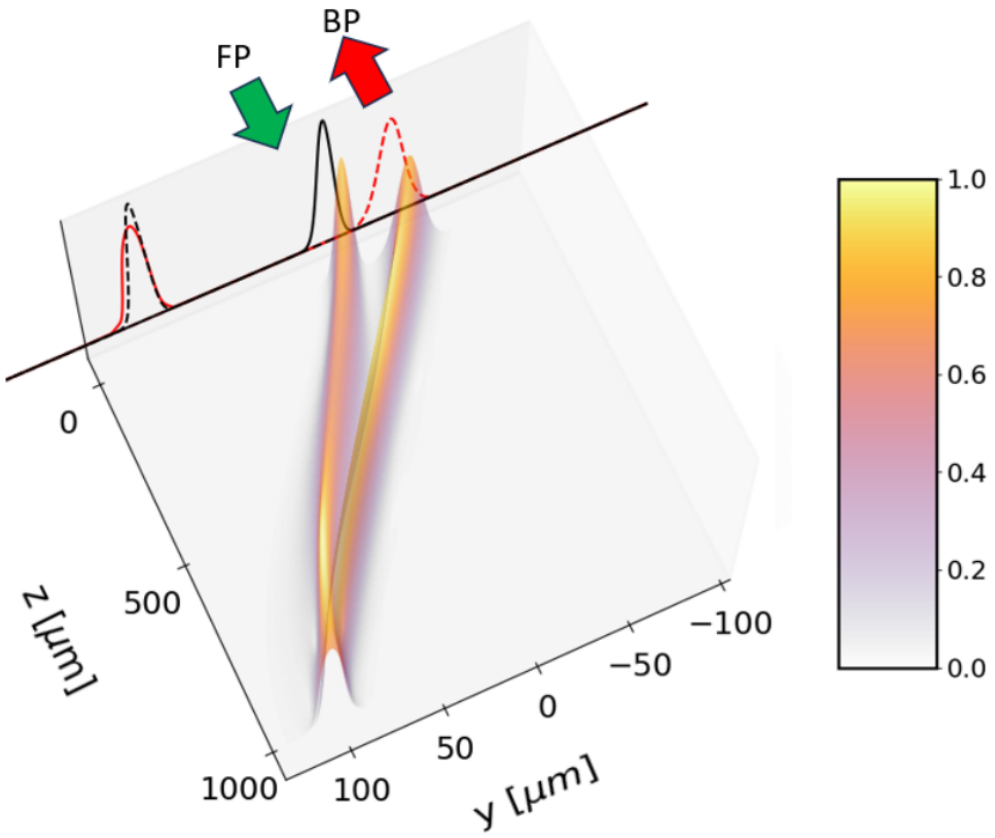


Figure 4.36: Linear longitudinal modulation of the background orientation in a $600\mu m$ sample cell from $\theta_0 = 15°$ to $\theta_L = 55°$.3D trajectories and transverse profiles of FP (green arrow) and BP (red arrow) nematicons (normalized field amplitude $u$ in arbitrary units); input (black) and output (red) beam profiles in $z = 0$,$z = L$ are also projected on the $y$ axis in $z = 0$. Reproduced with permission from [147].

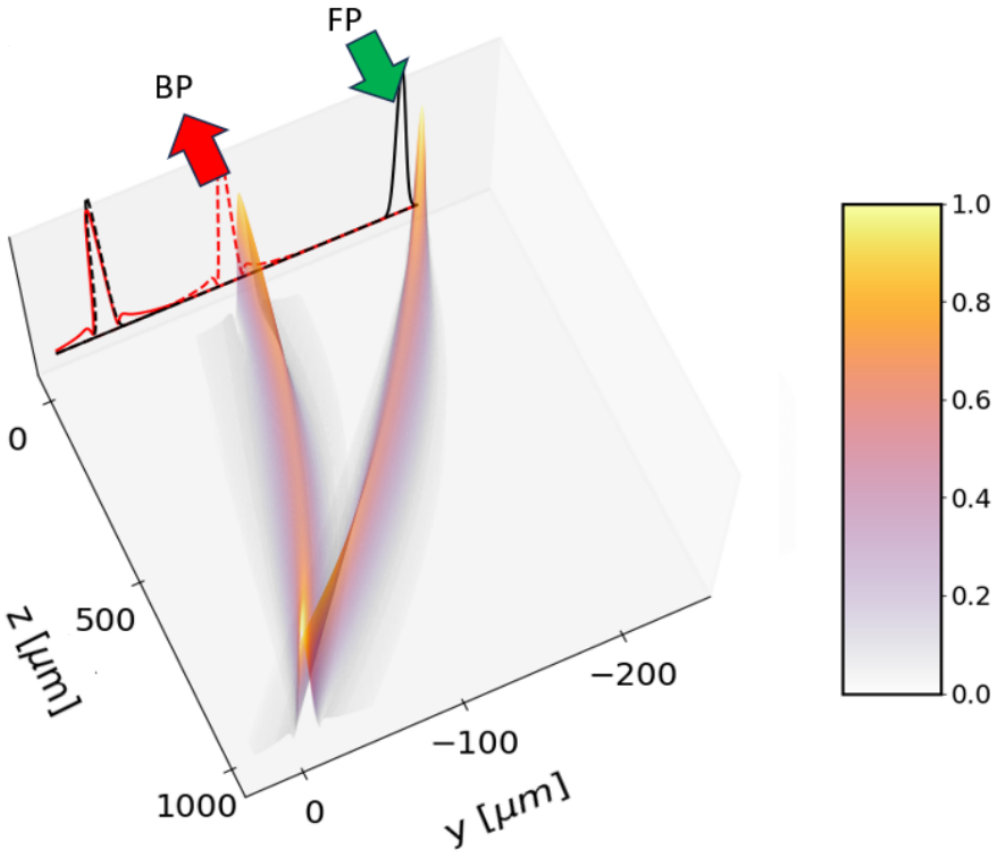


Figure 4.37: Transverse longitudinal modulation of the background orientation in a $600\mu m$ sample cell from $\theta_{bot} = 30°$ to $\theta_{top} = 50°$. 3D trajectories and transverse profiles of FP (green arrow) and BP (red arrow) nematicons (normalized field amplitude $u$ in arbitrary units); input (black) and output (red) beam profiles in $z = 0$,$z = L$ are also projected on the $y$ axis in $z = 0$. Reproduced with permission [122].

## 4.7 Combined linear y-modulation and z-modulation

The previous sections addressed either purely transverse or purely longitudinal modulations, assuming linearly varying orientation angles across the width $d$ or the length $L$ of the cell, respectively. Here, to better elucidate the phenomenon, we consider the general system (4.39) and (4.40) with a modulation in the principal plane $(y, z)$ obtained by combining $y-$ and $z-$ linearly modulated background orientations

$$\theta_b(z, y) = \theta_0 + \left(\frac{\theta_L - \theta_0}{L}\right) z \pm \theta_{bot} + \left(\frac{\theta_{top} - \theta_{bot}}{d}\right)\left(y + \frac{d}{2}\right). \tag{4.56}$$

Figure 4.38 displays typical purely transverse and longitudinal director background modulation, while Figure 4.39 shows the resulting combined background modulation obtained by (4.49) using the "plus" sign.

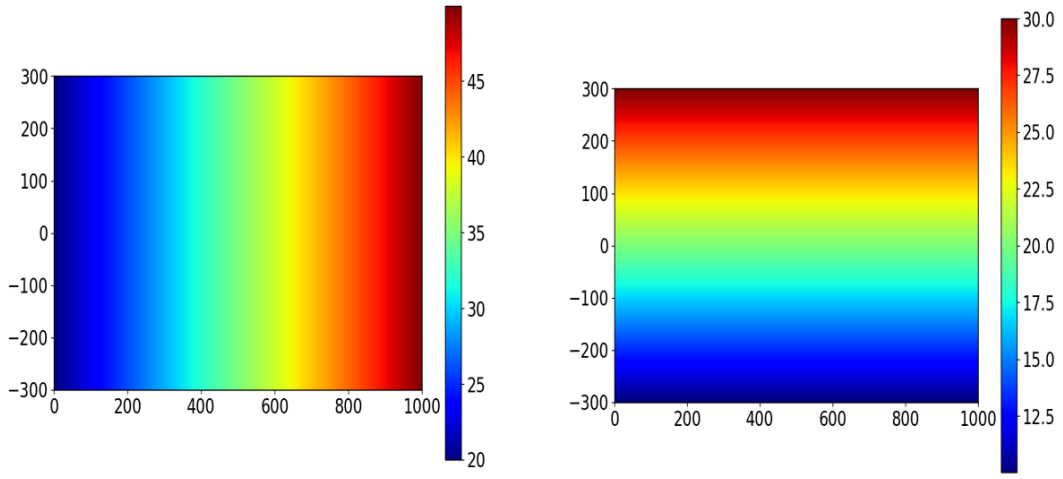


Figure 4.38: Left: z-modulated background defined by $\theta_0 = 20°$ and $\theta_L = 50°$. Right: y-modulated background with $\theta_{bot} = 10°$ and $\theta_{top} = 30°$.

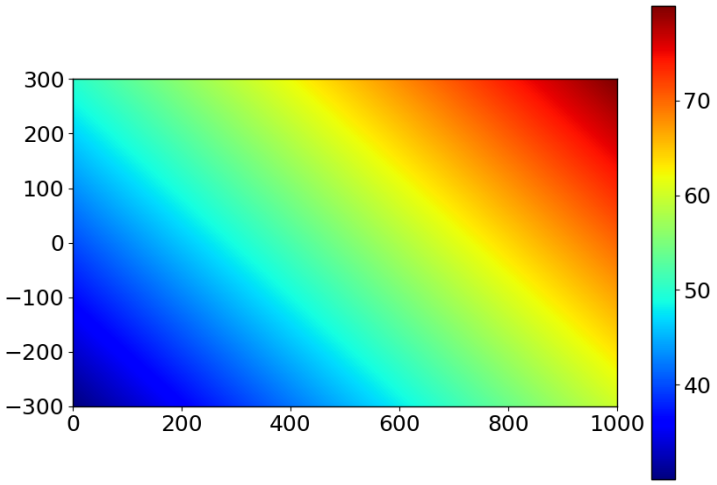


Figure 4.39: Background orientation obtained by combining the transverse and longitudinal modulation from the previous figure.

Notice that for the nematicon system (4.42) and (4.43) to remain valid in the weakly nonlinear regime considered, the values at the extreme corners of the sample NLC cell should be kept far from 0 or $\pi/2$, i.e. $\theta_0 - \theta_{bot} > 0$ and $\theta_L + \theta_{top} < \pi/2$.

Figure 4.40(a) and (b) compare respectively trajectories and profiles of FP and BP nematicons generated by identical input beams injected from the opposite ends of a $(30\mu m, 600\mu m, 1000\mu m)$ cell, with optical power $P_b = 2.45mW$ and width $W_b = 4.2\mu m$. The background orientation is given a mixed modulation (4.56) quantified by $\theta_0 = 20°$, $\theta_L = 50°$, $\theta_{bot} = 20°$ and $\theta_{top} = 10°$, using the "plus" sign in (4.56); Figure 4.40(b) displays well-separated FP and BP nematicon profiles on either side of the Gaussian input, with a transverse displacement $\Delta y \sim 50\mu m$ in $z = 0$, Fig 4.40(c)-(d) graphs the background walk-off and extraordinary refractive index across the sample at rest. The injected wavepackets experience self-focusing and self-routing at varying rates as they travel across regions with modulated refraction oriented at $\theta_0$ (for the FP beam) or $\theta_L$ (for the beam BP), with the walk-off and refractive index acting in a cooperative/counteracting way in different regions of the cell. Figure 4.41 presents results for $\theta_0 = 20°$, $\theta_L = 50°$, $\theta_{bot} = 10°$ and $\theta_{top} = 30°$, where the transverse component in Eq. (4.56) plays a significant role over the longitudinal one, resulting in well-separated FP and BP nematicons (c.f Figure 4.41 (b)).

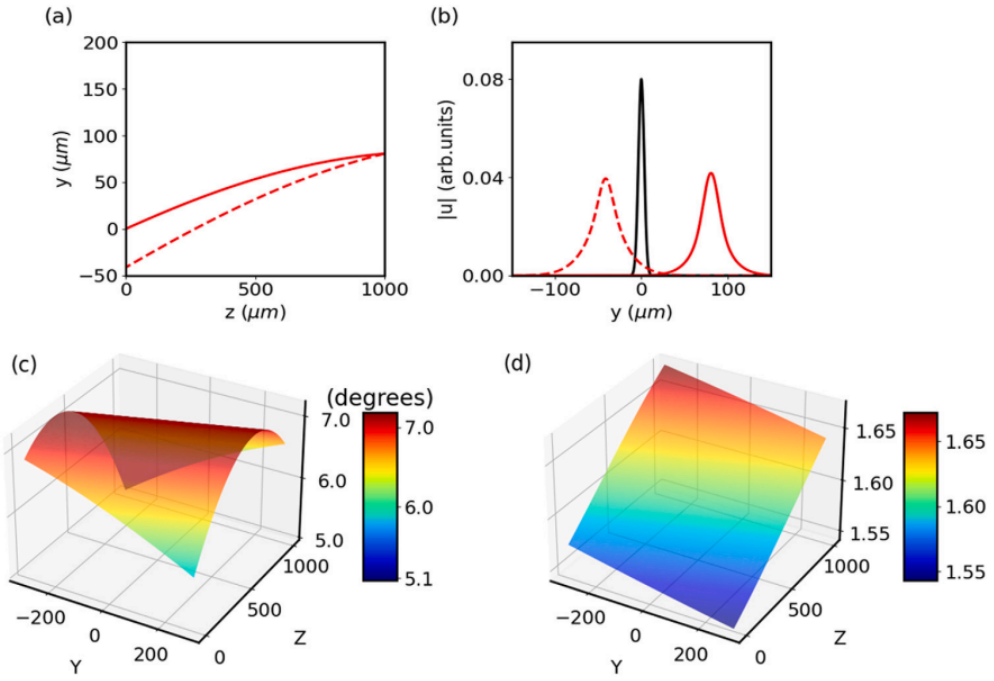


Figure 4.40: Diode-like response for $2.4mW$ input beams in a sample with $\theta_0 = 20°$, $\theta_L = 50°$, $\theta_{bot} = 20°$ and $\theta_{top} = 10°$. (a) FP(solid line) and BP (dashed line) nematicon trajectories in the principal plane $(y, z)$. (b) Transverse profiles of input beam (black), FP nematicon (red solid) in $z = L$, and BP nematicon in $z = 0$ (red dashed). (c)Linear walk-off $\delta(y, z)$ and (d) extraordinary refractive index $n_e(y, z)$ distributions across the cell. Reproduced with permission from [122]. Copyright by Elsevier.

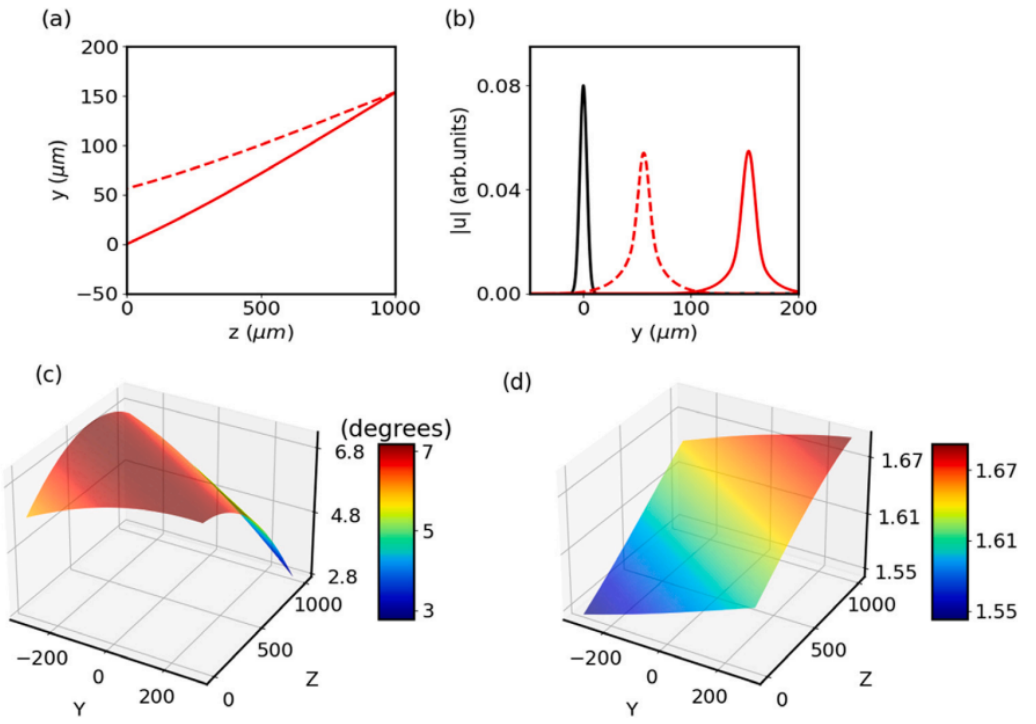


Figure 4.41: Diode-like response for $2.4mW$ input beams in a sample with $\theta_0 = 20°$, $\theta_L = 50°$, $\theta_{bot} = 10°$ and $\theta_{top} = 30°$. (a) FP(solid line) and BP (dashed line) nematicon trajectories in the principal plane $(y, z)$. (b) Transverse profiles of input beam (black), FP nematicon (red solid) in $z = L$, and BP nematicon in $z = 0$ (red dashed). (c)Linear walk-off $\delta(y, z)$ and (d) extraordinary refractive index $n_e(y, z)$ distributions across the cell. Reproduced with permission from [122]. Copyright by Elsevier.

## 4.8 (2+1)-D Model

We will now discuss, the corresponding adjustments to the numerical methods for the (2+1)-D model with a damping term (See Section 4.3.1)

$$i\frac{\partial u}{\partial z} + i\gamma\Delta(\theta_b + \psi)\frac{\partial u}{\partial y} + \frac{1}{2}\nabla_\perp^2 u + 2\frac{\sin(2\theta_b)}{\sin(2\theta_0)}\psi u + i\epsilon(y)u = 0, \tag{4.57}$$

$$\nabla_\perp^2\psi + \frac{2}{\nu}\frac{\sin(2\theta_b)}{\sin(2\theta_0)}|u|^2 = 0. \tag{4.58}$$

As with the (1+1)-D, we take the Fourier transform of the electric field equation (4.57)

$$\frac{\partial\hat{u}}{\partial z} + i\gamma\Delta(\psi)s_y\hat{u} - \frac{i}{2}s_x^2\hat{u} - \frac{i}{2}s_y^2\hat{u} - i\mathcal{F}\left\{2\frac{\sin(2\theta_b)}{\sin(2\theta_0)}\psi u\right\} + \mathcal{F}\{i\epsilon u\} = 0, \tag{4.59}$$

where $s_x$ and $s_y$ are the Fourier variables corresponding to the spatial variables $(x, y)$.

In equation (4.59) the terms $\Delta(\psi)$ and $\mathcal{F}\left\{2\frac{\sin(2\theta_b)}{\sin(2\theta_0)}\psi u\right\}$ require the computation of $\psi$ from the director equation (4.58) with $\psi = 0$ at the boundaries $x = \pm L_x/2$, $Y = \pm L_y/2$. Several approaches can be used to associate the Poisson Equation with boundary conditions. For example, taking FFT of (4.58) in the $x$ direction reduces the problem to a two-point boundary value problem in $y$

$$\frac{d^2\hat{\psi}}{dy^2} = s_x^2\hat{\psi} - \frac{2}{\nu}\mathcal{F}\left\{\frac{\sin(2\theta_b)}{\sin(2\theta_0)}|u|^2\right\}, \quad \psi(\pm L_y/2) = 0. \tag{4.60}$$

Here we can use finite difference combined with Picard iteration to obtain the system

$$\hat{\psi}_{i+1} - 2\hat{\psi}_i + \hat{\psi}_{i-1} = (\Delta y)^2 s_x^2\hat{\psi} + (\Delta y)^2 f(\hat{\psi}), \tag{4.61}$$

where $f$ includes all the nonlinear terms and $\Delta y$ is the spatial step in the $y$ direction. This system can be written in matrix form

$$A\hat{\psi} = b. \tag{4.62}$$

And given an initial guess $\hat{\psi}_0$ for $\hat{\psi}$, we can iterate $A\hat{\psi_{i+1}} = b(\hat{\psi}_i)$ until $\hat{\psi}_i$ converges.

However, this approach has several drawbacks when compared with other methods such as Jacobi iteration or Gauss-Seidel [95], in particular, the high amount of computational memory required makes it impractical for large numerical grids.

For those reasons, we choose to employ the Gauss-Seidel method, which has a faster convergence rate and requires fewer iterations than Jacobi iteration and less computational memory. In this case, the Poisson equation (4.58) is iterated as

$$\psi_{i,j}^{k+1} = \frac{(\psi_{i-1,j}^{k+1} + \psi_{i+1,j}^{k})\Delta y^2 + (\psi_{i,j+1}^{k} + \psi_{i,j-1}^{k+1})\Delta x^2 - \Delta x^2\Delta y^2 f_{i,j}}{2(\Delta x^2 + \Delta y^2)}, \tag{4.63}$$

where $\Delta x$ and $\Delta y$ are the spatial steps in the $x-$ and $y-$ respectively . Then, we measure the difference in norm between $\psi^{k+1}$ and $\psi^k$ until the difference is smaller than a fixed tolerance (typically $10^{-5}$). The Gauss-Seidel method can be improved using numerical techniques, such as successive over-relaxation, but is the bottleneck on computational time for the nematicon system [15], as mentioned in Section 4.3.1 the nematicon system (4.57) and (4.58) takes around 10000 minutes to be solved using Gauss-Seidel, for propagation lengths of 1000µm in a single Intel Xeon E5-2680 at 2.5 GHz.

On the other hand, the electric field equation (4.59) can be solved using the same integrating factor method from the (1+1)-D model, namely

$$\frac{d}{dz}\left(\hat{u}_{i,j}e^{i(s_i^2+s_j^2)z/2}\right) = -i\mathcal{F}\{NON(u_{i,j},\psi_{i,j})\}e^{i(s_i^2+s_j^2)z/2}, \tag{4.64}$$

where $NON$ includes the nonlinear terms and

$$s_i = \frac{2\pi i}{L_x}, \qquad s_j = \frac{2\pi j}{L_y}, \tag{4.65}$$

$$i = \frac{-N_x}{2} + 1, \ldots, \frac{N_x}{2}, \quad j = \frac{-N_y}{2} + 1, \ldots, \frac{N_y}{2}, \tag{4.66}$$

with $N_x$ and $N_y$ the number of discretization points in the spatial directions. In a similar fashion to the (1+1)-D model, (4.64) can be solved using the RK4 method in Fourier space and the final solution is obtained via the inverse FFT algorithm to return to physical space.

To summarize, the spatial domain $\left[-\frac{L_x}{2}, \frac{L_x}{2}\right] \times \left[-\frac{L_y}{2}, \frac{L_y}{2}\right]$ is discretized in a $i \times j$ grid, with $i, j$ given by (4.66). The propagation length $[0, L_z]$ (time-like domain) is also uniformly discretized into $N_z$ points, such that $z_k = k\Delta z$, $k \in \{0, \ldots, N_z\}$, $\Delta z = L/N_z$.

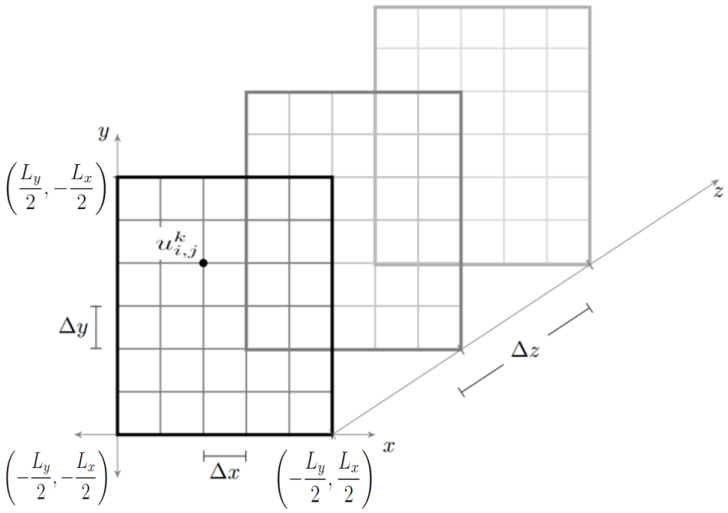


Figure 4.42: Diagram of the discretized NLC cell. The point $u^k_{i,j}$ represents the point $u(x_i, y_j, z_k)$ on the grid.

First, initial conditions are applied to the system. The all-optical reorientational angle $\psi$ is uniformly set equal to zero over the $(x, y)$, i.e. $\psi^0_{i,j} = 0$. The electric field envelope for the light beam $u$ is set to an input Gaussian beam profile

$$u^0_{i,j} = A_b \exp\left(\frac{x_i^2 + y_j^2}{W_b^2}\right), \quad xi = i\Delta x, y_j = j\Delta j, \tag{4.67}$$

where $A_b$ and $W_b$ are the nondimensional amplitude and width of the beam, respectively.Then, $u^0 i, j$ is used to determine the distribution of the reorientational $\psi^1_{i,j}$ at $z = \Delta z$ from the discretized Poisson equation (4.63).

The angle $\psi^1_{i,j}$ is used in the discretized electric field equation (4.64) to propagate the solutions one time step $\Delta z$ and obtain $u^1_{i,j} = u(i, j, \Delta z)$. The process

is iterated until we obtain $u_{i,j}^{N_z} = u(i, j, L_z)$, the solution at $z = L_z$.

Finally, the position of the beam centre at $z = L$ is taken as the input position for the initial Gaussian BP beam, and the previous steps are repeated after reversing the wave vector i.e. changing $z$ by $-z$ in the electric field equation.

| Typical Numerical Parameter | | |
|---|---|---|
| Symbol | Parameter | Value |
| $N_x$ | Number of spatial modes $x$ direction | 128 |
| $D_x$ | Nondimensional spatial $x$ interval | 62 |
| $\Delta x$ | Spatial $x$ sampling rate | 0.4 |
| $N_y$ | Number of spatial modes $y$ direction | 2048 |
| $D_y$ | Nondimensional spatial $y$ interval | 1250 |
| $\Delta y$ | Spatial $y$ sampling rate | 0.6 |
| $N_z$ | Number of time-like steps | 189000 |
| $L$ | Nondimensional propagation interval | 948 |
| $\Delta z$ | Time-like step | 0.005 |
| $A_b$ | Nondimensional amplitude | $0.9 \rightarrow 0.18$ |
| $W_b$ | Nondimensional width | $8 \rightarrow 15$ |
| $\gamma_0$ | Strength of the damping layer | 40 |
| $1/\eta$ | Width of the damping layer | 1 |
| $\nu$ | Nonlocality parameter | 250 |
| $\alpha$ | Nondimensional loss coefficient | 0.001 |

Table 4.2: Typical numerical parameters for the (2+1)-D linear longitudinal modulation problem.

### 4.8.1 Results (2+1)-D Model

Due to the large computational times of the (2+1)-D model, few numerical experiments were realized. Figures 4.43 and 4.44 display the results of (2+1)-D numerical simulation in a $z$-modulated sample cell governed by equations (4.57) and (4.58) for an input beam of power $P_b = 8.5mW$ and width $W_b = 4.2mW$, with a background modulation defined by $\theta_0 = 45°$ and $\theta_L = 80°$. The nonlocality is given by $\nu = 250$.

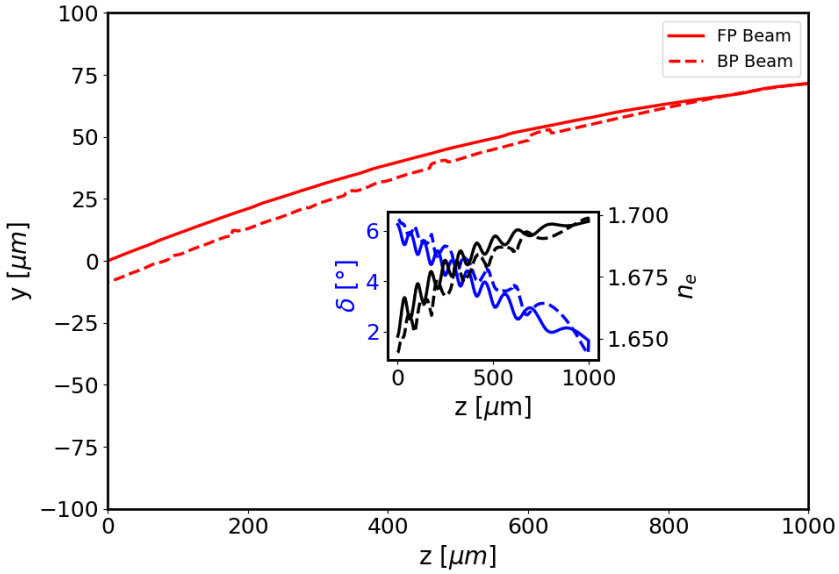


Figure 4.43: Diode-like response for $8.5mW$ input beams and $\theta_0 = 45°$,$\theta_L = 80°$. FP (solid line) and BP (dashed line) beam trajectories in $(y, z)$. Inset: Nonlinear walk-off angle $\delta$(blue lines) and extraordinary refractive index $n_e$ (black lines), oscillations are due to oscillations in the amplitude of the electric field [124].

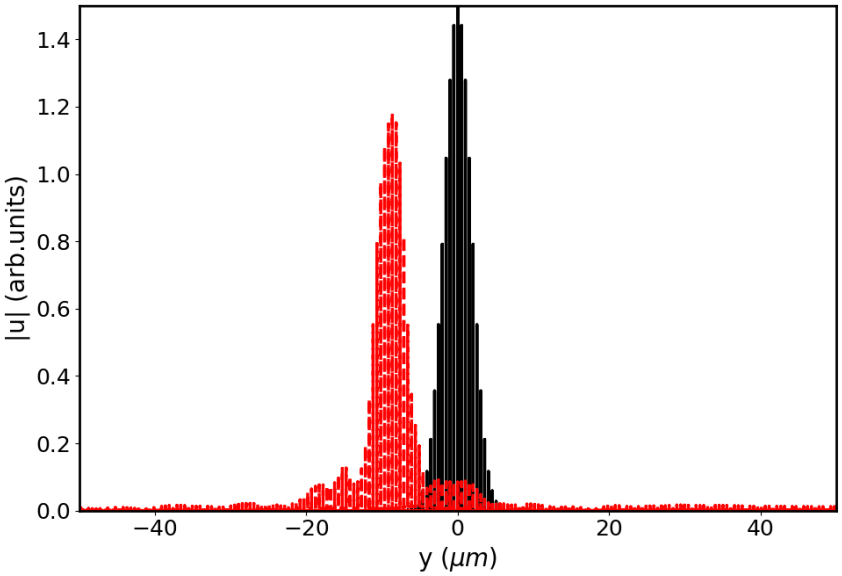


Figure 4.44: Transverse section of the input beam (black bars) and BP beam (red bars) profiles for parameters of Table 4.2.

We observe a diode-like response with separated solitary beam peaks at $z = 0$, although the transverse separation $y_{BP}(z = 0) - y_{FP}(z = 0)$ is around half of the separation observed in the (1+1)-D model. As expected, the optical power necessary to sustain nematicon propagation along the whole length of the cell is higher than in the reduced model, and a power-dependent threshold exists with

beams of lower power experiencing diffraction or breaking down into filaments. We expect scattering losses to play a significant role as the thickness of the sample cell is no longer negligible and nonlocality is crucial to stabilize two-dimensional solitary waves in NLS-type equations [171].

## 4.9 Results For Additional Configurations

### 4.9.1 Asymmetric $z$-modulated sample cells

We consider an asymmetric background $z$-modulation obtained by combining two linear orientations with different slopes, namely

$$\theta_b(z) = \begin{cases} \theta_0 + \left(\frac{\theta_1-\theta_0}{L/2}\right) z, & z \leq L/2, \\ \theta_2 + \left(\frac{\theta_0-\theta_2}{L/2}\right) z, & z > L/2. \end{cases} \tag{4.68}$$

where $\theta_1 \neq \theta_2$ and the angle at the ends of the cell is $\theta_0 = \theta_b(z=0) = \theta_b(z=L)$. Figures 4.45, 4.46 and 4.47 display the results obtained for an input beam of dimensional power $P_b = 2.4\ mW$, width $W_b = 4.2\ \mu m$. The nonlocality is given by $\nu = 250$ and the background modulation defined by $\theta_0 = 10^\circ$, $\theta_1 = 41^\circ$ and $\theta_L = 55^\circ$.

Figure 4.46(a) displays well-separated FP and BP nematicons profiles compared with the Gaussian input, with a transverse displacement $y_{BP}(z=0) - y_{FP}(z=0) \approx 30\mu m$ at $z=0$ consistent with a diode-like response where negligible amounts of crosstalk between the BP output and the FP port.

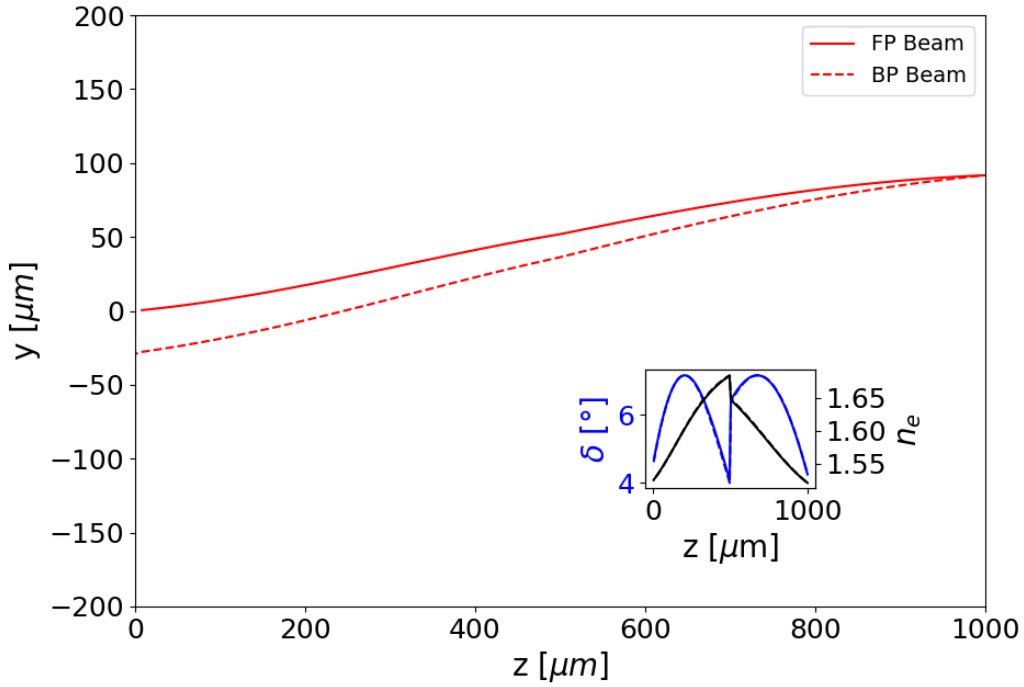


Figure 4.45: Beam trajectory in an asymmetric modulated cell for an input beam of dimensional power $P_b = 2.4\ mW$, width $W_b = 4.2\ \mu m$. The nonlocality is given by $\nu = 250$ and the background modulation defined by $\theta_0 = 10°$, $\theta_1 = 41°$ and $\theta_2 = 55°$. Inset: Computed linear walk-off $\delta$ (blue) and extraordinary refractive index $n_e$ (black)

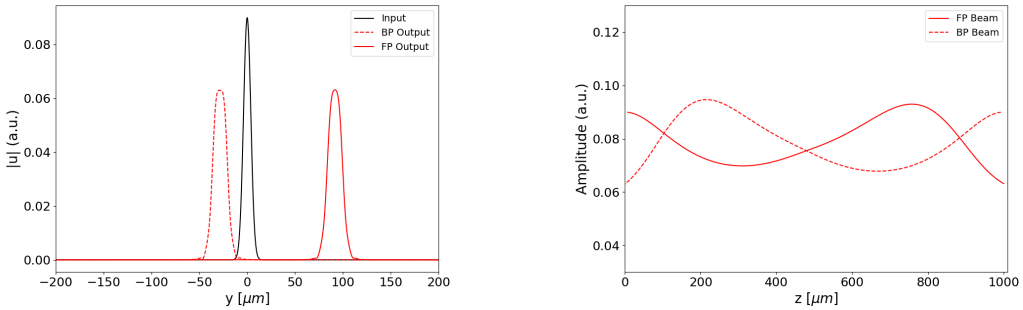


Figure 4.46: (a) Transverse profiles of input beam (black), FP beam at $z = L$ (red solid line), BP beam at $z = 0$. (b) dimensionless amplitudes of FP(solid line) and BP (dashed line) beams

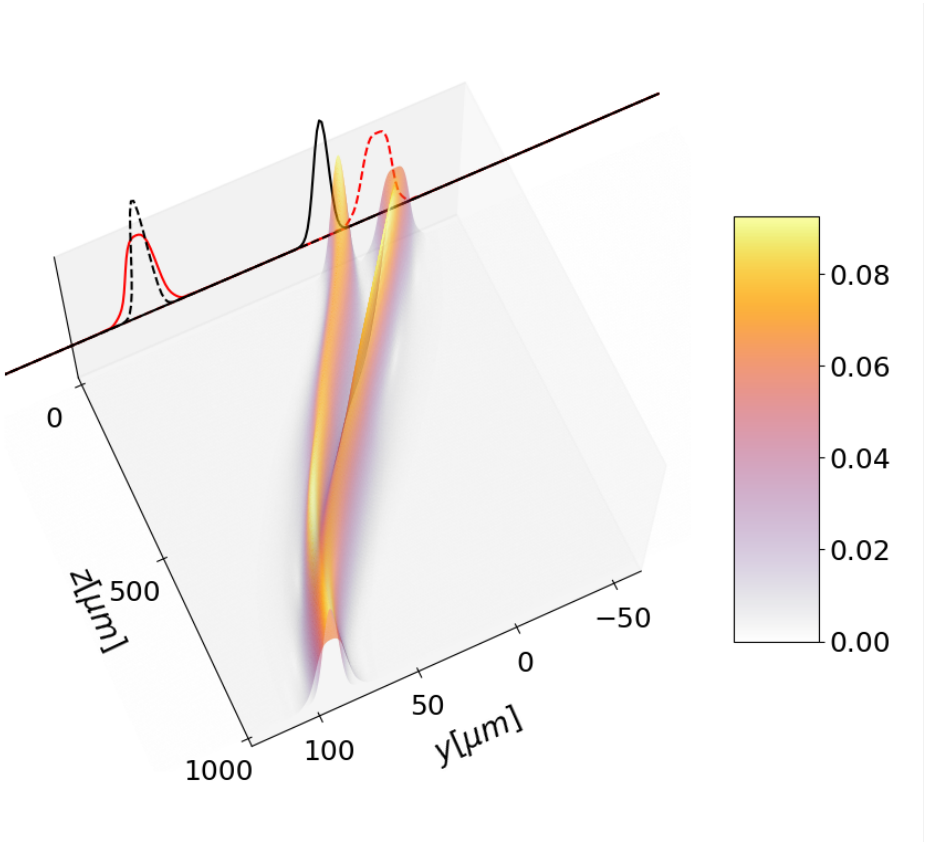


Figure 4.47: 3D trajectories and transverse profiles of FP (green arrow) and BP (red arrow) nematicons (normalized field amplitude $u$ in arbitrary units); input (black) and output (red) beam profiles in $z = 0$,$z = L$ are also projected on the $y$ axis in $z = 0$.

### 4.9.2 Sample cells with asymmetric scattering losses

We also consider a $z$-modulated sample cell where scattering losses $\alpha$ are present only in half of the sample, i.e.

$$\alpha = \begin{cases} 0, & z \leq L/2, \\ \alpha, & z > L/2. \end{cases} \tag{4.69}$$

Figures 4.48, 4.49 and 4.50 show the results obtained for an input beam of dimensional power $P_b = 2.4\ mW$, width $W_b = 4.2\ \mu m$. The nonlocality is given by $\nu = 250$ and the background modulation defined by $\theta_0 = 20°$ and $\theta_L = 60°$.

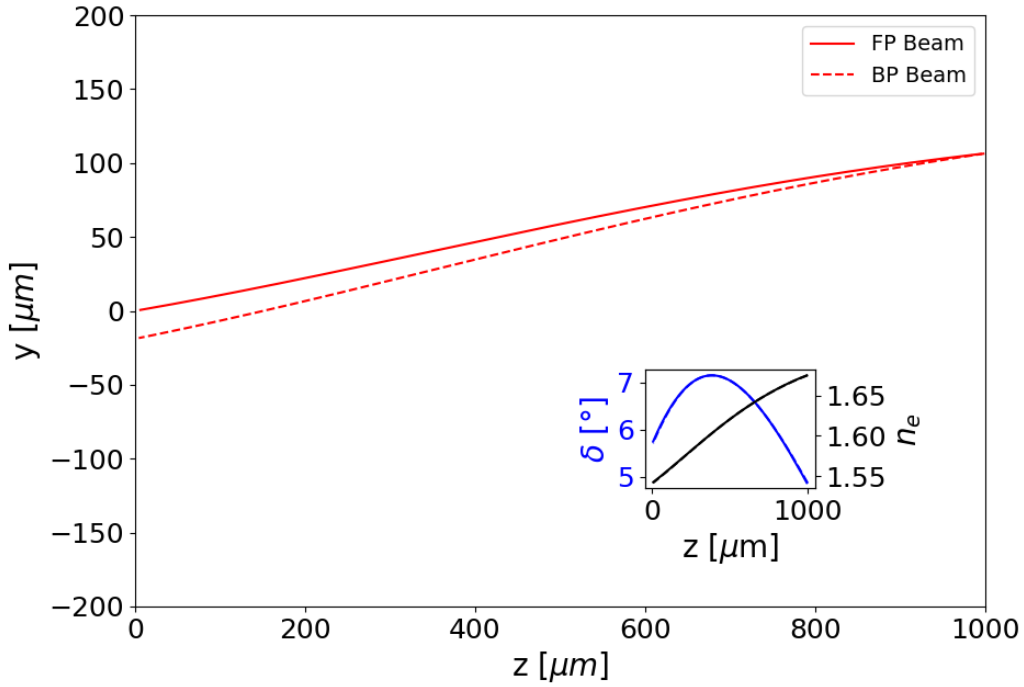


Figure 4.48: Beam trajectory in an asymmetric modulated cell for an input beam of dimensional power $P_b = 2.4\ mW$, width $W_b = 4.2\ \mu m$. The nonlocality is given by $\nu = 250$ and the background modulation defined by $\theta_0 = 20°$ and $\theta_L = 60°$. Inset: Computed linear walk-off $\delta$ (blue) and extraordinary refractive index $n_e$ (black)

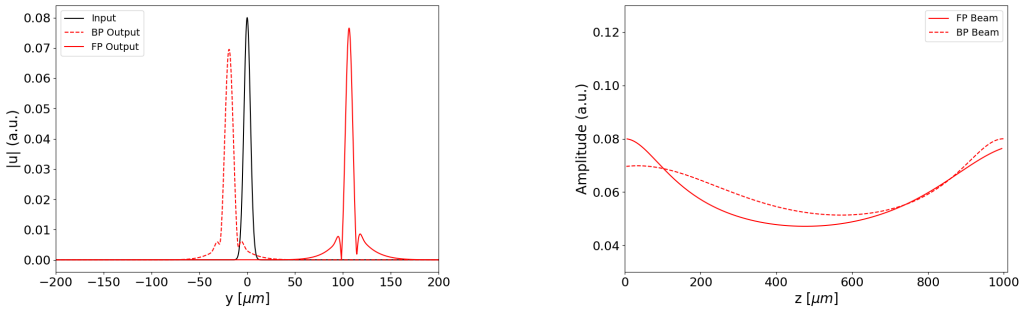


Figure 4.49: (a) Transverse profiles of input beam (black), FP beam at $z = L$ (red solid line), BP beam at $z = 0$. (b) dimensionless amplitudes of FP(solid line) and BP (dashed line) beams

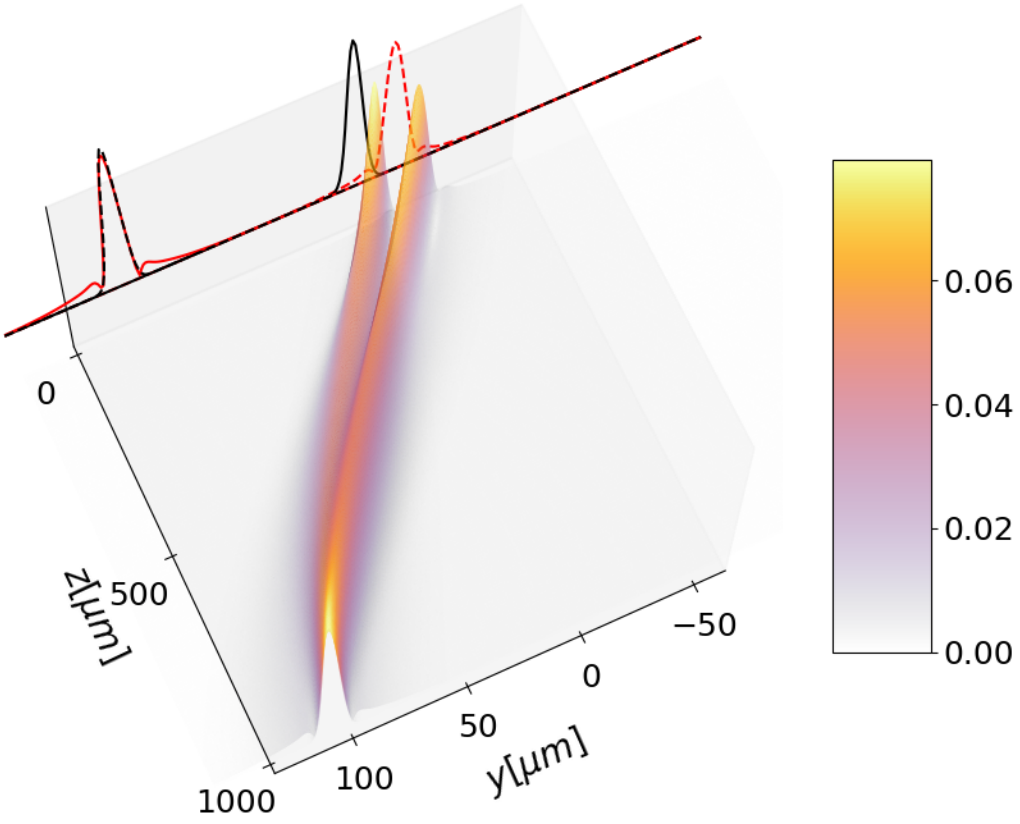


Figure 4.50: 3D trajectories and transverse profiles of FP (green arrow) and BP (red arrow) nematicons (normalized field amplitude $u$ in arbitrary units); input (black) and output (red) beam profiles in $z = 0$,$z = L$ are also projected on the $y$ axis in $z = 0$.

Figure 4.49(a) displays well-separated FP and BP nematicons profiles compared with the Gaussian input, with a transverse displacement $y_{BP}(z = 0) - y_{FP}(z = 0) \approx 20\mu m$ at $z = 0$ consistent with a diode-like response where negligible amounts of crosstalk between the BP output and the FP port. However, 4.49 (b) and 4.50 show that the presence of losses in half of the cell reduces the nematicons amplitude significantly, increasing the amount of radiation shed as they pass into the loss region $z > L/2$.

# Chapter 5

# Optical Isolation, Time Symmetry Breaking and Dynamic Reciprocity

## 5.1 Optical diode effect and direction-dependent routing

The simple layout examined in Sections 4.6, 4.6 and 4.7 can be regarded as a two-port guided wave device, in which forward and backward extraordinary polarized signals are confined in the nematicon waveguides excited by counterpropagating beams of equal powers and profiles. In this respect, since the BP nematicon is not superposed with the FP nematicon, the resulting optical device displays an all-optical diode-like transmission, with low signal crosstalk and high rejection depending on the separation, as $\Delta y > W_b$, and adjustable with the optical power and background orientation angle parameters. Moreover, in the scattering matrix formalism (c.f. Section 2.3.3) the device can be described by the following isolator-like scattering matrix

$$S_{\text{device}} = \begin{bmatrix} 0 & b \\ a & 0 \end{bmatrix}, \tag{5.1}$$

where $b \ll 1$ is the output of the BP beam at port 1 ($z = 0$) and $a \leq 1$ is the output of the FP beam at port 2 ($z = L$).

Since the phenomenon rests essentially on the nonspecular distribution $\Theta$ of the optical axis with respect to the input and output ports, a modulated NLC sample can be described as a dielectric stack (c.f [126] and references therein) resulting in a spatially asymmetric dielectric tensor $\epsilon(\vec{r})$. The previous consideration supports the claim of nonreciprocal transmission despite the passive and nonmagnetic character of the device. Nevertheless, the concepts of nonreciprocity, time-reversal breaking and asymmetrical transmission are often used interchangeably and their definitions have generated widespread confusion and discussion [31, 127, 128, 129, 130, 131]. It is then natural to ask ourselves: Is the observed asymmetrical transmission truly proof of optical nonreciprocity?

## 5.2 Nonreciprocal Systems

In physics, a nonreciprocal system can be described as one that exhibits different received/transmitted field ratios when sources and detectors are exchanged [126, 132]. Nonreciprocal systems may be classified into linear and nonlinear, with linear isolators corresponding to devices whose responses are independent of the amplitude of the input signal [131, 132]. In both instances, nonreciprocity is based on time-reversal symmetry breaking, through an external bias in the linear case, or via a combination of self-biasing and structural asymmetry [132, 133, 126] in the nonlinear one.

### 5.2.1 Time-reversal operation

The time reversal operation can be described by monitoring the temporal evolution of a process between two ports $P_1$ and $P_2$. First, we excite $P_1$ at $t = 0$ and trace the response of the system until transmission to $P_2$ at $t = T$. Then, flipping the sign of the time variable, results in a system, that is not necessarily identical to the original one, being excited at $t = -T$ and evolving until the time $t = 0$ where the response at port $P_1$ is obtained. If the system does not remain the same under time-reversal, we call it *time-reversal asymmetric* [132]. Equivalently, a system is time-reversal asymmetric if it exhibits a different response when transmitting at $P_1$ and receiving at $P_2$ as than when transmitting at $P_2$ and receiving at $P_1$.

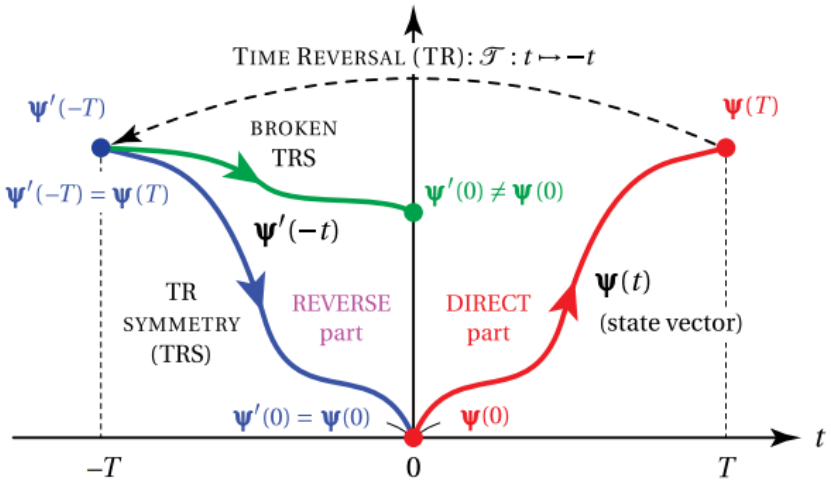


Figure 5.1: Time-reversal symmetry (red and blue curves) and broken time-symmetry. Here $\Psi(t)$ corresponds to the state vector of the system, consisting of magnitude, phase, temporal and spatial frequency, polarization, momentum, and spin. Image reproduced from [132].

In our direction-dependent routing problem, the propagation length $z$ takes the role of a time-like variable and we excite a nematicon waveguide that trans-

mits a signal from port 1 at $z = 0$ until it is received at port 2 at $z = L$. After time-reversal ($z-$ reversal in our problem) the nematicon waveguide excited from port 2 transmits a signal that is not fully received at port 1, effectively breaking time-reversal symmetry.

Time-reversal asymmetry provides a fundamental criterion for nonreciprocity. As stated in [172], inverting the sign (direction) of the input (beam/signal) wavevector and interchanging the locations of source and detector does not leave the system transmission unchanged, enabling the attribution of nonreciprocity to our two-port device given by the FP and BP extraordinary-wave guided signals. However, this has been considered by some [126, 132] a loose criterion, as there are systems that exhibit time-reversal breaking despite being reciprocal [132].

### 5.2.2 Optical Isolation

An optical isolator is a nonreciprocal device that allows light signals to propagate in one direction but suppresses the transmission of arbitrary waves in the backward direction. An ideal optical isolator has to block or divert all possible signals excited for backward transmission and, therefore, it is not enough to find a configuration with a good transmission in the forward direction and another with a poor transmission in the backward direction. A true optical isolator blocks backwards transmission for all possible states of backward propagation [31]

In practical conditions, the previous restrictions can be relaxed depending on the operation modes and power range of the photonic devices involved. A simple experimental test to verify optical isolation under practica conditions was proposed by Jalas et al[31] and is displayed in Fig. 5.2. First, input and output signals should be reduced to single modes and the difference between forward and backward transmission measured without adjusting the set-up between input and output. To ensure that the setup does not influence the result, all transmission factors are normalized by performing a measurement when the potential optical isolator is bypassed.

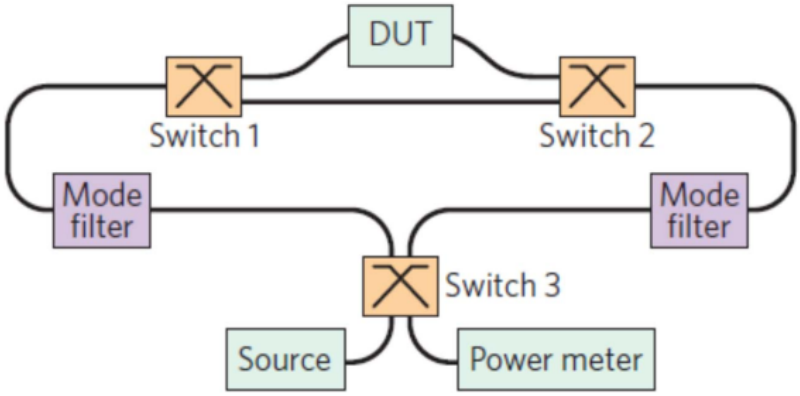


Figure 5.2: Experimental set-up for verifying optical isolation of a device under test (DUT) proposed by Jalas et al. Image reproduced from [31].

For our two-port device the test proceeds as follows:

1. A source Gaussian beam is launched into a single-mode optical fibre connected to port 1 on the left side of the diagram in Figure 5.2 and to port 2 on the right side.

2. Switches 1 and 2 are active to bypass our modulated liquid crystal cell.

3. The optical power of the signal is measured at the power meter for both states of switch 3 (One corresponds to the Forward propagating (FP) beam and the other to the Backward propagating (BP) beam, we denoted the measurements by $P^{FP}_{\text{bypass}}$ and $P^{BP}_{\text{bypass}}$.

4. Activate switches 1 and 2 to go through the cell and measure the transmitted powers for both states of switch 3, denoting the measurements by $P^{FP}_{\text{device}}$ and $P^{BP}_{\text{device}}$

5. If $\frac{P^{FP}_{\text{device}}}{P^{FP}_{\text{bypass}}} \neq \frac{P^{BP}_{\text{device}}}{P^{BP}_{\text{bypass}}}$, then isolation is observed between ports 1 and 2.

Our two-port device then displays isolator-like behaviour, with Figure 5.3 displaying the corresponding scheme. The extraordinary-polarized guided-wave signals transmitted along the nematicon waveguide do not overlap when launched in opposite directions from the input FP port at $z = 0$ and from the output port at $z = L$, respectively. Moreover, the nematicon mode is the only one operating in the system.

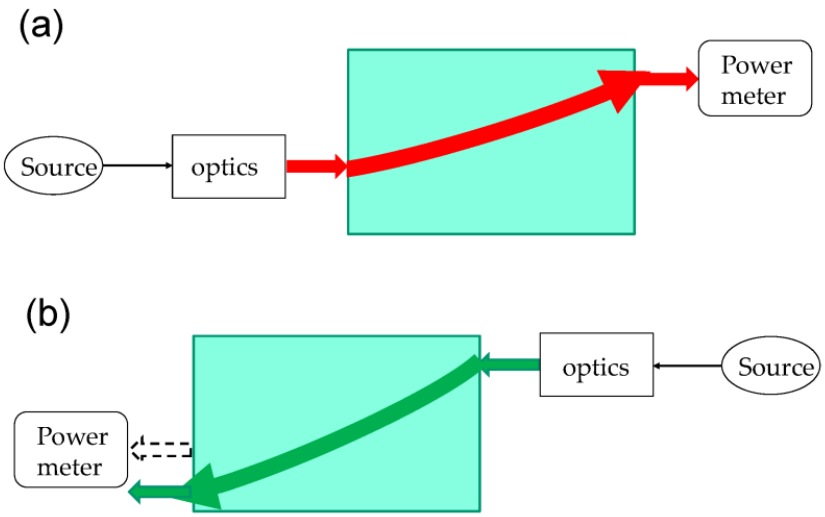


Figure 5.3: Diode operation: (a) FP nematicon and guided-wave co-polarized signal travel from left to right, reaching the light meter: (b) BP nematicon and co-polarized signal travel from right to left using the same FP output port, but do not reach the detector, despite identical beam excitation with $\vec{k}_{FP} = -\vec{k}_{BP}$. Reproduced with permission from Photonics.

Now, this diode corresponds to a passive nonlinear structure, as the optical solitons and their paths are power-dependent. Also, it operates in a non-simultaneous fashion, hence, it should be considered if it can be constrained by *dynamic reciprocity* [131].

### 5.2.3 Phase-conjugation

In optics, particularly, nonreciprocity has been extensively discussed with reference to linear systems, but it remains somewhat debated when addressing those with nonlinear and/or dissipative responses [126]. According to de Hoop's work [133], the inherent nonlinearity entails the non-reciprocal operation of inhomogeneous non-magnetic nematic liquid crystals, which resemble dielectric stacks with a spatially nonsymmetric dielectric tensor [126, 133], as in our geometry entailing orientation modulation across the transverse coordinate ($y$) (Section 4.6).

A stronger test for reciprocity is to consider time-reversal with phase-conjugation [126], used to generalise Lorentz (non)reciprocity theorem [126]. The phase-conjugation operation can be expressed as:

$$T : u \to u^*, \qquad \vec{k} \to -\vec{k}$$

This pair of operations, conjugation of complex amplitudes and inversion of wavevectors, reverses the sign of the Poynting vector, i.e. the time-reversal operator $T$ reverse the direction of the energy flow provided, that, at the same time as reversing $\vec{k}$, the complex amplitude is conjugated. It is important to note that following Potton's argument reciprocity is not the same as time-reversal

symmetry or phase conjugation the same as time-reversal (See Carminatti [134]), but along two planes($z = 0$ and $z = L$) phase-conjugation can achieve complete time-reversal of a field (Section D in Carminatti). Nonetheless, authors (See [135],[136]) use optical phase conjugation as their means to achieve reciprocity

We performed numerical experiments by launching a BP input which was a (reflected) phase-conjugated replica of the FP outgoing beam at the output FP port $y_{FP}(L)$. See Figures 5.4, 5.5, 5.6 and 5.7 for the phase-conjugated results corresponding to the systems from Sections 4.5, 4.6 and 4.7.

Under this test, our layout appears to be weakly nonreciprocal (see Table 1 in [132]), as it remains reciprocal under the strong phase-conjugation criterion. Nevertheless, in view of potential applications, the examined configurations of Sections 4.5, 4.6 and 4.7 display a strong diode-like effect. Thus, the confinement of co-polarized signals allows the two-port device, with input/output in $(y_{FP}(0), 0)$ and $(y_{FP}(L), L)$, to operate as a nonlinear diode which transmits forward to port 2 $(y_{FP}(L), L)$ signals injected in port 1 $(y_{FP}(0), 0)$ , while it isolates port 1 from signals back-launched in port 2.

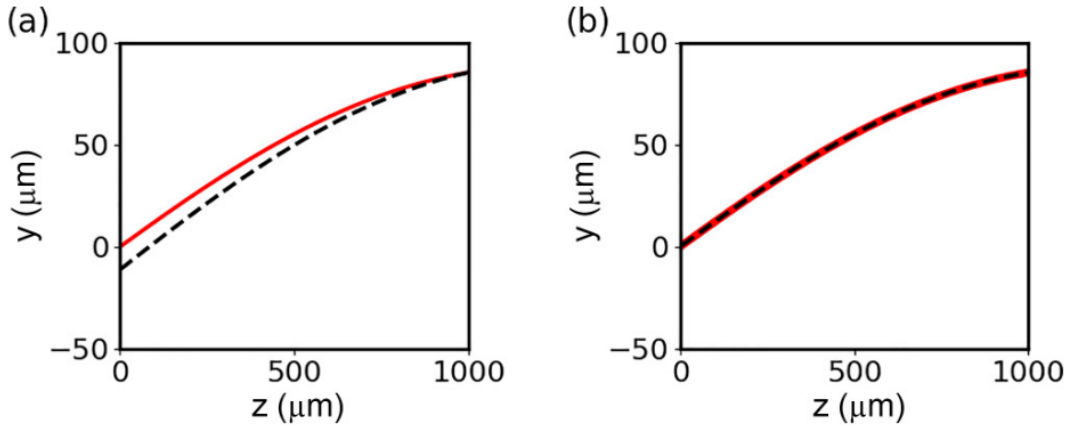


Figure 5.4: Linear longitudinal modulation in a sample with $\theta_0 = 45°$ and $\theta_L = 70°$. The FP (red solid) and BP (black dashed) trajectories are plotted for (a) identical counter-launched input beam beams and (b) phase-conjugated reflection.

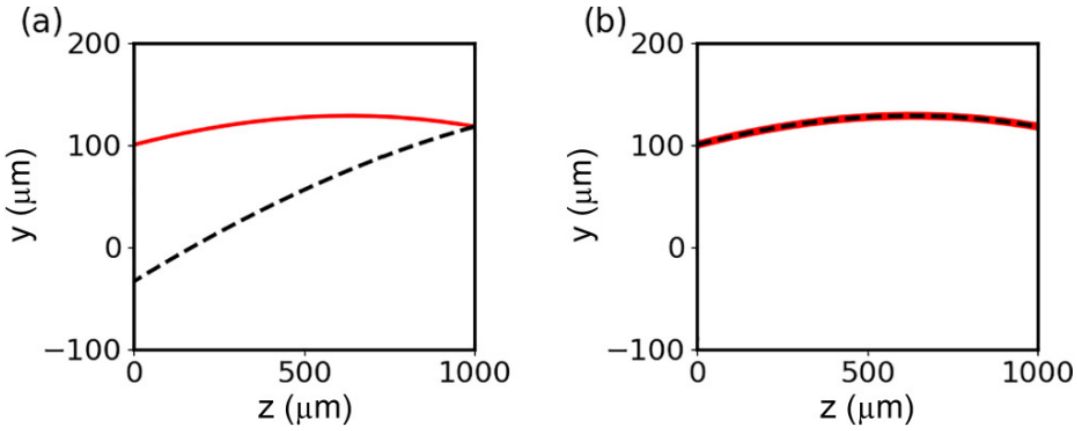


Figure 5.5: Linear transverse modulation in a sample with $\theta_{bot} = 75°$ and $\theta_{top} = 45°$. The FP (red solid) and BP (black dashed) trajectories are plotted for (a) identical counter-launched input beam beams and (b) phase-conjugated reflection.

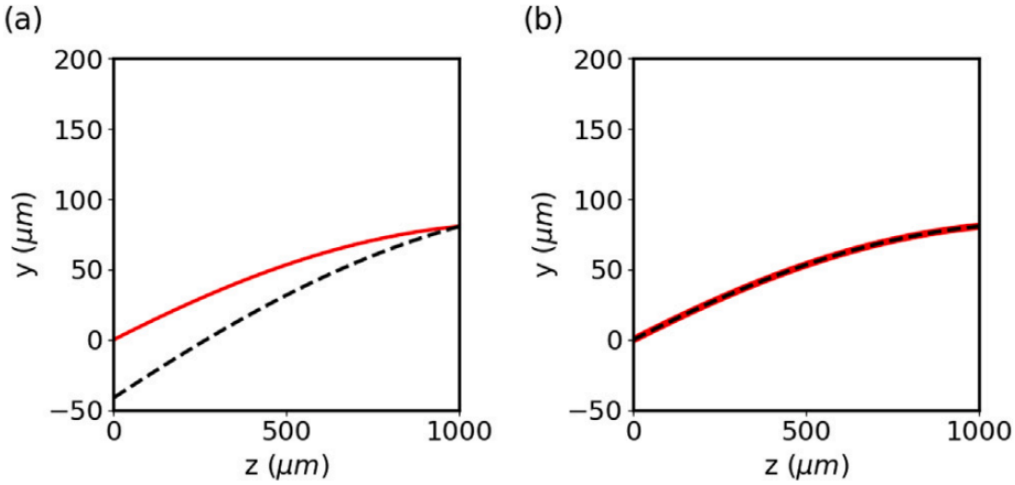


Figure 5.6: Sample with $\theta_0 = 20°$, $\theta_L = 50°$, $\theta_{bot} = 20°$ and $\theta_{top} = 10°$.The FP (red solid) and BP (black dashed) trajectories are plotted for (a) identical counter-launched input beam beams and (b) phase-conjugated reflection.

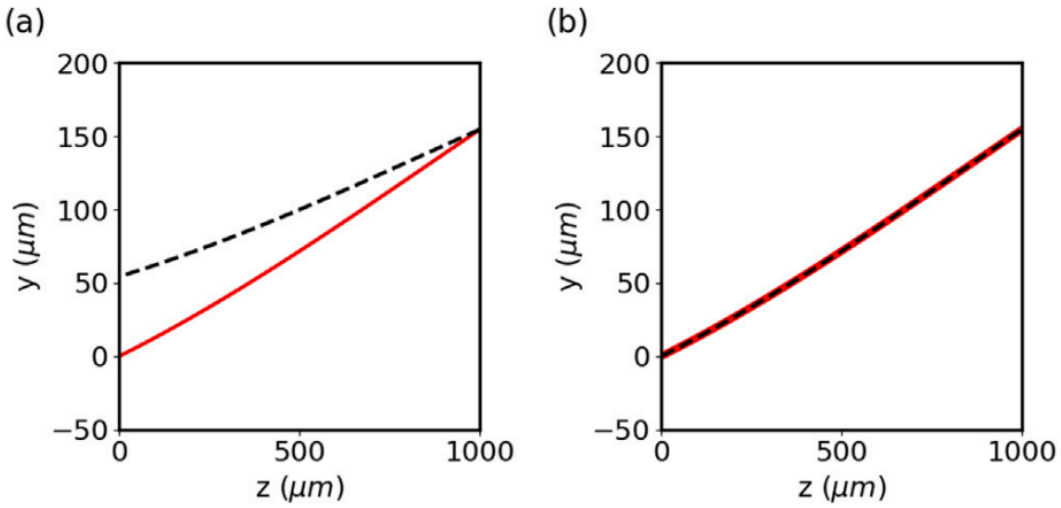


Figure 5.7: Sample with $\theta_0 = 20°$, $\theta_L = 50°$, $\theta_{bot} = 10°$ and $\theta_{top} = 30°$.The FP (red solid) and BP (black dashed) trajectories are plotted for (a) identical counter-launched input beam beams and (b) phase-conjugated reflection.

This result is not surprising if we observe the electric field equation (4.11) for the BP light beam,

$$-i\frac{\partial u}{\partial Z} + i\gamma\Delta(\theta_b(L-Z)+\psi)\frac{\partial u}{\partial Y} + \frac{1}{2}\frac{\partial^2 u}{\partial Y^2} + 2\frac{\sin(2\theta_b(L-Z))}{\sin(2\theta_b(L))}\psi u = 0. \quad (5.2)$$

Now, taking the complex conjugate of the equation we get,

$$i\frac{\partial u^*}{\partial Z} - i\gamma\Delta(\theta_b(L-Z)+\psi)\frac{\partial u^*}{\partial Y} + \frac{1}{2}\frac{\partial^2 u^*}{\partial Y^2} + 2\frac{\sin(2\theta_b(L-Z))}{\sin(2\theta_b(L))}\psi u^* = 0, \quad (5.3)$$

the phase-conjugate reflection $u^*(Y, L-Z)$ satisfies the FP beam equation with the sign of the walk-off term $\Delta$ flipped as the propagation variable is decreasing now.

### 5.2.4 Nonlinear isolators and Dynamic Reciprocity

In contrast to linear isolators, nonlinear ones break Lorentz reciprocity through the presence of a spatial nonlinearity. Such devices have a spatially asymmetric permittivity profile $\epsilon(\vec{r})$, therefore optical fields concentrate differently for FP and BP wavepackets, in other words, FP and BP beams encounter different dielectric structures as they travel across the device, displaying nonreciprocal behaviour. Moreover, the asymmetry between the dielectric structures encountered by FP and BP signals is a consequence of the signals themselves, in other words, as the FP and BP signals excite different field distributions within the device, this gives forms to different transmission properties. This opens the possibility to design devices that exhibit high transmission for an FP signal, but maintain low transmission for a BP signal within a certain optical power range [83, 131, 132].

Figure 5.8 sketches schematically the operating principle of a nonlinear optical isolator.

This is exactly the case for our two-port nematicon-based device, as, without the presence of the power-dependent nonlinearity given by the all-optical reorientation $\psi$, the system is reciprocal (c.f. Figure 4.12). When the nonlinearity is introduced, the dielectric properties of the spatially modulated NLC sample cell now depend on the strength of the optical field. As a result, the system exhibits high transmission between port 1 and port 2 for an input FP signal with sufficiently high power (c.f. Figure 4.13), while maintaining low transmission for BP waves between the same two ports.

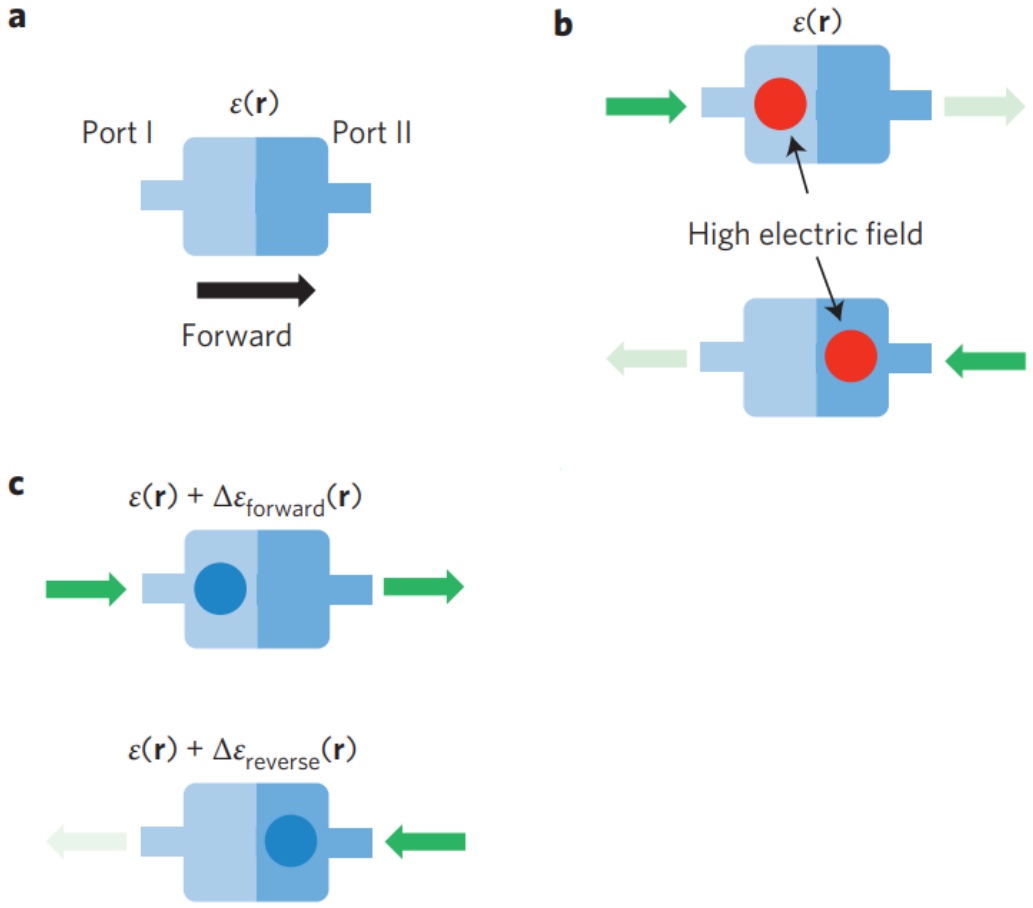


Figure 5.8: (a)General Two-port optical device with spatially asymmetric dielectric tensor $\epsilon(\vec{r})$. (b) Without nonlinearity, the system is reciprocal, as an FP input beam has the same transmission coefficients than a BP beam. (c) With nonlinearity, FP and BP signals travel through different dielectric structures: In the forward direction, the permittivity distribution is favourable to transmission, but in the reverse direction the dielectric structure of the device is not favourable for transmission. Adapted from [131].

In most experiments, and proposed optical devices based on nonlinear isolators one has either forward or backward waves, but not both. Under such conditions, nonreciprocity is demonstrated by launching an input wave between a particular power range and observing high transmission in the forward direction and low transmission in the backward direction. However as argued by Jalas et al.[31] and Shi et al. [131], an ideal optical isolator should be able to suppress the transmission of arbitrary waves in the backward direction, independent of the presence of a signal in the forward direction or not. It has been hypothesized that nonlinear isolators could display *dynamic reciprocity*, i.e. significant backward noise (weak BP signal) transmission when a strong input is being transmitted [83]. This would represent a significant limitation to the applicability of nonlinear isolators for signal processing and laser protection, for example, in optical communications a backward noise may arrive when a strong forward signal is passing through the optical isolator [131].

### 5.2.5 Counterpropagating nematicons

To address the dynamic reciprocity issue, we study the interaction between counterpropagating (CP) nematicons in $z-$ modulated NLC sample cells. The FP and BP beams are injected respectively from the left ($z = 0$) and right ($z = L$) sides of the NLC sample cell. The normalized input Gaussian profile envelopes are defined by

$$u(Y, Z = 0) = A_b \exp\left(Y^2/W_b^2\right), \tag{5.4}$$
$$v(Y, Z = L) = A_b \exp\left((Y - y_{FP}(L))^2/W_b^2\right), \tag{5.5}$$

where $A_b$ and $W_b$ are the maximum electric field amplitudes and width of the beams, and $y_{FP}(L)$ is the transverse position at $Z = L$ of an FP nematicon with input profile given by (5.4).

The nematicon equations governing the interaction of two mutually incoherent nematicons of the same wavelength propagating in opposite directions along the $z$ axis in a longitudinal modulated NLC cell can be deduced from the equations derived by Alberucci et al. [173], and is given in dimensionless form by the paraxial equations

$$i\frac{\partial u}{\partial Z} + i\gamma\Delta(\theta_b(Z) + \psi)\frac{\partial u}{\partial Y} + \frac{1}{2}\frac{\partial^2 u}{\partial Y^2} + 2A_u\frac{\sin(2\theta_b(Z))}{\sin(2\theta_0(0))}\psi u = 0, \tag{5.6}$$
$$-i\frac{\partial v}{\partial Z} + i\gamma\Delta(\theta_b(Z) + \psi)\frac{\partial v}{\partial Y} + \frac{1}{2}\frac{\partial^2 v}{\partial Y^2} + 2A_u\frac{\sin(2\theta_b(Z))}{\sin(2\theta_0(0))}\psi v = 0, \tag{5.7}$$
$$\nu\frac{\partial^2 \psi}{\partial Y^2} + 2\frac{\sin(2\theta_b(Z))}{\sin(2\theta_0(0))}(A_u|u|^2 + A_v|v|^2) = 0, \tag{5.8}$$

where the coefficients $A_u$ and $A_v$ are the dimensionless coupling strengths, and the scaling transformation is given

$$y = WY, \quad z = BZ, \tag{5.9}$$

where

$$W = \frac{\lambda}{\pi\sqrt{\Delta\epsilon \sin 2\theta_0}}, \quad B = \frac{2n_e\lambda}{\pi\Delta\epsilon \sin 2\theta_0}, \tag{5.10}$$

for a reference Gaussian input beam power of $P_0$, width $W_b$ and wavelength $\lambda$ ($\lambda = 2\pi/k_0$) [99].

The set of equations (5.6), (5.7), and (5.8) determines the response of a test BP nematicon beam to the refractive index perturbation produced by a control FP beam once both waveguides have reached a stationary steady state. Figure 5.9 displays the comparison between simultaneous counterpropagating nematicons and the case when the FP and BP nematicons are injected individually into the sample cell. Figure 5.10 shows the transverse output profiles of the simultaneous counterpropagating FP and BP nematicon beams, for FP and BP beam parameters of $P_b = 2.4mW$, $W_b = 3.5\mu m$ propagating with the same wavelength $\lambda = 1064$ in a $z$-modulated cell defined by $\theta_0 = 20°$ and $\theta_L = 60°$.

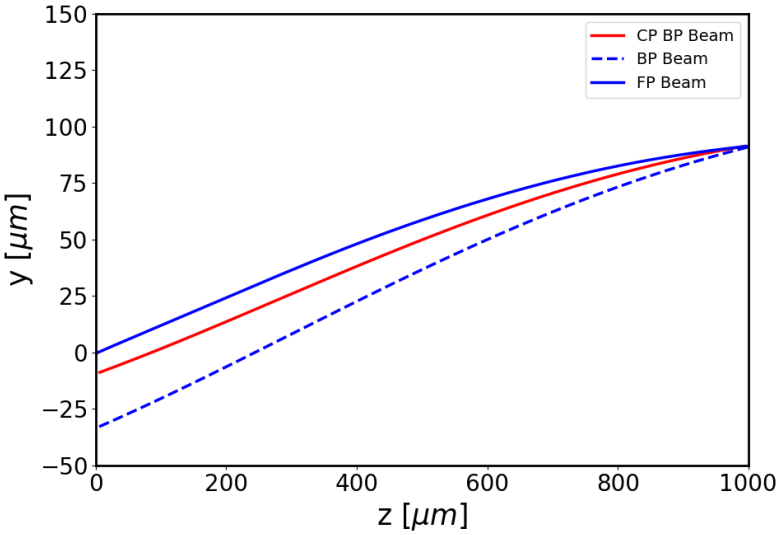


Figure 5.9: Trajectories of FP (blue solid) and BP (blue dashed) nematicon beams injected individually into a $z-$ modulated cell defined by $\theta_0 = 20°$ and $\theta_L = 60°$ and counterpropagating BP (red solid) nematicon beam interacting with the waveguide structure produced by an FP beam with input power $2.4mW$ and width $3.5\mu m$.

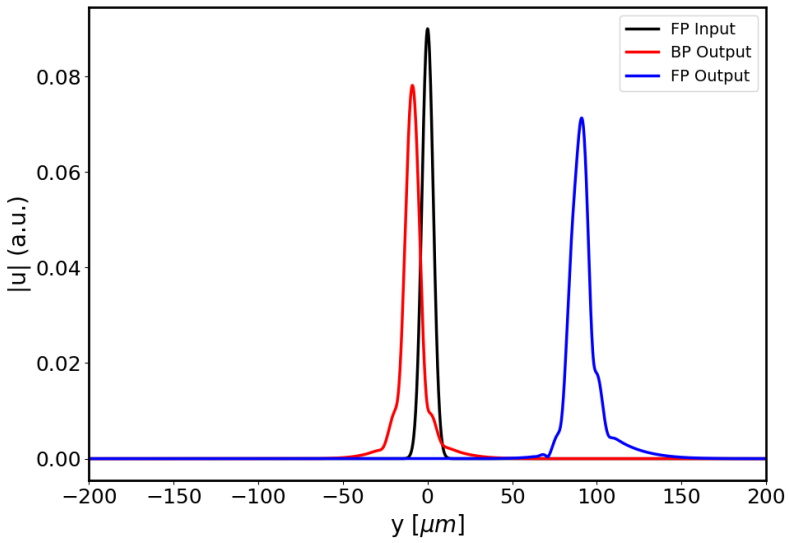


Figure 5.10: Transverse profiles of FP input beam (black solid), BP beam (red) output at $z = 0$ and FP output at $z = L$ for FP and BP beams injected simultaneously into the NLC sample cell.

We observe that the counterpropagating BP beam is attracted to the FP beam when placed under the refractive index perturbation produced by the FP beam (which can be sculpted into the cell via photopolymerization (Section 2.3.2)). Moreover, there is significant crosstalk between the FP and BP beam signals, drastically impacting the original diode-like transmission and proving the existence of dynamic reciprocity for the device under study.

This result is not surprising and is an expected consequence of the strong nonlocal reorientational response of NLC, as nonlocal interactions between nematicons are always attractive due to the positive index perturbation caused by one beam on the other extending beyond the width of the beams [174, 175, 73] (c.f. Figure 5.11). This nonlocal attraction counteracts any repulsion in cases where beams are out of phase, making the interaction between nematicons phase-independent, in contrast to local NLS solitons for which the interaction is attractive if the solitons are in-phase and repulsive if they are out of phase [12].

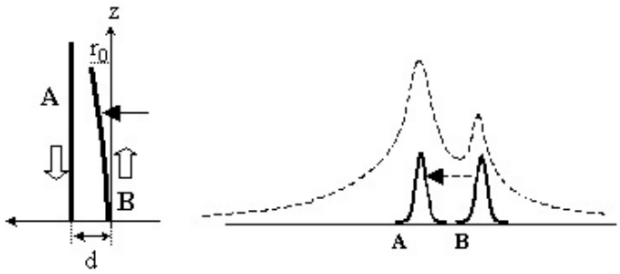


Figure 5.11: Interaction of counter-propagating nonlocal optical solitons. (a) A: Continous wave beam, B: pulsed beam. (b) Overlap of the refractive index profile produced by counterpropagating optical solitons, with the pulsed soliton B attracted towards the heavier soliton A. Reproduced from [176].

Finally, we should remark that we adopted a simplified approach to verify the dynamic reciprocity of our nonlinear isolator, as in reality, the waveguiding structures induced by the nematicons change over time experiencing a transient state before reaching a steady stationary state. To account for the time-dependent behaviour of the waveguides induced by simultaneous counterpropagating nematicons, the system to consider can be adjusted from the paraxial wave equations studied by Belic et al.[177]

$$i\frac{\partial u}{\partial z} + i\gamma\Delta(\theta_b(z)+\psi)\frac{\partial u}{\partial y} + \frac{1}{2}\frac{\partial^2 u}{\partial y^2} + 2\frac{\sin(2\theta_b(z))}{\sin(2\theta_0(0))}\psi u = 0, \tag{5.11}$$

$$-i\frac{\partial v}{\partial z} + i\gamma\Delta(\theta_b(z)+\psi)\frac{\partial v}{\partial y} + \frac{1}{2}\frac{\partial^2 v}{\partial y^2} + 2\frac{\sin(2\theta_b(z))}{\sin(2\theta_0(0))}\psi v + 0, \tag{5.12}$$

$$\frac{\partial \psi}{\partial t} = \frac{\nu\tau}{\bar{\gamma}}\frac{\partial^2 \psi}{\partial y^2} + \frac{\tau}{2}\frac{\sin(2\theta_b(z))}{\sin(2\theta_0(0))}(|u|^2+|v|^2), \tag{5.13}$$

where $\bar{\gamma}$ is a constant proportional to the viscous coefficient of the NCL, $\tau$ is the relaxation time and $\psi = \psi(t, y, z)$. The numerical scheme necessary to solve the system (5.11-5.13) is expensive computationally (both in time and memory) as it requires a series of nested loops in space and time, which results impractical over large numerical grids.

## 5.3 Nematicon-based optical diode limitations

Following the discussion of the previous section, we can conclude that our nematicon-based optical diode presents the main characteristics and limitations of nonlinear nonreciprocal systems outlined by Caloz et al. [132]

1. Time-reversal symmetry breaking due to spatial asymmetry and nonlinear self-biasing (nonlinearity triggered by the signal wave itself).

2. Limitation to restricted excitations, power range and isolation.

3. Limitation to excitation of one direction only at a time, i.e. dynamic reciprocity.

4. Weak nonreciprocity form i.e. reciprocity under phase-conjugation.

Notwithstanding the limitations of nonlinear nonreciprocal systems as true isolators, this does not mean they are useless in technological applications. By carefully choosing the mode of operations, optical isolation is possible and has been demonstrated with discrete systems and integrated with semiconductor laser chips [178, 179]. To maximize scalability and integration into current photonic circuits, a device capable of displaying diode/isolator-like behaviour would be fully passive and magnet-free [179]. The nematicon-based optical diode exhibits those desired characteristics, requires no external drive and can operate without generating electromagnetic interference or a magnetic field background.

# Chapter 6

# Future Work and Conclusions

We have introduced a mechanism of direction-dependent transmission based on signal waveguiding by oppositely propagating nematicons in nonuniformly oriented nematic liquid crystal cells. By tailoring solitary wave formation in nonspecular planar samples excited by oppositely propagating wave packets, counterpropagating nematicons can guide co-polarized signals along distinct nonoverlapping trajectories, effectively leading to a diode-like transmission. We analyzed the role of a linearly modulated background orientation, nonlocality, power and losses, using realistic NLC physical parameters and sample features.

We also stated the limitations of our nematicon-based optical diode as a true isolator, as it exhibits a weak form of nonreciprocity and is constrained by dynamic reciprocity. Nevertheless, it presents several suitable properties that can be exploited in practical applications such as being fully passive, all-optical, magnet-free and providing diode-like transmission for a reasonable optical power range with no need for an external drive.

Subsequent efforts will be focused on detailed performance measurements in order to establish a comparison with state-of-the-art active and magnetic integrated isolators. Additionally, a more systematic approach is required to explore the relationship between our proposed mechanism and similar mechanisms of nonlinear nonreciprocity existing literature (See [126, 131, 132] for example). On the other hand, the addition of thermo-reorientational effects given by equations (3.31)-(3.33) is of particular interest, as it can provide insights into the operational stability of photonic devices based on nematicon waveguide structures under thermal fluctuations.

Finally, a significant limitation of the results presented here is the lack of comparative results for the full (2+1)-D model due to the computational cost of the numerical implementation. The first step to improve the computation time will be to decrease the spatial resolution while checking the convergence of the numerical solutions, in particular, numerical results in the Schrödinger-Newton system indicate that a large number of points in the propagation variable is not necessary to obtain accurate and stable simulation [180, 181].

# Appendix A: Published Papers

## Publication Details

- Enrique Calisto, Noel F. Smyth, and Gaetano Assanto, "Optical isolation via direction-dependent soliton routing in birefringent soft matter," *Opt. Lett. 47*, 2782-2785 (2022).https://doi.org/10.1364/OL.459564

- Enrique Calisto and Gaetano Assanto, "Direction-dependent optical solitary waves in nematic liquid crystals", *Phys. Rev. A 108*, 043509 (2023). https://doi.org/10.1103/PhysRevA.108.043509

- Enrique Calisto and Gaetano Assanto. 2023. "Nonreciprocal Propagation of Nematicons" *Photonics 10*, 1144 (2023). https://doi.org/10.3390/photonics10101144

- Enrique Calisto and Gaetano Assanto, "Counterpropagating optical solitary waves in orientation-modulated nematic liquid crystals, " *Wave Motion,130*,103379 (2024). https://doi.org/10.1016/j.wavemoti.2024.103379.

# Appendix B: Additional Results

The following appendix reports additional results and figures that were produced in the course of this thesis.

## Longitudinally modulated case i.e. $\theta_b = \theta_b(z)$

**1.** $\theta_0$ **to** $\theta_1$ **from** $10°$ **to** $45°$

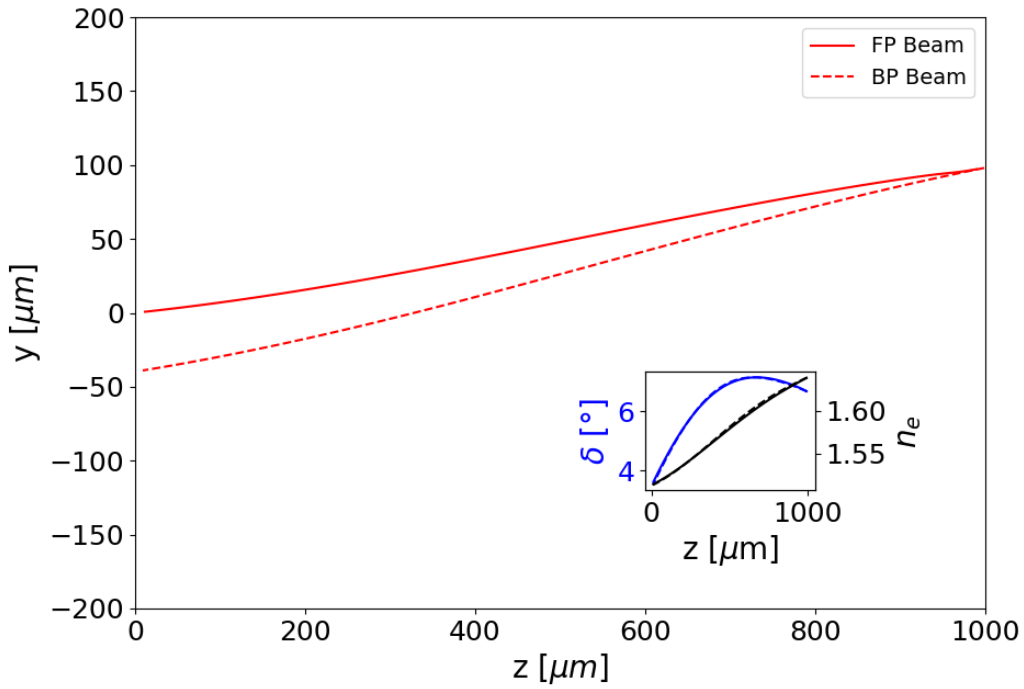


Figure 6.1: FP (solid line) and BP (dashed line) beam trajectories in $(y, z)$ for $\theta_0 = 10°$ and $\theta_1 = 45°$. **Inset:** Calculated walk-off (blue) and refractive index across $y$ (black).

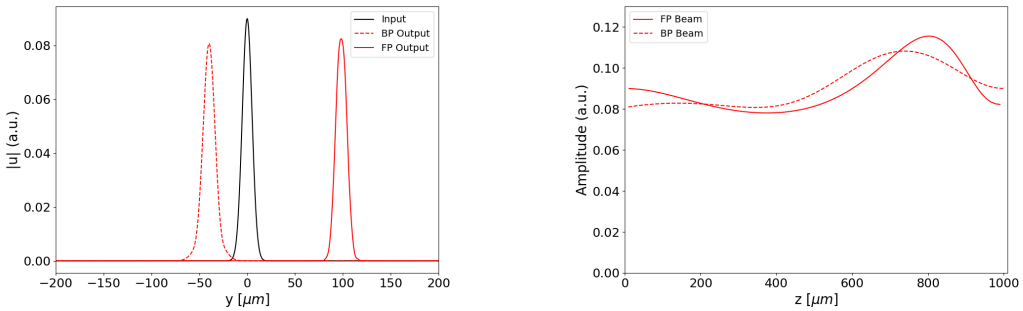


Figure 6.2: (a) Transverse profiles of input beam (black), FP nematicon at $z = L$ (red solid line),BP nematicon at $z = 0$. (b) dimensionless amplitudes of FP(solid line) and BP (dashed line) beams

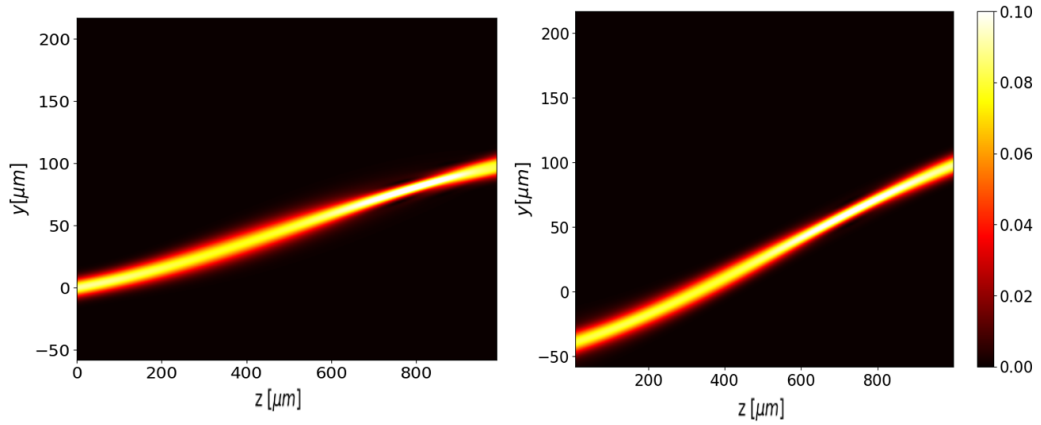


Figure 6.3: Acquired nematicon evolution in $(y, z)$ plane of FP (Left) and BP (Right) nematicons

**2.** $\theta_0$ **to** $\theta_1$ **from** $20°$ **to** $60°$

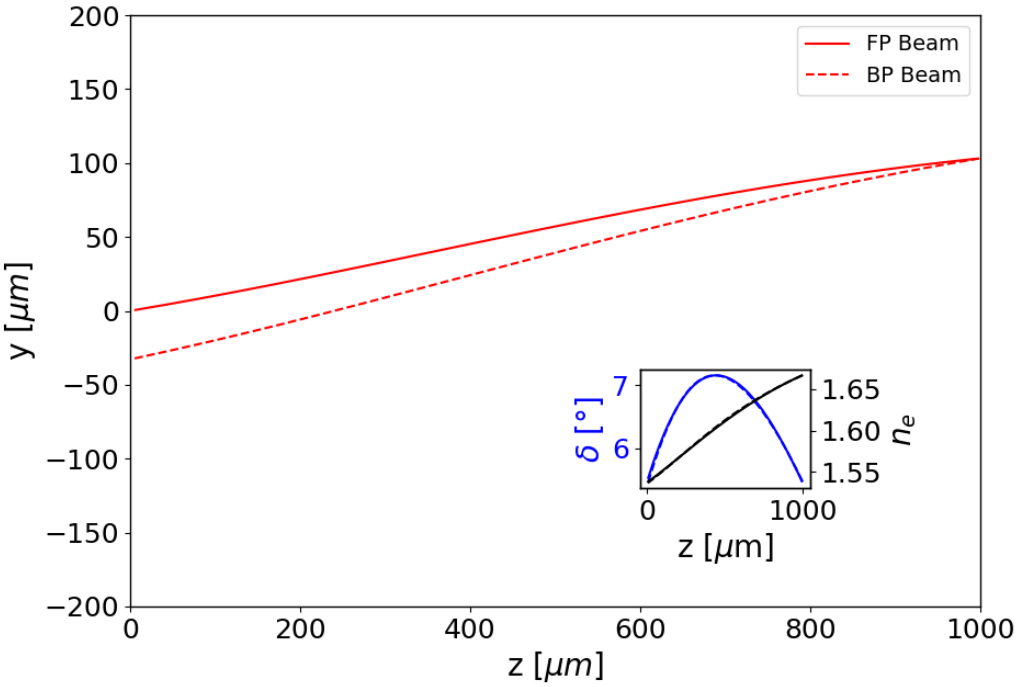


Figure 6.4: Beam trajectory for $\theta_0 = 20°$ and $\theta_1 = 60°$. **Inset:** Compute walk-off (blue) and refractive index (black

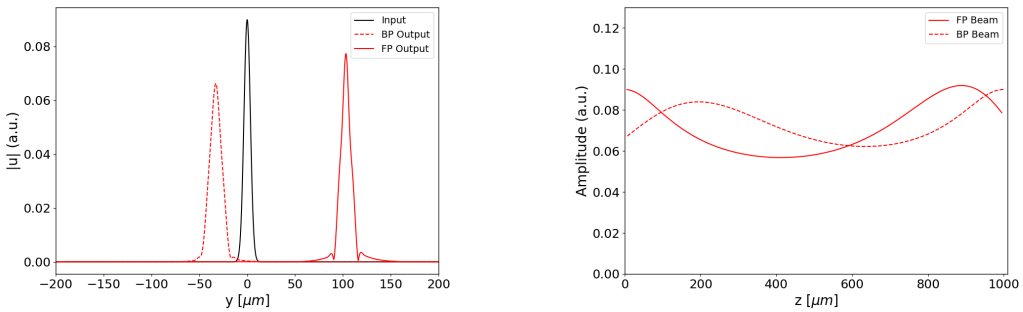


Figure 6.5: (a) Transverse profiles of input beam (black), FP beam at $z = L$ (red solid line), BP beam at $z = 0$. (b) dimensionless amplitudes of FP(solid line) and BP (dashed line) beams

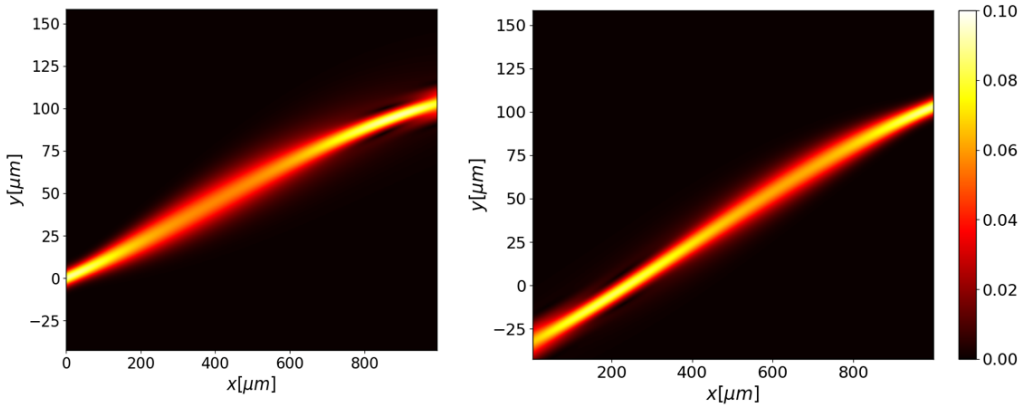


Figure 6.6: Acquired beam evolution in $(y, z)$ plane of FP (Left) and BP (Right) beams for $\theta_0 = 20°$ and $\theta_1 = 60°$

**3.** $\theta_0$ **to** $\theta_1$ **from** $25°$ **to** $65°$

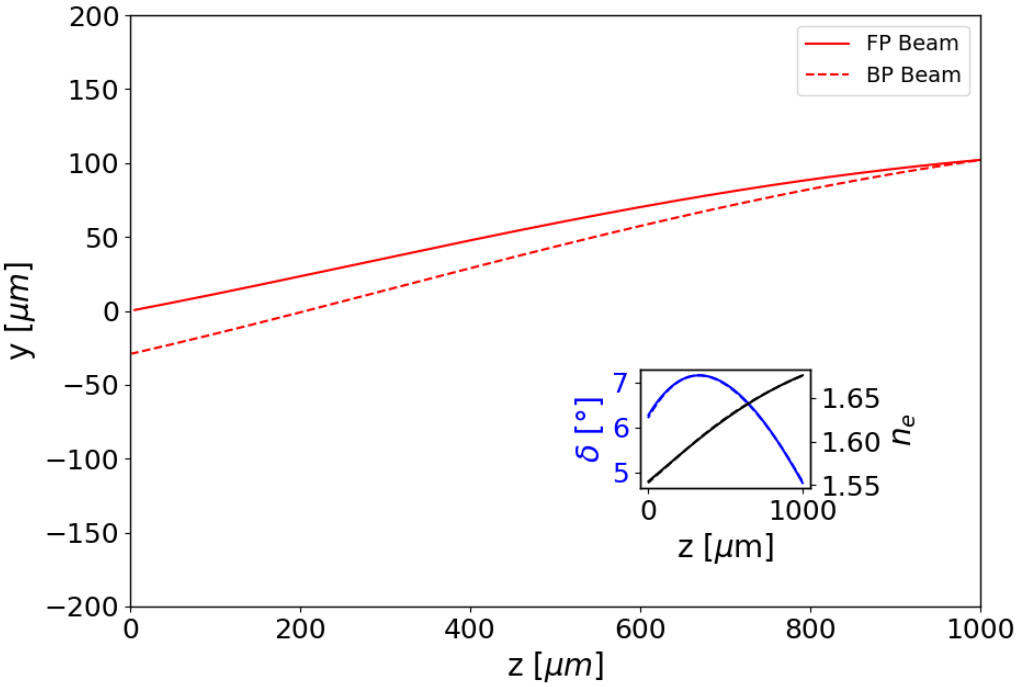


Figure 6.7: Beam trajectory for $\theta_0 = 25°$ and $\theta_1 = 65°$. **Inset:** Compute walk-off (blue) and refractive index (black

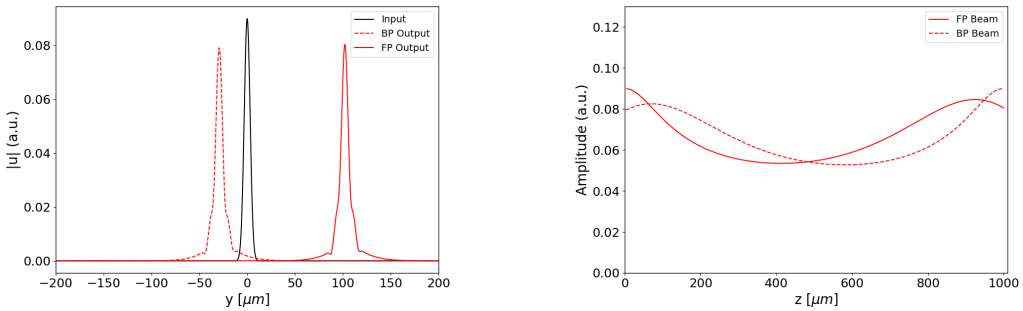


Figure 6.8: (a) Transverse profiles of input beam (black), FP beam at $z = L$ (red solid line),BP beam at $z = 0$. (b) dimensionless amplitudes of FP(solid line) and BP (dashed line) beams

**4.** $\theta_0$ **to** $\theta_1$ **from** $45°$ **to** $60°$

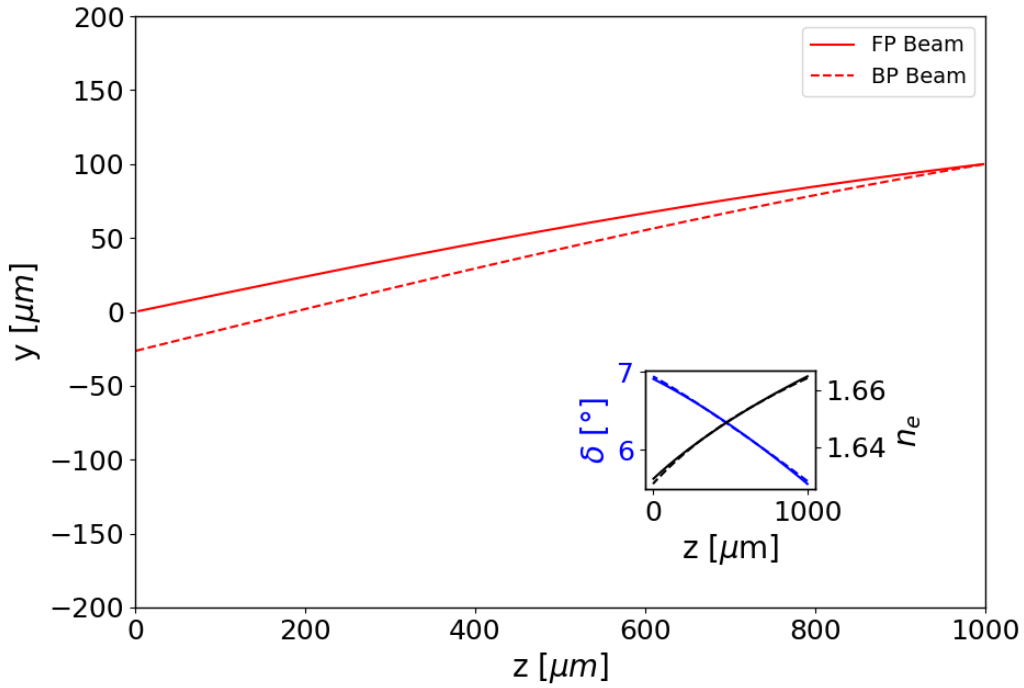


Figure 6.9: Beam trajectory for $\theta_0 = 25°$ and $\theta_1 = 65°$. **Inset:** Compute walk-off (blue) and refractive index (black

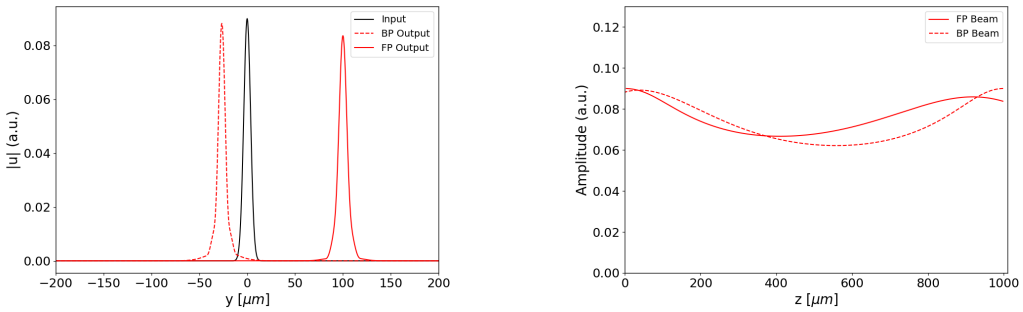


Figure 6.10: (a) Transverse profiles of input beam (black), FP beam at $z = L$ (red solid line), BP beam at $z = 0$. (b) dimensionless amplitudes of FP(solid line) and BP (dashed line) beams

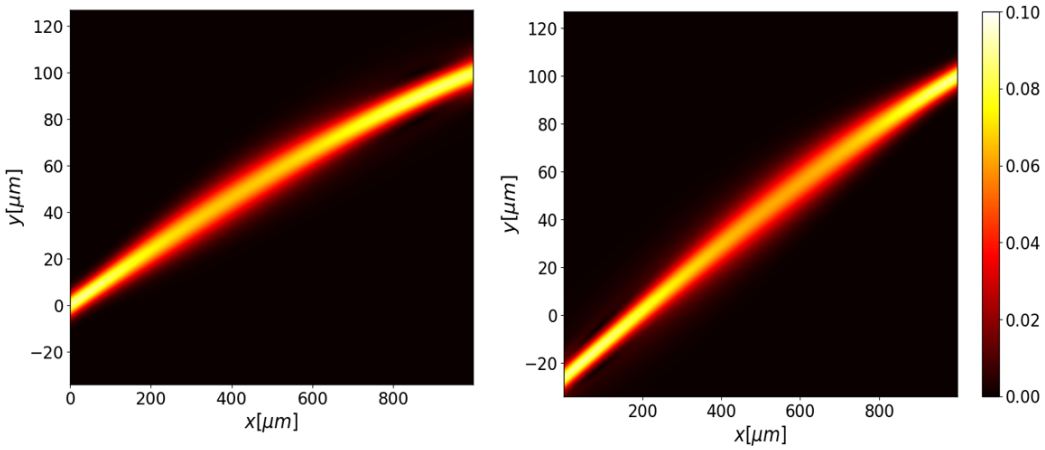


Figure 6.11: Acquired beam evolution in $(y, z)$ plane of FP (Left) and BP (Right) beams for $\theta_0 = 45°$ and $\theta_1 = 60°$

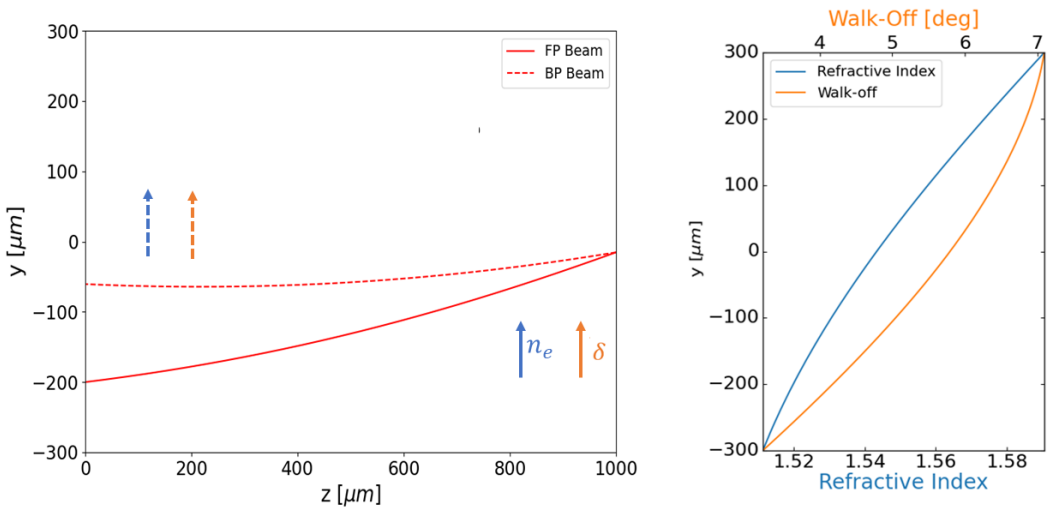


Figure 6.12: **Left:** FP (solid line) and BP (dashed line) nematicon trajectories in $(y, z)$ for $\theta_{top} = 15°$ and $\theta_{bot} = 45°$ ($\theta_{in}(y_0) = 20°$). **Right:** Calculated walk-off (orange) and refractive index across $y$.

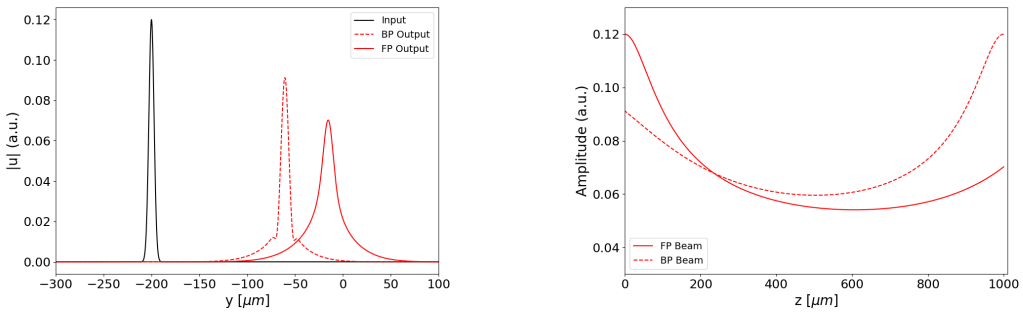


Figure 6.13: (a) Transverse profiles of input beam (black), FP nematicon at $z = L$(red solid line), BP nematicon at $z = 0$. (b) dimensionless amplitudes of FP(solid line) and BP (dashed line) beams

# Transverse modulated case i.e. $\theta_b = \theta_b(y)$

## Case 1: $\theta_{bot}$ to $\theta_{top}$ from $15°$ to $45°$

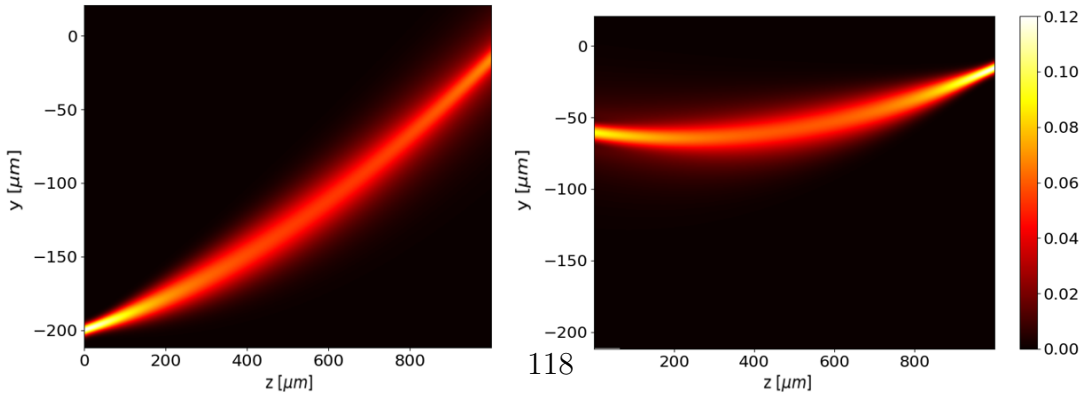




Figure 6.14: **Left:** Acquired nematicon evolution in $(y, z)$ plane of FP (Left) and BP (Right) nematicons

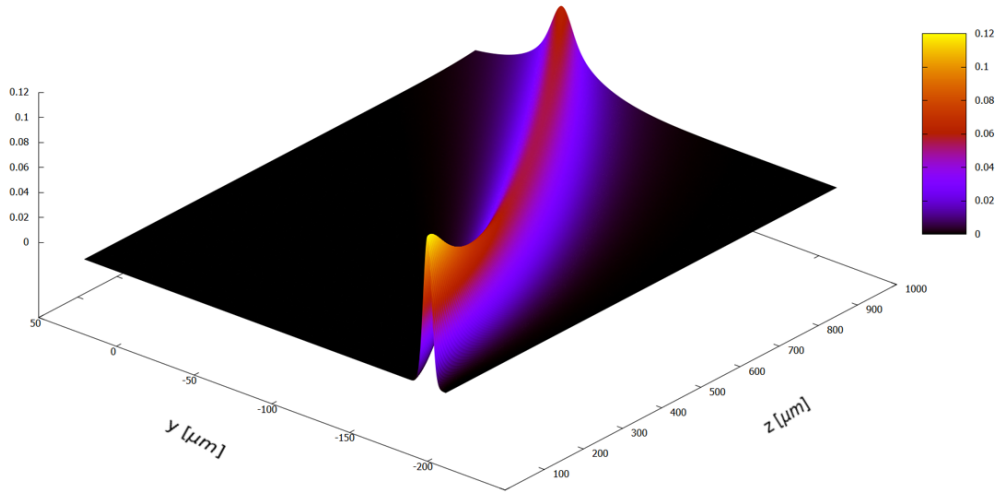


Figure 6.15: 3D plot for nematicon evolution in $(y, z)$ plane of the FP nematicon

## Case 2: $\theta_{bot}$ to $\theta_{top}$ from $75°$ to $45°$

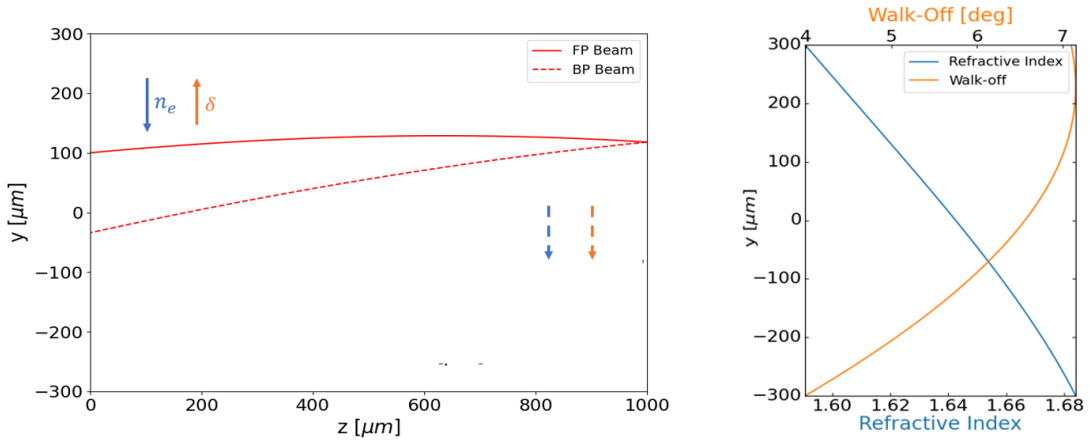


Figure 6.16: **Left:** FP (solid line) and BP (dashed line) beam trajectories in $(y, z)$ for $\theta_{bot} = 75°$ and $\theta_{top} = 45°$ ($\theta_{in}(y_0) = 55°$). **Right:** Calculated linear walk-off (orange) and refractive index across $y$.

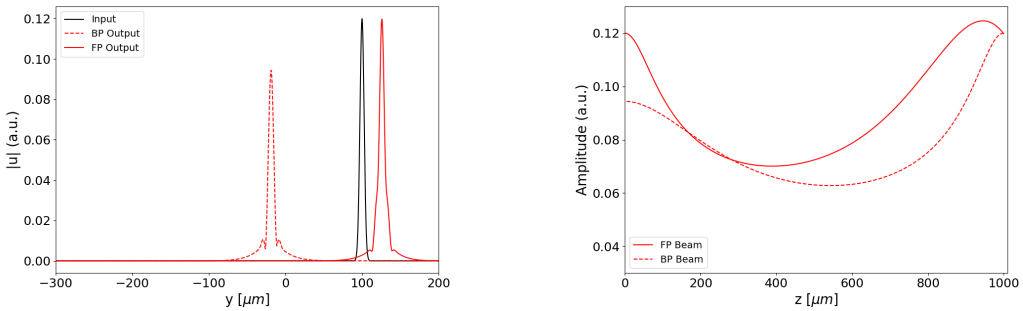


Figure 6.17: (a) Transverse profiles of input beam (black), FP nematicon at $z = L$(red solid line), BP nematicon at $z = 0$. (b) dimensionless amplitudes of FP(solid line) and BP (dashed line) beams

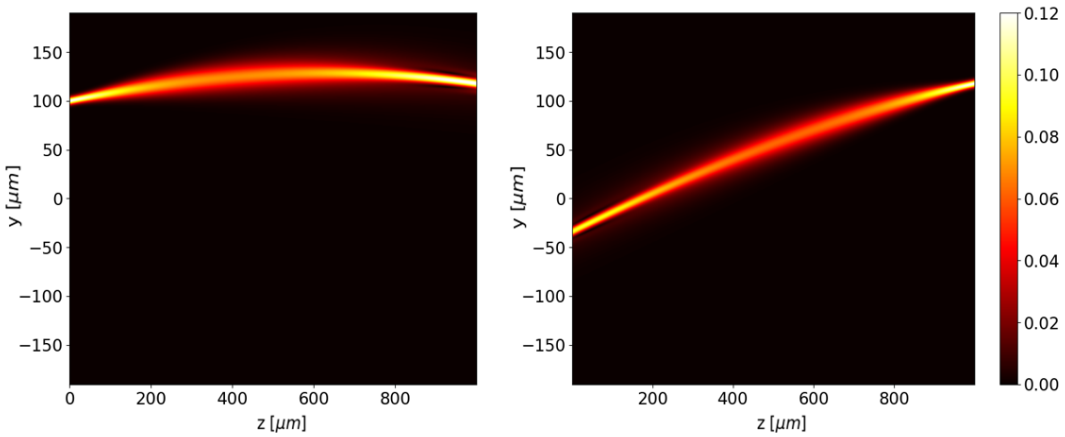


Figure 6.18: Acquired nematicon evolution in $(y, z)$ plane of FP (Left) and BP (Right) nematicons

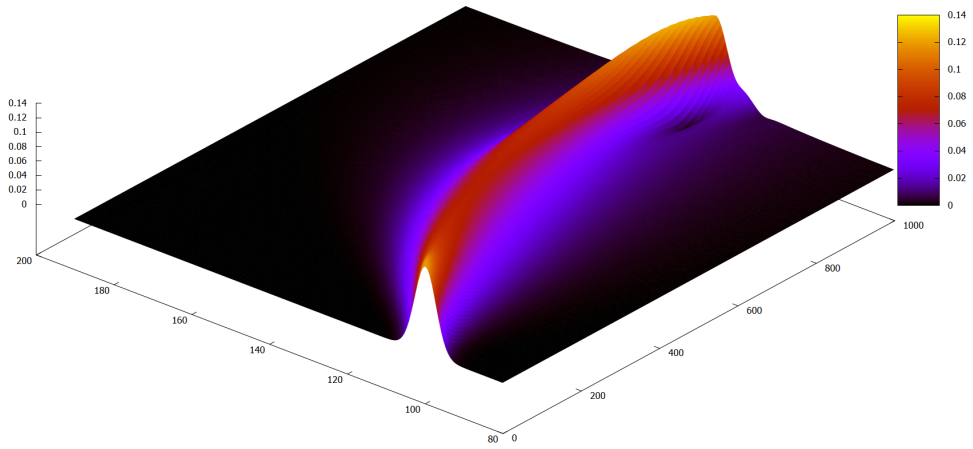

Figure 6.19: 3D plot for nematicon evolution in $(y, z)$ plane of the FP nematicon

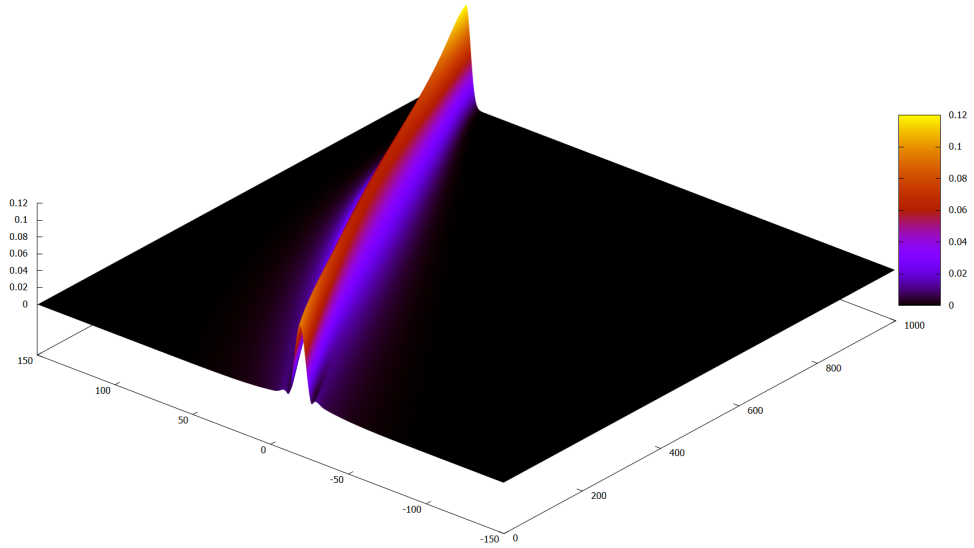

Figure 6.20: 3D plot for nematicon evolution in $(y, z)$ plane of the BP nematicon

## Case 3: $\theta_{bot}$ to $\theta_{top}$ from $15°$ to $45°$

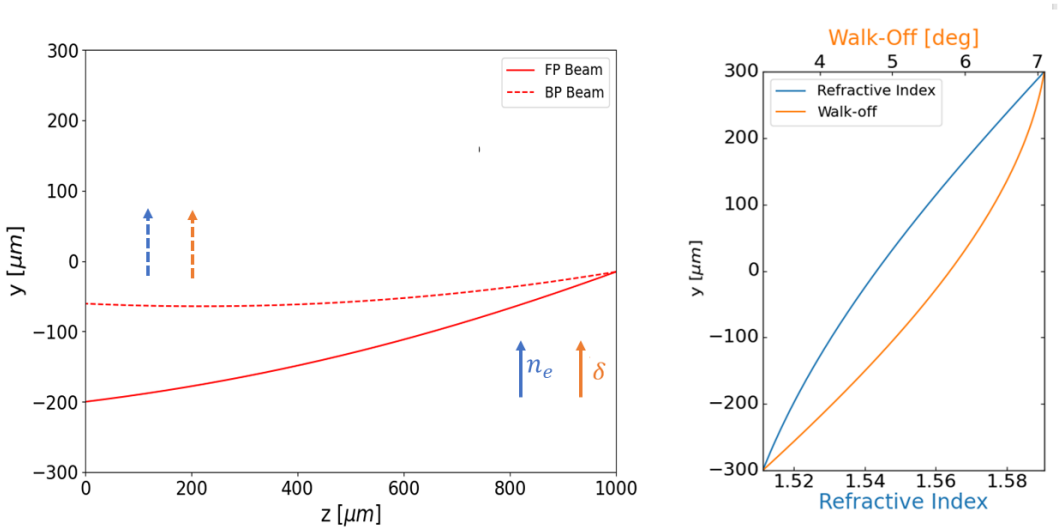


Figure 6.21: **Left:** FP (solid line) and BP (dashed line) nematicon trajectories in $(y, z)$ for $\theta_{bot} = 15°$ and $\theta_{top} = 45°$ ($\theta_{in}(y_0) = 20°$). **Right:** Calculated linear walk-off (orange) and refractive index across $y$.

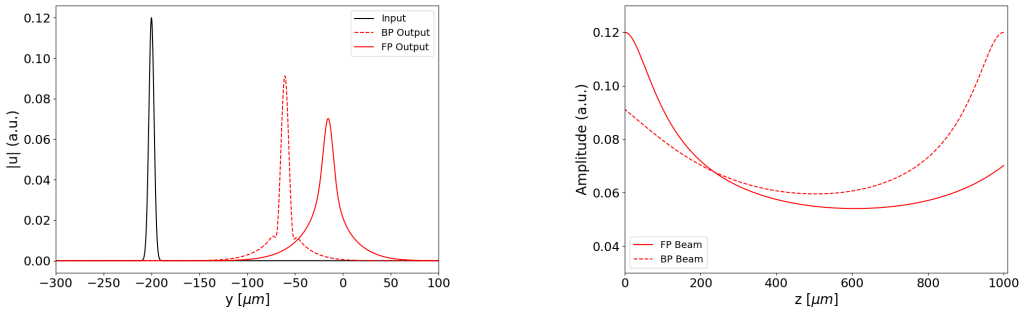


Figure 6.22: (a) Transverse profiles of input beam (black), FP nematicon at $z = L$(red solid lin e),BP nematicon at $z = 0$. (b) dimensionless amplitudes of FP(solid line) and BP (dashed line) beams

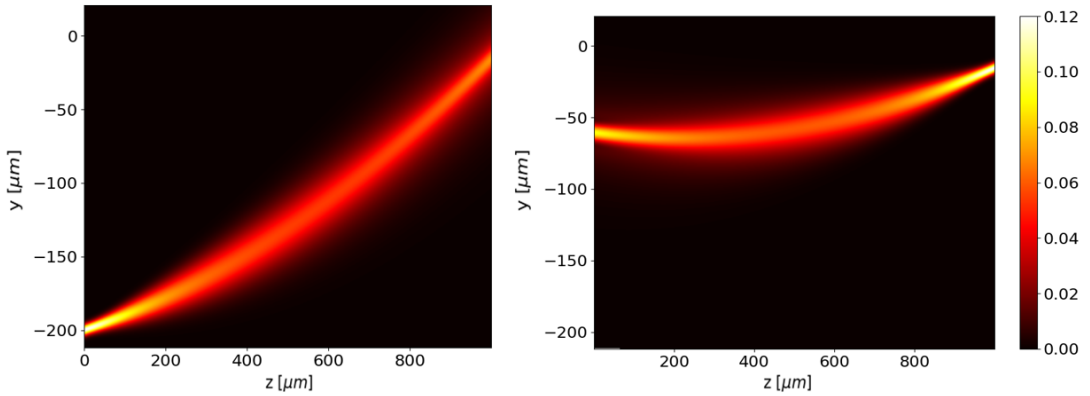


Figure 6.23: **Left:** Acquired nematicon evolution in $(y, z)$ plane of FP (Left) and BP (Right) nematicons

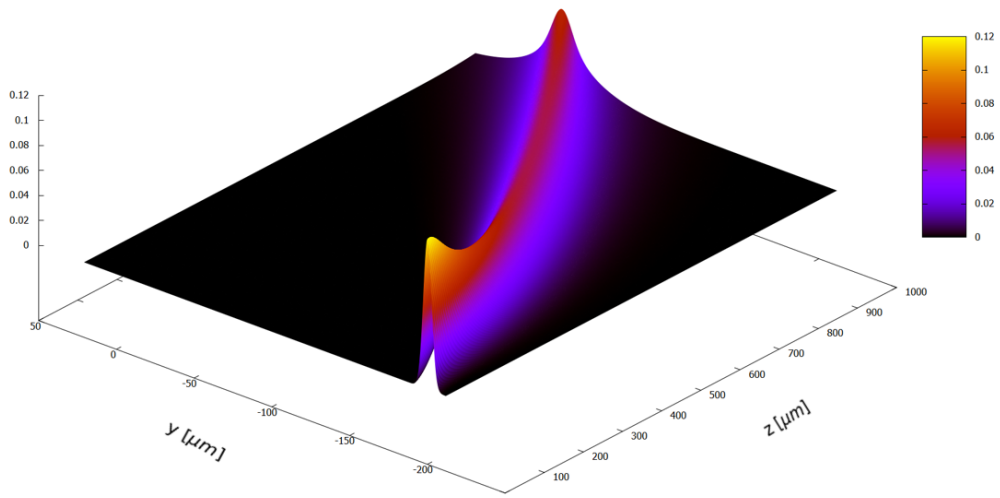


Figure 6.24: 3D plot for nematicon evolution in $(y, z)$ plane of the FP nematicon

# Bibliography


[1] J.Russell, & J.Robinson (1838). "Report of the Committee on Waves" : Appointed by the British Association at Bristol in 1836 [and consisting of Sir John Robison and John Scott Russell]. London: Printed by Richard and John E. Taylor.

[2] Alex Kasman. "A brief history of solitons and the KdV equation". *Current science 150*, 18 (2018).

[3] G. Whitham, *Linear and nonlinear waves*, Wiley, New York (1974).

[4] N. J. Zabusky and M. D. Kruskal, "Interaction of 'solitons' in a collisionless plasma and the recurrence of initial states," *Phys. Rev. Lett., 15*, 240 (1965).

[5] C. Gardner, J. Greene, M. Kruskal and R. Miura, "Method for solving the Korteweg deVries equation," *Phys. Rev. Lett., 19*, 1095-1097 (1967).

[6] M. Ablowitz and H. Segur. *Solitons and the Inverse Scattering Transform* , SIAM, Philadelphia (1981).

[7] G. Hwang, T. Akylas, and J. Yang, "Gap solitons and their linear stability in onedimensional periodic media," *Physica D: Nonlinear Phenomena, 240*, 12,1055-1068, (2011).

[8] K. B. Dysthe and K. Trulsen, "Note on breather type solutions of the NLS as models for freak-waves," *Physica Scripta,. 1999*, T82, 48-52, (1999).

[9] L. F. Mollenauer and J. P. Gordon, *Solitons in optical fibers*, Elsevier Academic Press, (2006)

[10] P. Emplit, J.P. Hamaide, F. Reynaud,C. Froehly, A. Barthelemy, "Picosecond steps and dark pulses through nonlinear single-mode fibers," *Optics. Comm., 62*, 374-379 (1987).

[11] A. Hasegawa and F. Tappert, "Transmission of stationary nonlinear optical pulses in dispersive dielectric fibres. I. Anomalous dispersion," *Appl. Phys. Lett., 23*, 142-144 (1973).

[12] G.P. Agrawal. *Nonlinear fibre optics*. 3rd edn. San Diego, Academic Press, (2001).

[13] S. Trillo and W. Torruellas. *Spatial solitons*. Berlin, Springer-Verlag, (2001).

[14] Y.S. Kivshar and G.P. Agrawal. *Optical solitons: from fibres to photonic crystals*. New York, Elsevier, (2003).

[15] G Assanto. *Nematicons: Spatial optical solitons in nematic liquid crystals*. New York, John Wiley and Sons, (2012).

[16] M.Peccianti and G.Assanto, Nematicons, *Phys. Rep.516*,147(2012)

[17] Y.R. Shen. *The principles of nonlinear optics*. New York, John Wiley & Sons, (1984), 286–331 (Chapters 16–17).

[18] R.W. Boyd. *Nonlinear optics*. 3rd edn. Amsterdam, Netherlands, Academic Press, (2008).

[19] M. Lax, W.H. Louisell and W.B. McKnight. From Maxwell to paraxial wave optics. *Phys. Rev. A. 11*, 1365–1370, (1975).

[20] A. C. Newell and J. V. Moloney, *Nonlinear Optics*. Reading, MA: Addison-Wesley, (1992).

[21] V. Skarka,V.I. Berezhiani, R. Miklaszewski, "Spatiotemporal dynamics of electromagnetic pulses in saturating nonlinear optical media with normal group velocity dispersion," *Phys. Rev. E, 60*, 7622-7625 (1999).

[22] A.L. Dyshko, V.N Lugovi, A.M. Prokhorov, "Multifocus structure of a beam in a nonlinear medium," *Sov. Physics JETP, 34*, 1235 (1972).

[23] G. Fibich, G.C. Papanicolaou, "Self-focusing in the presence of small-time dispersion and nonparaxiality," *Opt. Lett., 22*, 1379-1381 (1997).

[24] D. Briedis, D. E. Petersen, D. Edmundson, W. Krolikowski, and O. Bang, "Ring vortex solitons in nonlocal nonlinear media" *Opt. Express 13*, 435 (2005).

[25] A. I. Yakimenko, Y. A. Zaliznyak, and Y. Kivshar, "Stable vortex solitons in nonlocal self-focusing nonlinear media", *Phys. Rev. E 71*, 065603(R) (2005).

[26] A.W Snyder and D.J. Mitchell. "Accessible solitons".*Science 276*, 1538–1541. (1997).

[27] D.J. Mitchell and A.W. Snyder. "Soliton dynamics in a nonlocal medium". *J. Opt. Soc. Am. B 16*, 236–239, (1999).

[28] W. Królikowski, O Bang, J.J. Rasmussen and J. Wyller. "Modulational instability in nonlocal nonlinear Kerr media". *Phys. Rev. E 64*, 016612 (2001).

[29] A.I. Yakimenko, V.M. Lashkin and O.O. Prikhodko. "Dynamics of two-dimensional coherent structures in nonlocal nonlinear media". *Phys. Rev. E 73*, 066605 (2006).

[30] U. Laudyn, M. Kwasny, F. Sala, M. Karpierz, N.F. Smyth, G. Assanto, "Curved solitons subject to transverse acceleration in reorientational soft matter", *Sci.Rep. 7*, 12385 (2007).

[31] D. Jalas, A. Petrov, M. Eich, MW. Freude, S. Fan, Z. Yu, R. Baets, M. Popović, A. Melloni, J.D. Joannopoulos, et al. "What is—And what is not—An optical isolator", *Nature Photon. 7*, 579–582 (2013).

[32] Z.F. Yu, Z. Wang, S.H. Fan, "One-way total reflection with one-dimensional magneto-optical photonic crystals", *Appl. Phys.Lett. 90*, 121133 (2007).

[33] T. Amemiya, H. Shimizu, M. Yokoyama, P.N. Hai, M.Tanaka, Y. Nakano, "1.54$\mu$m TM-mode waveguide optical isolator based on the nonreciprocal-loss phenomenon: Device design to reduce insertion loss", *Appl. Opt. 46*, 5784-5791 (2007).

[34] N. Kono, K. Kakihara, K. Saitoh, M. Koshiba, "Nonreciprocal microresonators for the miniaturization of optical waveguide isolators", *Opt. Express 15*, 7737-7751 (2007).

[35] Y. Yazaki, Y. Shoji, T. Mizumoto, "Demonstration of interferometric waveguide optical isolator with a unidirectional magnetic field", *Jpn. J. Appl. Phys. 56*,5460-5464 (2007).

[36] X.S. Lin, J.H. Yan, L.J. Wu, S. Lan, "High transmission contrast for single resonator based all-optical diodes with pump-assisting", *Opt. Express 16*, 20949-20954 (2008).

[37] S. Trillo and S. Wabnitz, "Nonlinear nonreciprocity in a coherent mismatched directional coupler", *Appl.Phys. Lett. 49*,752-754 (1986).

[38] P. Ferro, S. Trillo, S. Wabnitz, "Demonstration of nonlinear nonreciprocity and logic operations with a twisted birefringent optical fiber", *Opt. Lett. 19*,263-265 (1994).

[39] C.G. Treviño-Palacios, G.I. Stegeman, P. Baldi, "Spatial nonreciprocity in waveguide second-order processes", *Opt. Lett. 21*,1442-1444 (1996).

[40] K. Gallo and G. Assanto, "All-optical diode based on second-harmonic generation in an asymmetric waveguide", *J. Opt. Soc. Am. B 16*, 267-269 (1999).

[41] K. Gallo, G. Assanto, K.R. Parameswaran, M.M. Fejer, "All-optical diode in a periodically-poled Lithium Niobate waveguide", *Appl.Phys. Lett. 79*, 314-316 (2001).

[42] H. Zhou, K.F. Zhou, W. Hu, Q. Guo, S. Lan, X.S. Lin, A. Venu Gopal, "All-optical diodes based on photonic crystal molecules consisting of nonlinear defect pairs", *J. Appl. Phys. 99*,123111 (2006).

[43] X.S. Lin, W.Q. Wu, H. Zhou, K.F. Zhou, S. Lan, "Enhancement of unidirectional transmission through the coupling of nonlinear photonic crystal defects", *Opt. Express 14* 2429-2439 (2006).

[44] D. Alexander, J. Bruce, C. Zuhlke, B. Koch, R. Rudebusch, J. Deogun, H. Hamza, "Demonstration of a nanoparticle-based optical diode", *Opt. Lett. 31*,1957-1959 (2006).

[45] S. Chandrasekhar. *Liquid Crystals*, Cambridge University Press, 2 edition, (1992).

[46] P.G De Gennes and J. Prost. *The Physics of Liquid Crystals*, Clarendon Press, Oxford, (1993).

[47] Courtesy of HowStuffWorks. *Liquid Crystal Display*[Online]. Available: `https://www.theengineeringknowledge.com/`

[48] B.Averill and P.Eldredge, *General Chemistry: Principles, Patterns, and Applications*, Saylor Foundation,(2011).

[49] D. Andrienko. Introduction to liquid crystals. *Journal of Molecular Liquids, 267*,520 – 541, Special Issue Dedicated to the Memory of Professor Y. Reznikov, (2018).

[50] I.C. Khoo, *Liquid Crystals: Physical Properties and Nonlinear Optical Phenomena*, Wiley, (1995).

[51] S. Missaoui and M. Kaddour, "Co-design of an antenna filter RF with anisotropy of liquid crystal", presented at *5ème Conférence Internationale des Energies Renouvelables (CIER– 2017)*, (2017).

[52] K. Binder, S. Egorov, A. Milchev and A. Nikoubashman, "Understanding the properties of liquid-crystalline polymers by computational modelling", *J. Phys. Mater. 3*, 032008 (2020).

[53] Courtesy of Jan Pavelka, *Double refraction in calcite* [Online]. Available: `https://commons.wikimedia.org/wiki/File:Fluorescence_in_calcite.jpg`

[54] V. Freedericksz and V. Zolina, "Forces causing the orientation of an anisotropic liquid", *Trans. Faraday Soc. 29*, 919 (1927)

[55] G. Assanto, M. Peccianti and C. Conti, "Nematicons: Optical Spatial Solitons in Nematic Liquid Crystals," *Optics & Photonics News 14*(2), 44-48 (2003).

[56] S. Baqer, D.J. Frantzeskakis, T.P. Horikis, C. Houdeville, T.R. Marchant and N.F. Smyth, "Nematic Dispersive Shock Waves from Nonlocal to Local," *Applied Sciences 11,* (11) 4736 (2021).

[57] M. Peccianti, A. De Rossi, G. Assanto, A. De Luca, C. Umeton and I. Khoo, "Electrically assisted self-confinement and waveguiding in planar nematic liquid crystal cells," *Appl. Phys. Lett.77*, 7-9 (2000).

[58] L. Weng et al. "Anchoring energy enhancement and pretilt angle control of liquid crystal alignment on polymerized surfaces". *AIP Advances 5*,097218 (2015).

[59] G.Assanto and M.Karpiez, "Nematicons: self-localised beams in nematic liquid crystals", *Liq. Crystal.36*,1161(2009).

[60] G. D. Ziogos and E. E. Kriezis, "Modeling light propagation in liquid crystal devices with a 3-D full-vector finite-element beam propagation method," *Opt. Quantum Electron. 40*, 733–748 (2008).

[61] F. A. Sala, N. F. Smyth, U. A. Laudyn, M. A. Karpierz, A. A. Minzoni, and G. Assanto, "Bending reorientational solitons with modulated alignment," *J. Opt. Soc. Am. B 34*, 2459-2466 (2017)

[62] J. Beeckman, K. Neyts, X. Hutsebaut, C. Cambournac and M. Haelterman, "Time Dependence of Soliton Formation in Planar Cells of Nematic Liquid Crystals," *IEEE J. Quantum Electron. 41*, 735–740 (2005).

[63] A. Newell. *Solitons in mathematics and physics*. SIAM, Philadelphia (1985)

[64] M. Segev, B. Crosignani, A. Yariv, and B. Fischer, "Spatial solitons in photorefractive media," *Phys. Rev. Lett. 68*, 923, (1992).

[65] N. Ghofraniha, C. Conti, G. Ruocco, S. Trillo, "Shocks in nonlocal media", *Phys. Rev. Lett. 99*,043903 (2007).

[66] I.M. Moroz, R. Penrose, P. Tod, "Spherically-symmetric solutions of the Schrödinger–Newton equations", *Classical Quantum Gravity 15*,2733–2742 (1998).

[67] A. Paredes and H. Michinel, "Interference of dark matter solitons and galactic offsets", *Phys. Dark Universe 12*, 50–55 (2016).

[68] A. Navarrete, A. Paredes, J.R. Salgueiro, H. Michinel, "Spatial solitons in thermo-optical media from the nonlinear Schrödinger–Poisson equation and dark-matter analogues", *Phys. Rev. A 95*,013844 (2015).

[69] A. Piccardi, A. Alberucci, N. Tabiryan, G. Assanto, "Dark nematicons", *Opt. Lett. 36*,1356–1358 (2011).

[70] G. Assanto and N. Smyth. "Light-Induced Waveguides in Nematic Liquid Crystals",*IEEE Journal of Selected Topics in Quantum Electronics. 22* 24400306. (2015)

[71] M. Peccianti, C. Conti, G. Assanto, A. De Luca and C. Umeton, "Routing of Anisotropic Spatial Solitons and Modulational Instability in liquid crystals", *Nature 432*, 733-737 (2004).

[72] S. Perumbilavil, A. Piccardi, R. Barboza, O. Buchnev, G. Strangi, M. Kauranen, G. Assanto, "Beaming random lasers with soliton control", *Nature Commun. 9*,3863 (2018).

[73] J.F. Henninot, J.F. Blach, M. Warenghem, "Enhancement of dye fluorescence recovery in nematic liquid crystals using a spatial optical soliton", *J. Appl. Phys. 107*,113111 (2010).

[74] M. Peccianti and G. Assanto, "Signal readdressing by steering of spatial solitons in bulk nematic liquid crystals", *Opt. Lett. 26*, 1690–1692 (2001).

[75] Y.V. Izdebskaya, A.S. Desyatnikov,G. Assanto and Y.S. Kivshar, "Multimode nematicon waveguides", *Opt. Lett. 36*, 184 (2011).

[76] N. Karimi et al. "Moulding optical waveguides with nematicons", *Adv. Opt. Mat. Commun.*,5,1700199 (2017).

[77] G. Assanto, "Nematicons: Reorientational solitons from optics to photonics", *Liq.Cryst. Rev. 6*,170-194(2018).

[78] S. V. Serak, N. V. Tabiryan, M. Peccianti, and G. Assanto. "Spatial soliton all-optical logic gates", *IEEE Photon. Technol. Lett.,* 18,1287–1289, (2006).

[79] A. Pasquazi, A. Alberucci, M. Peccianti, and G. Assanto, "Signal processing by optooptical interactions between self-localized and free propagating beams in liquid crystals", *Appl. Phys. Lett. 87*, 261104, (2005).

[80] M.Peccianti and G. Assanto, "Signal readdressing by steering of spatial solitons in bulk nematic liquid crystals",*Opt. Lett. 26*, 1690–1692 (2001).

[81] V.R. Almeida, C.A. Barrios, R.R. Panepucci and M. Lipson, "All-optical control of light on a silicon chip", *Nature 431*, 1081–1084(2004).

[82] Z.G. Zheng et al. "Three-dimensional control of the helical axis of a chiral nematic liquid crystal by light", *Nature 531*, 352–356,(2016).

[83] L.Fan et al. "An All-Silicon Passive Optical Diode", *Science 335*, 447–450 (2012).

[84] C.Wang, X.L. Zhong and Z.Y. Li, "Linear and passive silicon optical isolator", *Scientific Reports 2* (2012).

[85] C.Y.Wang et al. "All-optical transistor- and diode-action and logic gates based on anisotropic nonlinear responsive liquid crystal", *Sci Rep 6*, 30873 (2016).

[86] J.X. Fu, R.J.Liu and Z.Y. Li, "Robust one-way modes in gyromagnetic photonic crystal waveguides with different interfaces", *Appl. Phys. Lett. 97*, 041112 (2010).

[87] A.M. Levy, "Nanomagnetic route to bias-magnet-free on-chip Faraday rotators", *J. Opt. Soc. Am. B 22*, 254–260 (2005).

[88] H. Zhou et al. "All-optical diodes based on photonic crystal molecules consisting of nonlinear defect pairs", *J. Appl. Phys. 99*, 123111 (2006).

[89] M.S. Kang, A. Butsch, and P. St. J. Russell, "Reconfigurable light-driven optoacoustic isolators in photonic crystal fibre", *Nat. Photonics 5*, 549–553 (2011)

[90] C. Vassallo, *Optical Waveguide Concepts*, Ch. 1, Elsevier, (1991)

[91] D. M. Pozar, *Microwave Engineering*, Wiley, New York (2012).

[92] V. S. Asadchy, M. S. Mirmoosa, A. Díaz-Rubio, S. Fan and S. A. Tretyakov, "Tutorial on Electromagnetic Nonreciprocity and its Origins," *Proceedings of the IEEE, 108*,10,1684-1727, (2020).

[93] B. Fornberg and G. B. Whitham, "A Numerical and Theoretical Study of Certain Nonlinear Wave Phenomena", *Phil. Trans. R. Soc. Lond. A, 289*, 373-403 (1978).

[94] F. If, P. Berg, P. L. Christiansen and O. Skovgaard, "Split-step spectral method for nonlinear Schrodinger equation with absorbing boundaries", *J. Comp. Phys., 72*, 501-503 (1987).

[95] W. H. Press, B. P. Flannery, S. A. Teukolsky, W. T. Vetterling, *Numerical Recipes in Fortran 77 - The Art of Scientific Computing*, Cambridge University Press (1986, 1992).

[96] G.El,M.Hoefer, and M. Shearer, "Dispersive and DiffusiveDispersive Shock Waves for Nonconvex Conservation Laws", *SIAM Review, 59*(1), 3-61 (2017)

[97] G. Assanto, A. Fratalocchi, and M. Peccianti, "Spatial solitons in nematic liquid crystals: From bulk to discrete," *Opt. Express 15*, 5248–5259 (2007)

[98] F. A. Sala and M. A. Karpierz, "Modeling of nonlinear beam propagation in chiral nematic liquid crystals," *Mol. Cryst. Liq. Cryst. 558*, 176–183 (2012)

[99] G. Assanto, A. A. Minzoni, M. Peccianti, and N. F. Smyth, "Optical solitary waves escaping a wide trapping potential in nematic liquid crystals: modulation theory," *Phys. Rev. A 79*, 033837 (2009).

[100] C. Conti, M. Peccianti, G. Assanto, "Route to nonlocality and observation of accessible solitons", *Phys. Rev. Lett. 91*, 073901 (2003).

[101] I. C. Khoo, "Principal nonresonant optical nonlinearities of nematic and isotropic liquid crystals," *Nonlinear Optics and Optical Physics*, 176–210 (1994).

[102] B. D. Skuse and N. F. Smyth, "Interaction of two colour solitary waves in a liquid crystal in the nonlocal regime," *Phys. Rev. A 79*,063806(2009)

[103] G.A. El and M.A. Hoefer, "Dispersive shock waves and modulation theory", *Physica D: Nonlinear Phenomena 333*,11-65, (2016).

[104] R. Haberman, *Elementary applied partial differential equations with Fourier series and boundary value problems*, Prentice Hall, New Jersey (1998).

[105] G. Assanto, C. Khan and N.F. Smyth, "Multi-hump thermo-reorientational solitary waves in nematic liquid crystals: Modulation theory solutions", *Phys. Rev. A 104*, 013526 (2020).

[106] L. Abdulkareem, S.F. Abdalah, K. Al Naimee, R. and Meucci, "Temperature effect on nonlinear refractive indices of liquid crystals in visible and NIR", *Optics Communications 363*, 188-194, (2016).

[107] P. Panayotaros and T.R. Marchant, "Solitary waves in nematic liquid crystals", *Phys. D: Nonl. Phenom. 268*, 106 -117 (2014).

[108] J.M.L. MacNeil, N.F. Smyth and G. Assanto, "Exact and approximate solutions for optical solitary waves in nematic liquid crystals", *Phys. D 284*, 1-15 (2014).

[109] M. Peccianti and G. Assanto, "Nematic Liquid Crystals: a suitable medium for self-confinement of coherent and incoherent light", *Phys. Rev. E 65* 035603-035606(R) (2002).

[110] G. Assanto, P. Panayotaros and N.F. Smyth, "Mechanical analogies for nonlinear light beams in nonlocal nematic liquid crystals", *J. Nonl. Opt. Phys. Mater. 27*, 1850046 (2018).

[111] J. P. Borgna, P. Panayotaros, D. Rial, C. Vega, "Optical solitons in nematic liquid crystals: model with saturation effects", *Nonlinearity 31*,1535–1559 (2018).

[112] G. Q. Zhang, A. Zuo, S. Y. Liu, "Ground state solitary waves for nonlocal nonlinear Schrodinger systems", *J. Math. Phys. 61*,091502 (2020).

[113] D Anderson. "Variational approach to nonlinear pulse propagation in optical fibres", *Phys. Rev. A 127*, 3135–3145 (1983).

[114] H. Goldstein, C. Poole and J. Safko, *Classical mechanics*, Addison-Wesley, 3rd edition, (2001), 34–63.

[115] G. Assanto, N. F. Smyth, and W. Xia, "Modulation analysis of nonlinear beam refraction at an interface in liquid crystals," *Physical Review A, 84*, 3, 033818, (2011).

[116] G. Assanto, N. F. Smyth, and W. Xia, "Refraction of nonlinear light beams in nematic liquid crystals," *Journal of Nonlinear Optical Physics & Materials, 21*, 03, 1250033, (2012).

[117] W. L. Kath and N. F. Smyth, "Soliton evolution and radiation loss for the nonlinear Schr¨odinger equation," *Physical Review E, 51*, 2, 1484, (1995).

[118] B. A. Malomed, "Variational methods in nonlinear fiber optics and related fields," *Progress in Optics 43*, E. Wolf, Elsevier Science, 71–193 (2002).

[119] E. Calisto, N.F. Smyth and G. Assanto, "Optical isolation via direction-dependent soliton routing in birefringent soft-matter", *Opt. Lett. 47*,459564 (2022).

[120] A. Alberucci and G. Assanto, "Propagation of optical spatial solitons in finite size media: interplay between non-locality and boundary conditions", *J. Optical Soc. Amer. B 24*, 2314–2320 (2007).

[121] A. Alberucci, G. Assanto, D. Buccoliero, A.S. Desyatnikov, T.R. Marchant and N.F. Smyth, "Modulation analysis of boundary induced motion of nematicons", *Phys. Rev. A 79*, 043816 (2009).

[122] E. Calisto and G. Assanto, "Counterpropagating optical solitary waves in orientation-modulated nematic liquid crystals", *Wave Motion 130*, 103379 (2024).

[123] L. Trefethen. *Spectral methods in MATLAB*. SIAM, Philadelphia (2000).

[124] A. A. Minzoni, N. F. Smyth, and A. L. Worthy, "Modulation solutions for nematicon propagation in nonlocal liquid crystals," *J. Opt. Soc. Am. B 24*, 1549-1556 (2007).

[125] I.C. Khoo et al., "Synthesis and characterization of the multi-photon absorption and excited-state properties of 4-propyl 4'-butyl diphenyl acetylene," *J. Mater. Chem. 19*, 7525-7531 (2009).

[126] R. J. Potton, "Reciprocity in optics", *Rep. Prog. Phys. 67*,717(2004)

[127] X. Fang, "Polarization-independent all-fiber isolator based on asymmetric fiber tapers," *Opt. Express 21,* 1792 (1993).

[128] L. Feng et al., "Nonreciprocal light propagation in a silicon photonic circuit", *Science 333*, 729 (2011).

[129] C. Wang, X.L. Zhong, and Z.Y. Li, "Linear and passive silicon optical isolator", *Sci. Rep. 2*, 674 (2012).

[130] S. Fan et al., "Comment on nonreciprocal light propagation in a silicon photonic circuit", *Science 335,* 38 (2012).

[131] Y. Shi, Z. Yu and S. Fan, "Limitations of nonlinear optical isolators due to dynamic reciprocity", *Nature Photon. 9*,388-392(2015).

[132] C. Caloz, A. Alù, S. Tretyakov, D. Sounas, K. Achouri, Z.-L. Deck-Léger, "Electromagnetic Nonreciprocity", *Phys. Rev. Appl. 10*, 047001 (2018).

[133] A.T. De Hoop, "Reciprocity of the electromagnetic field", *Appl. Sci. Res. 8*, 135 (1959).

[134] R. Carminati et al. "Reciprocity, unitarity, and time-reversal symmetry of the S matrix of fields containing evanescent components," *Physical Review A 62*(1)012712 (2000).

[135] A. Sanjeev,V. Trivedi and Z. Zalevsky, "Optical reciprocity induced wavefront shaping for axial and lateral shifting of focus through a scattering medium", *Sci Rep 12*, 6387 (2022).

[136] S.-Y Lee, et al. "Reciprocity-induced symmetry in the round-trip transmission through complex systems." *APL photonics 5* (10)106104 (2020).

[137] I.C. Khoo, "Nonlinear optics of liquid crystalline materials", *Phys. Rep. 471*,221-267 (2009).

[138] M.A. Karpierz, "Solitary waves in liquid crystalline waveguides", *Phys. Rev. E 66*,036603 (2002).

[139] M. Peccianti, C. Conti and G. Assanto, "Optical modulational instability in a non-local medium", *Phys. Rev. E 68*, R025602 (2003).

[140] G. Strangi, S. Ferjani, V. Barna, A. De Luca, N. Scaramuzza, C. Versace, C. Umeton and R. Bartolino, "Random lasing and weak localization of light in dye-doped nematic liquid crystals", *Opt. Express 14*,7737-7744 (2006).

[141] A.E. Miroshnichenko, E. Brasselet and Y.S. Kivshar, "Light-induced orientational effects in periodic photonic structures with pure and dye-doped nematic liquid crystal defects", *Phys. Rev. A 78*, 053823 (2008).

[142] S. Perumbilavil, A. Piccardi, R. Barboza, O. Buchnev, G. Strangi, M. Kauranen and G. Assanto, "Beaming random lasers with soliton control", *Nature Commun. 9*, 3863 (2018).

[143] G. Assanto and N.F. Smyth, "Spin-optical solitons in liquid crystals", *Phys. Rev. A 102,* 033501 (2020).

[144] C. Conti, M. Peccianti and G. Assanto, "Observation of optical spatial solitons in a highly nonlocal medium", *Phys. Rev.Lett. 92*, 113902 (2004).

[145] R. Dabrowski, P. Kula and J. Herman, "High Birefringence Liquid Crystals", *Crystals 3*, 443-482 (2013).

[146] E. Calisto and G. Assanto, "Direction-dependent optical solitary waves in nematic liquid crystals", *Physical Review A 108*, (4), 043509 (2023).

[147] E. Calisto and G. Assanto, "Nonreciprocal Propagation of Nematicons", *Photonics 10* (10), 1144 (2023).

[148] P.A. Breddels, "Trends and advances in developments of liquid crystal mixtures for TFT LCDs", In *Proceedings of the 12th International Topical Meeting on Optics of Liquid Crystals (OLC'07)*, Puebla City, Mexico, 1–5 October 2007; pp. 17–20.

[149] A. Fratalocchi, A. Piccardi, M. Peccianti and G. Assanto, "Nonlinearly controlled angular momentum of soliton clusters", *Opt. Lett. 32*, 1447-1449 (2007).

[150] A. Piccardi, A. Alberucci, U. Bortolozzo, S. Residori, G. Assanto, "Soliton gating and switching in liquid crystal light valve", *Appl. Phys. Lett. 96* (7) 071104 (2010).

[151] G. Assanto and N.F. Smyth, "Self-confined light waves in nematic liquid crystals", *Phys. D 402* 132182 (2020).

[152] A. Alberucci and G. Assanto, "All-optical isolation by directional coupling", *Opt. Lett. 36*, 1641-1643 (2008).

[153] Z. Yu and S. Fan, "Complete optical isolation created by indirect interband photonic transitions", *Nature Photon. 3* 91-94 (2009).

[154] A.E. Miroshnichenko, E. Brasselet, Y.S.Kivshar, "Reversible optical nonreciprocity in periodic structures with liquid crystals", *Appl. Phys.Lett. 96*,063302 (2010).

[155] S.V. Zhukovsky and A.G. Smirnov, "All-optical diode action in asymmetric nonlinear photonic multilayers with perfect transmission resonances", *Phys.Rev. A 83*,023818 (2011).

[156] H. Lira, Z. Yu, S. Fan, M. Lipson, "Electrically driven nonreciprocity induced by interband photonic transition on a silicon chip", *Phys. Rev.Lett. 109*, 033901 (2012).

[157] L. Fan, L.T. Varghese, J. Wang, Y. Yuan, A.M. Weiner, M. Qi, "Silicon optical diode with 40 dB nonreciprocal transmission", *Opt. Lett. 38*, 1259-1261 (2013).

[158] D.W. Wang, H.T. Zhou, M.J. Guo, J.X. Zhang, J. Evers, S.Y. Zhu, "Optical diode made from a moving photonic crystal", *Phys. Rev. Lett. 110*, 093901 (2013).

[159] B. Anand, R. Podila, K. Lingam, S.R. Krishnan, S. Siva Sankara Sai, R. Philip, A.M. Rao, "Optical diode action from axially asymmetric nonlinearity in an all-carbon solid-state device", *Nano. Lett. 13*, 5771-5776 (2013).

[160] D.L. Sounas and A. Alù, "Angular-momentum-biased nanorings to realize magnetic-free integrated optical isolation", *ACS Photon. 1*,198-204 (2014).

[161] D.L. Sounas and A. Alù, "Non-reciprocal photonics based on time modulation", *Nature Photon. 11*, 774-783 (2017).

[162] D.L. Sounas, J. Soric and A. Alù, "Broadband passive isolators based on coupled nonlinear resonances", *Nature Electron. 1*, 113-119 (2018).

[163] E.A. Kittlaus, W.M. Jones,P.T. Rakich, N.T. Otterstrom, R.E. Muller, M. Rais-Zadeh, "Electrically driven acousto-optics and broadband non-reciprocity in silicon photonics", *Nature Photon. 15*, 43-52 (2020).

[164] M. Yu et al., "Integrated electro-optic isolator on thin-film lithium niobate", *Nature Photon. 17*,666-671 (2023).

[165] S. Lepri and G. Casati, "Asymmetric wave propagation in nonlinear systems", *Phys. Rev. Lett. 106*, 164101 (2011).

[166] M. Peccianti, A. Fratalocchi, G. Assanto, "Transverse dynamics of Nematicons", *Opt. Express 12*, 6524-6529 (2004).

[167] A. Alberucci and G. Assanto, "Nematicons beyond the perturbative regime",*Opt. Lett. 35*,2520-2522 (2010).

[168] A. Piccardi, A. Alberucci and G. Assanto, "Soliton self-deflection via power-dependent walk-off", *Appl.Phys. Lett. 96*, 061105 (2010).

[169] P. Oswald and P. Pieranski, *Nematic and Cholesteric Liquid Crystals*, 1st ed., Taylor and Francis, Oxfordshire, UK, (2005).

[170] A. Alberucci, A. Piccardi,M. Peccianti, M. Kaczmarek, G. Assanto, "Propagation of spatial optical solitons in a dielectric with adjustable nonlinearity", *Phys. Rev. A 82*, 023806 (2010).

[171] W. Królikowski, O. Bang, N. I. Nikolov, D. Neshev, J. Whyller, J. J. Rasmussen, and D. Edmundson, "Modulation instability, solitons and beam propagation in spatially nonlocal nonlinear media," *J. Opt. B: Quantum Semiclassical Opt. 6*, S288–S294 (2004).

[172] M. Born and E. Wolf, *Principles of Optics*, 7th ed., Cambridge University Press, Cambridge, UK, (1999).

[173] A. Alberucci, M. Peccianti, G. Assanto, A. Dyadyusha and M. Kaczmarek, "Two-Color Vector Solitons In Nonlocal Media",*Phys. Rev. Lett. 97,* 153903 (2006).

[174] M. Peccianti, K.A. Brzd˛akiewicz and G. Assanto, "Nonlocal spatial soliton interactions in nematic liquid crystals," *Opt. Lett., 27,* 1460–1462 (2002)

[175] W. Hu, T. Zhang, Q. Guo, L. Xuan and S. Lan, "Nonlocality-controlled interaction of spatial solitons in nematic liquid crystals," *Appl. Phys. Lett., 89*, 071111 (2006).

[176] J.F. Henninot, J.F. Blach and M. Warenghem, "Experimental study of the nonlocality of spatial optical solitons excited in nematic liquid crystal," *J. Opt. A: Pure Appl. Opt., 9*, 20–25 (2007).

[177] A. I. Strinić, D. M. Jović, M. S. Petrović, D. V. Timotijević, N. B. Aleksić, and M. R. Belić, "Counterpropagating beams in nematic liquid crystals," *Opt. Express 14*, 12310-12315 (2006)

[178] L. Del Bino, J. M. Silver, M. T. M. Woodley, S. L. Stebbings, X. Zhao, and P. Del'Haye, "Microresonator isolators and circulators based on the intrinsic nonreciprocity of the Kerr effect," *Optica 5*, 279-282 (2018).

[179] A.D. White et al, "Integrated passive nonlinear optical isolators", *Nat. Photon. 17*, 143–149 (2023).

[180] Roger, T., Maitland, C., Wilson, K. et al. "Optical analogues of the Newton–Schrodinger equation and boson star evolution". *Nat Commun 7*, 13492 (2016).

[181] Bekenstein, R., Schley, R., Mutzafi, M. et al. "Optical simulations of gravitational effects in the Newton–Schrödinger system". *Nature Phys 11*, 872–878 (2015).